Masteroppgave

NTNU
Norges teknisk-naturvitenskapelige universitet
Fakultet for informasjonsteknologi og elektroteknikk
Institutt for elkraftteknikk

Gaute Hagen Hallingstad

Online condition monitoring of synchronous generator using shaft signals

Masteroppgave i Energy and Environmental Engineering
Veileder: Arne Nysveen
Medveileder: Hossein Ehya
Juli 2021

NTNU
Kunnskap for en bedre verden

Gaute Hagen Hallingstad

Online condition monitoring of synchronous generator using shaft signals

Masteroppgave i Energy and Environmental Engineering
Veileder: Arne Nysveen
Medveileder: Hossein Ehya
Juli 2021

Norges teknisk-naturvitenskapelige universitet
Fakultet for informasjonsteknologi og elektroteknikk
Institutt for elkraftteknikk

NTNU
Kunnskap for en bedre verden

Abstract

Hydropower generators produce almost 100% of Norway's electricity. The primary type of generator is the Salient pole synchronous generators (SPSG). A steady operation of the SPSGs in hydroelectric power plants is essential to avoid unplanned stoppages that can give substantial cost increases in the production. One of the factors that ensures a steady operation of the SPSGs is to avoid faults.

When a fault occurs in an SPSG, the symmetrical flux field in the shaft is disturbed, and this causes an induced voltage. A way to discover faults at an early stage, can be to continuously measure the shaft voltage. Shaft voltage is a non-invasive method that has been utilized on other types of machines, but not that much on SPSGs. Two prominent faults on the SPSG are Static eccentricity (SC) and Inter-Turn Short Circuit (ITSC).

This thesis investigates whether shaft voltage can be used to identify the two fault types SC and ITSC, and the severity of the fault(s). The investigation is done by Finite element modeling (FEM) and experimental measurement on the 100 kVA laboratory SPSG located in the NTNU smart grid laboratory. In order to reveal a frequency-magnitude or time-frequency-magnitude pattern the signal processing methods such as Fast Fourier transform (FFT) and Continues wavelet transform (CWT) have been used.

FEM analysis of the generator with no load revealed that there are specific frequencies related to SC and ITSC. In ITSC, the slotting frequency is the most prominent component, and it seems to have the potential to distinguish between an ITSC of 2.9% on one pole and a healthy situation. It was also possible to distinguish between 10% static eccentricity by looking at the 50 Hz component. CWT, on the other hand, seems to not give any useful information.

Laboratory measurements with a load on the machine did reveal that the load impacts the shaft voltage. However it was more challenging to distinguish between 0 and 2.9% ITSC. The conclusion is that it is possible to use shaft voltage while running in no-load or use the variability of specific frequency.

Sammendrag

Nesten 100% av Norges elektrisitet produseres med vannkraft. Vannkraftprodusentene i Norge bruker i hovedsak generatorer av typen synkrongenerator med utpregede poler (SGUP). En sikker drift av disse generatorene er viktig for å ikke få uplanlagte stopp i produksjonen som kan føre til økning i produksjonskostnadene. Ulike feilsituasjoner som kan gi slike stopp bør unngås.

Noen av feilene som kan forekomme i en generator av denne typen kommer av forstyrrelser i det symmetriske fluksfeltet i akselen, som kan forårsake indusert spenning. Kontinuerlig måling av akselspenningen kan avsløre slike feil på et tidlig tidspunkt. Måling av akselspenning er en ikke-inngripende metode som brukes på ulike typer maskiner, men det har ikke blitt så mye brukt på SGUP. To vanlige feil på en SGUP er feil av typen statisk eksentrisitet og kortslutninger mellom vindingene i feltviklingen.

I denne oppgaven har det blitt undersøkt om måling av akselspenning kan brukes til å oppdage de to nevnte feiltypene, og også om det kan brukes til å avsløre alvorlighetsgraden av disse. Forsøk er gjort ved hjelp av Finite Element Modelling (FEM) og eksperimentelle målinger utført ved 100 kVA-generatoren som ligger i NTNUs Smart Grid laboratorium. For å kunne oppdage en frekvensstørrelse eller en tidsfrekvensstørrelsemønster, er signalprosesseringsmetoder som Fast Fourier Transform (FFT) og Continues Walwet Transform (CWT) anvendt.

FEM-analyse av generatoren uten belastning avslørte at det er spesifikke frekvenser relatert til statisk eksentrisitet og kortslutninger mellom vindingene i feilutviklingen. I kortslutningene mellom vindingene er sporingsfrekvensen den mest fremtredende komponenten, og den ser ut til å ha potensial til å skille mellom en kortslutning på $2,9\%$ på en pol og en normal situasjon. Det var også mulig å skille mellom 10% statisk eksentrisitet ved å se på 50 Hz-komponenten. CWT ser derimot ikke ut til å gi noen nyttig informasjon.

Laboratoriemålinger med belastning på maskinen avslørte at lasten påvirker akselspenningen. Det var imidlertid mer utfordrende å skille mellom 0 og $2,9\%$ kortslutning. Konklusjonen er at det er mulig å bruke akselspenning når det kjøres uten belastning, og å bruke variabilitet til spesifikke frekvenser.

Contents

List of Figures

List of Tables

Chapter 1

Introduction

1.1 Background

Hydropower generators produce almost 100% of Norway's electricity [1]. The primary type of generator in the Norwegian hydropower plant is the Salient pole synchronous generator (SPSG). Dependable operation of SPSGs is critical for maintaining high reliability of production. With an increased percentage of non-regulated power sources, this will be even more important in the years to come.

There are different faults that can occur in an SPSG. They might not directly cause a momentary shut-down of the generator, but they will degrade the machine. This makes the machine less efficient, and if not treated, it will potentially force an unplanned shut-down or cause costly and irreversible damage to the machine. By continuously monitoring various machine parameters, it is possible to detect faults on an incipient stage. This is known as online condition monitoring of electrical machines, and it can potentially provide a real-time assessment of the machine.

Online monitoring based on shaft voltage monitoring has been investigated before [2]. However, most work has been focused on induction machines and round-rotor synchronous machines. The studies on the fault detection of SPSGs using shaft voltage is limited. [3] investigates shaft voltage based on analytical and experimental results for eccentricity and inter-turn short circuit fault detection. The results indicate that static eccentricity and inter-turn short circuit can be detected using aforementioned method.

This thesis is a continuation of the research initiated at NTNU for online condition monitoring of SPSG that the theoretical studies have been done in the specialization project during the fall semester of 2020. The work focused on finite element modeling of inter-turn short circuits and static eccentricity and investigating patterns in shaft voltage that could be used to address the fault type in the SPSG.

1.2 Objectives and scope of work

The main objective of this thesis has been to investigate whether and how incipient electrical and mechanical faults can be detected by implementing an online shaft voltage monitoring system.

The thesis includes the following:

- 2D finite element analysis of a the generator located at NTNU Smart grid laboratory. The simulations were performed with load and at no-load, in an healthy operating condition, and faulty conditions including static eccentricity fault and inter-turn short circuit fault in the rotor field winding.
- Generator modifications. The laboratory generator at NTNU was modified with an isolated bearing to accommodate for the simulations. A measurement setup with a brush attached to the shaft was also developed.
- Running of the lab generator. The generator was operated with different loads and faults. During the operation, the shaft voltage was measured.
- The results from the 2D finite element modeling and the measurements from the experimental simulations were analyzed to assess the impact of the generator under the various conditions. And also to find out if it is possible to simulate the shaft voltage of a synchronous generator and to see if load has any impact on the results.

1.3 Methods, tools, and limitations

The finite element analysis was performed on 2D models of the salient pole synchronous generator located in the smart grid laboratory. The finite element analysis was done in ANSYS Maxwell 2019 and ANSYS Maxwell 2020 as a part of the ANSYS Electronics Desktop software. The objective of the finite element analysis was to investigate how the inter-turn short circuit and static eccentricity impacts the induced voltage in the shaft of the generator. The simulations were performed under both load and no-load conditions. This was done to investigate whether the loading of the generator has an impact on the amount of induced voltage in the shaft.

Except for the shaft and housing of the generator, the model of the generator was already developed. These parts were made as accurate as possible to make the results of the simulations comparable with the later measured voltage on the generator. Simplifications such as modelling the generator in 2D, even though the generator is a 3D objective, and restricting the number of mesh points was done. These simplifications where necessary in order to have an acceptable running time of around 24 hours. The finite element modeling

is described in chapter 3.

The second part of this work describes how the measurement of the shaft voltage works, the interpretation of the results and how the comparison with the theoretical finite-element analysis is done. Multiple different tests were performed to find the best way to measure the shaft voltage. The aim was to get an adequate signal quality for on-line monitoring. Different types of measuring points and brush positions were tested to see the impact on the signal. The experimental test setup is described in chapter 5. A significant part of the work is how to extract patterns that one could use to assess the generator's health under the various conditions. The method of Fourier transform, short-time Fourier transform, and continuous wavelet transform is explained in chapter 2.4. Python with the packages Scipy [1] and PyWavelets[2] were utilized to process the data. The processing of the data is described in chapter 5.2.2.

1.4 Thesis outline

Chapter 2. A description of the faults that are investigated in this thesis. First the term shaft voltage is defined. Then follows a description of various sources to the shaft voltage and how it is already utilized today. The last part of the chapter describes the converting of analog signals to digital by utilizing an oscilloscope and different signal processing methods.

Chapter 3. A description of the laboratory generator at NTNU, including the nameplate values and other specifications.

Chapter 4. A description of how the generator shaft and housing were modeled, and how the simulations were executed. The last part of this chapter includes a description of creating a model of a stiff grid that connects to the generator.

Chapter 5. Detailed information about the laboratory set-up. Description of how the different types of faults was imposed on the machine. This chapter also covers the process of getting good measurements of the shaft voltage.

Chapter 6. A presentation of the results from both the simulation and the measured shaft voltage.

Chapter 7. The main parts of the project are discussed, and future work is proposed.

Chapter 8. Conclusion and the main finding in the thesis.

Appendix A includes a schematic of the generator rotor and housing. Appendix B in-

[1] Open-source software for mathematics, science and engineering
[2] Open-source wavelet transform software

cludes a circuit diagram of a circuit that incorporates the capacitances of the bearing and shaft isolation. Appendix C presents CWT of the simulation done in the project work. Appendix D presents the Fourier transform of the simulated voltage induced the shaft and the housing with ITSC. Appendix E presents a comparison of the measured shaft voltage at the start and the end of the measurement session.

Chapter 2

Theoretical Background

This chapter starts with a description of the two different types of faults investigated in the thesis. The two types of faults are inter-turn short circuit in the field winding and static eccentricity.

After this follows an overview of shaft signals and how they are utilized in online condition monitoring to detect different types of faults.

Finally, there is a section covering how the analog signal is processed into a digital signal and then analyzed with fast Fourier transform, short-time Fourier transform, and wavelet transform.

2.1 Inter-turn short circuit in the field winding (ITSC)

Over time, the winding insulation decays due to mechanical, electrical, and thermal stresses and also due to aging and contamination. This can result in insulation breakdown. Other faults like broken damper bars and eccentricity can also lead to a temperature rise in the rotor, increasing the thermal stress on the isolation. Short circuits can happen between turns within the field coils called inter-short circuits or between a turn or the ground point, called a ground fault. The isolation between the field coils usually degrades before the insulation between the ground and conductors.

An ITSC reduces the number of ampere-turns in one pole. This weakens the magnetic field and the Magnetic motoric force (MMF) of the pole. The weakened magnetic field causes an asymmetrical air-gap field that results in a distorted force distribution that generates an Unbalanced magnetic pull (UMP). This can further lead to more vibrations in the machine, and more damage on the winding insulation. Differences in the temperature of the rotor can also lead to increased UPM due to developed shaft bowing. The temperature of the machine can vary because of uneven distribution of losses in the coil. All of this can

lead more short circuiting and stronger UPM. This means that what may start as a small ITSC with a small impact of the machine, can further down become the reason for a major fault and break down [4].

2.2 Eccentricity

In an electrical machine, eccentricity is when the air gap is not constant. Earlier, when eccentricity occurred it was normally due to manufacturing imperfections such as shaft bow, unbalanced mass or bearing tolerance, this is now seldom seen [5]. If eccentricity is seen during load, this is now normally not a symptom of manufacturing imperfections, but a symptom of a bearing fault [6].

There are two primary types of eccentricity; static and dynamic. There can also be a combination of the two types, this is referred to as mixed eccentricity. Static eccentricity is when the point the rotor rotates around is not in the center of the machine 2.1. When the point of rotation is not in the center of the rotor, it is dynamic eccentricity 2.2.

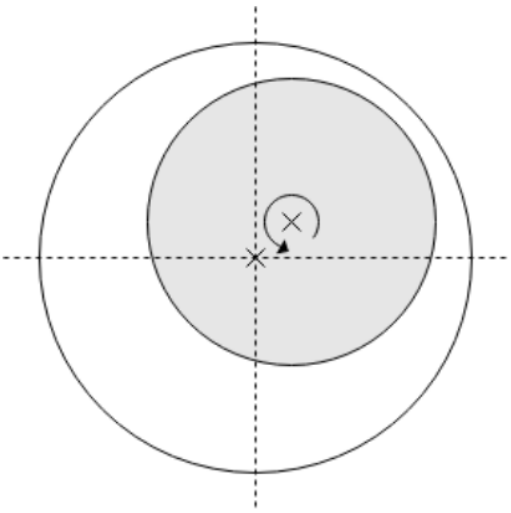

Figure 2.1: Static eccentricity

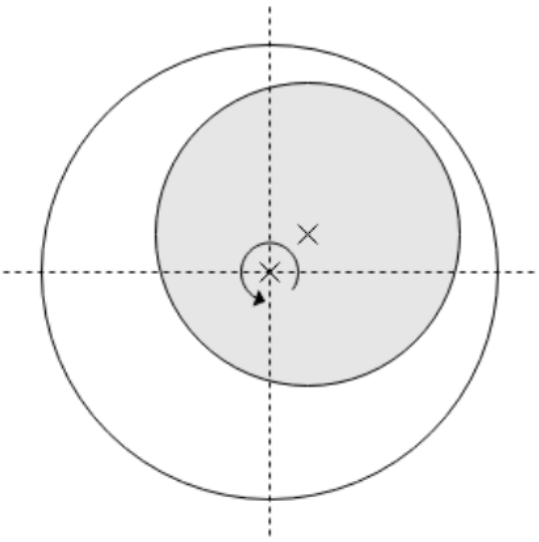

Figure 2.2: Dynamic eccentricity

The difference between the two types of eccentricity is that in static eccentricity, the air gap length varies with the rotor's position while in dynamic eccentricity, the air gap length varies with time. This will result in an asymmetrical magnetic field. This field will, in turn, result in an unbalanced magnetic force, enhanced noise level, and increased bearing vibration [7]. This fault may also eventually develop into an earth fault that triggers the ground fault protection relay, and the machine is shut down. A second earth fault results in large currents that can damage the machine.

2.3 Shaft signal

Shaft voltage is the voltage between the shaft and the machine's frame. This voltage is marked as V_b in fig 2.3. This voltage and current have been known as a source of possible problems in revolving electric machines for a long time [8]. Countermeasures have been taken to avoid this problem. Such countermeasures could be grounding the brushes for turbo generators, isolated coupling, or isolated bearings to prevent shaft currents from going through the bearings [3]. In salient pole synchronous generators is the practice of Statkraft [1] the generators are grounded if it is expected to have a shaft voltage above 1 V.

There are four types of sources to induced voltage in the shaft: Alternating voltages induced in the stator, axial rotor flux, electrostatic effect, and external potential applied to the shaft. The four different sources are described below. Alternating voltages induced in the shaft: This is caused by an unbalanced magnetic field. This field occurs when a flux that takes a clockwise- and counter-clockwise path through the yoke is not equal. In this situation, there will be a circulating flux that links with the shaft. If this shaft is alternating, there will there be induced a voltage in the shaft. For example, a typical stator of a generator is transported in sections and then combined to form a circle. If the permeance across the joints is not similar, the clockwise and counter-clockwise flux will not be equal, and there will be an induced voltage in the shaft. This voltage works in the circuit, shaft, bearing, pedestals, and base of the generator. If the voltage is high enough, or the bearing is not adequately isolated, the current will flow in a loop as shown in fig 2.3.

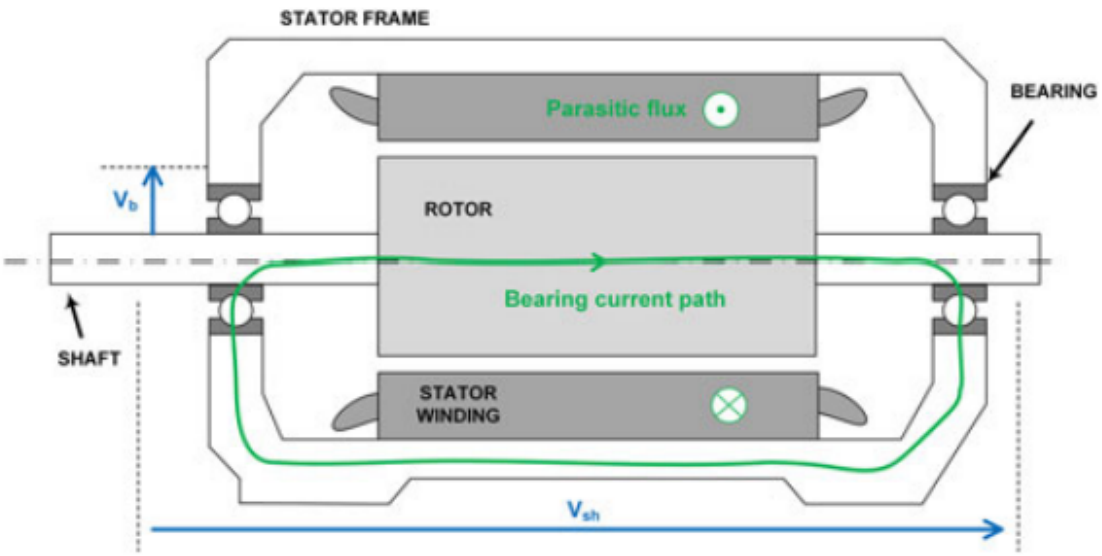

Figure 2.3: Illustration of shaft voltage and current [2]

[1] The biggest renewable power producer in Europe

Rotor eccentricity and bowed rotors can also create this type of shaft voltage. Axial rotor flux: If a magnetic flux flows in the current path as shown in fig 2.3 there will be induced a voltage in each bearing due to the revolving shaft cutting the flux that is passing from the shaft to the bearing. Usually, the voltage induced in the two bearings will neutralize each other. This leads to a local current flowing within the bearing [8]. Electrostatic effect: This is caused by external impacts. The external impact often comes from friction of pulleys, belts, and wet steam in low-pressure turbines or friction between turbine blades. This capacitive effect occurs when charges build up on the bearing lubrication until the lubricate threshold is surpassed. This will make current flow through the bearing [9].

An external potential applied on the shaft; Thyristors controlled excitation current in a synchronous generator contains relatively high-frequency components that could be induced in the shaft. This is due to the capacitive coupling between the shaft and the rotor winding [2].

2.3.1 Fault Diagnosis

By looking at shaft signals, it is possible to get crucial information about the machine's condition. The alternating voltage induced in the stator is the most prominent for faults like ITSC and eccentricity. The review article [2] has summarized many articles regarding these types of faults. When it comes to inter short circuits, it is stated that harmonics below 300 Hz are present. Static eccentricity is often linked to odd harmonics such as 1st, 3rd, 5th, and 7th. These harmonics are shown to be constant concerning the number of pole-pairs in the machine. Higher frequencies were also observed.

Article [10] examined a scaled version of a large turbo generator. Experimental measurements and finite element analysis of the generator were done. Fourier transform of the shaft voltage during static eccentricity did reveal that the main frequency component was the slotting frequency. This frequency is the frequency of slots passing by when one pole/point on the rotor rotates one rotation. The frequency is given by:

$$f_s = f_r n_s \tag{2.1}$$

f_r is the mechanical frequency of the rotor and n_s is the number of slots. The machine in [10] has a nominal speed of 1,500 rpm with 48 slots, this gives a slotting frequency of 1,200 Hz.

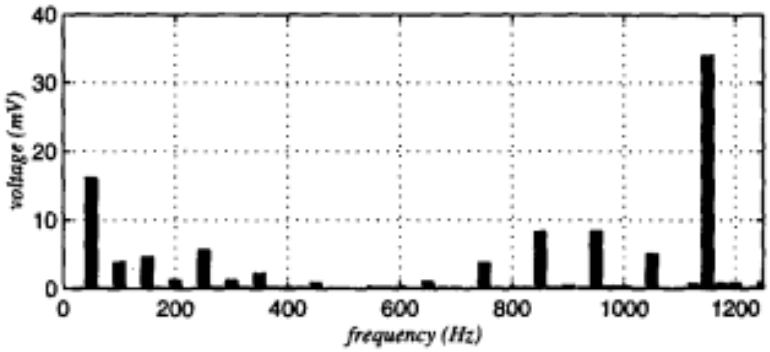

Figure 2.4: Measurement of the shaft voltage: Static eccentricity, [10]

Paper [3] has a study of the relationship between shaft signals, eccentricity, and ITSC in salient pole generators. It states that the induced voltage due to static eccentricity happens because the rotor is not centered in the machine. When the rotor is not centered, an unequal flow of fluxes flows in the shaft and forms a circulation flux that links with the shaft. This is illustrated in fig 2.5.

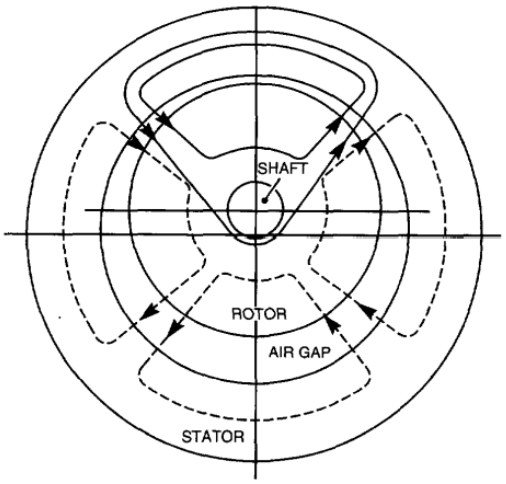

Figure 2.5: Shaft flux linkage with respect to air gap rotating flux [3]

A certain degree of magnetic saturation occurs in an electric machine. When the material is saturated, a third harmonic flux component will occur in the air-gap. The third harmonic is usually filtered out of the stator current by connecting the machine is star-connecting [11]. However, the component is not filtered out of the shaft voltage. Therefore, one expects that this frequency is linked with the magnetic field saturation that potentially occurs in a situation with static eccentricity. It develops an analytical formula for ITSC in a salient-pole synchronous generator. The idea is to model the shorted turns as an additional field coil made up of the same number of turns as the shorted turns but with a current flowing oppositely. The Magnetomotive force (MMF) component of these two coil poles and the

main MMF produces an MMF modulated by (p-1)/2. The MMF is then given by:

$$sin(\phi - \frac{\omega_s t}{p}) + sin(p\phi - \omega_s t) \tag{2.2}$$

With some algebra the MMF is given by:

$$sin\left[\frac{1+5p\phi}{2} - \frac{(1+5p)}{2p}(\omega_s t)\right] cos\left[\frac{(p-1\phi)}{2} - \frac{(p-1}{2p}(\omega_s t)\right] \tag{2.3}$$

This equation was validated in the paper by measuring and simulating of the shaft voltage by sampling shaft voltage on a 6-pole generator. This gives a number of pole pares p equal to 3, the harmonic component of the air-gap flux is the given by:

$$sin\left[8\phi - \frac{8}{3}(\omega_s t)\right] cos\left[\phi - \frac{1}{3}(\omega_s t)\right] \tag{2.4}$$

By inserting the pole number is it shown that a harmonic component of the 8th mechanical order is generated. The 8th mechanical gives an a frequency of $\frac{60}{3}8 = 160Hz$ when the electrical frequency is 60 Hz. This frequency is shown in figure 2.6.

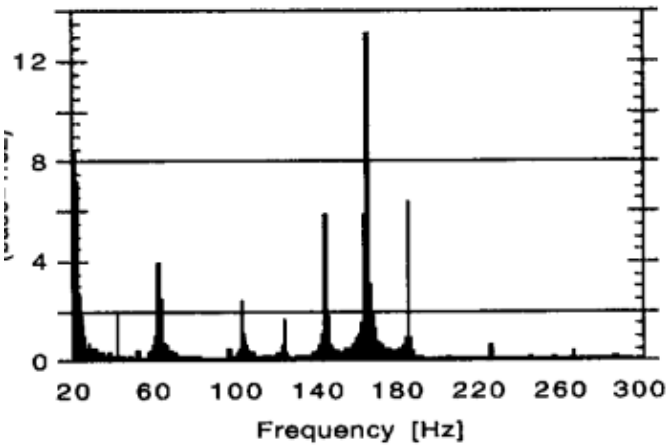

Figure 2.6: Relative shaft-flux-linkage harmonic magnitude with shorted field [3]

2.4 Signal processing tools (SPT)

To extract the proper indices from the fault signal, it is necessary to use different signal processing tools. The development of powerful microprocessors and new algorithms has made this possible. Signal processing tools can be categorized into two types, stationary and none-stationary. The most common stationary method used is the Fourier transform, and specifically the Fast Fourier Transform algorithm. This method is suitable for looking at the different harmonics in a faulty signal. It is necessary to calculate the Fourier transform over a long time to get adequate frequency precision [12, p 501]. This will increase the risk that non-stationary events like fluctuations in the load and power supply influence the signal. Methods that address this problem are short-time Fourier transform and Wavelet transform. Most of the work done in online condition monitoring has been on induction

motors and permanent magnet motors. Therefore, examples of usage mainly focus on this type of machine since there are little to none usage in condition monitoring on salient pole synchronous generators.

2.5 Discretization of a signal

The voltage measured at the shaft is a continuous analog signal that needs to be converted to a digital signal to process it digitally [12, p. 19]. This conversion procedure is called analog to digital (A/D) conversion. Fig 2.7 illustrates this process and a further explanation of the figure will follow below.

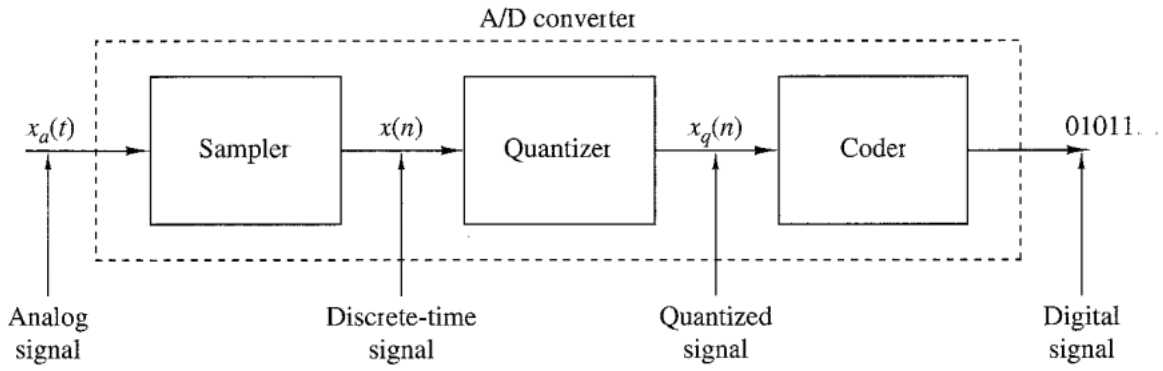

Figure 2.7: Block diagram of an analog-to-digital converter: Source adapted from [12, p 19]

1) Sampling is the process of measuring the signal $x_a(t)$ at discrete-time instants. 2) Quantization means taking each sample and giving it a value from a finite set of possible values. 3) Coding. In this process, each discrete value $x_q(n)$ is represented by a b-bit binary code. There are numerous ways to sample an analog signal. In this project a uniform or periodic sampling is used as illustrated in fig 2.8. The signal $x_a(t)$ is measured $x_a(t)$ every T seconds in order to generate a discrete-time signal $x(n)$ given by:

$$x(n) = x_a(nT), \ -\infty < n < \infty \tag{2.5}$$

Where T is the sampling interval, and its reciprocal $1/T = F_s$ is the sampling frequency.

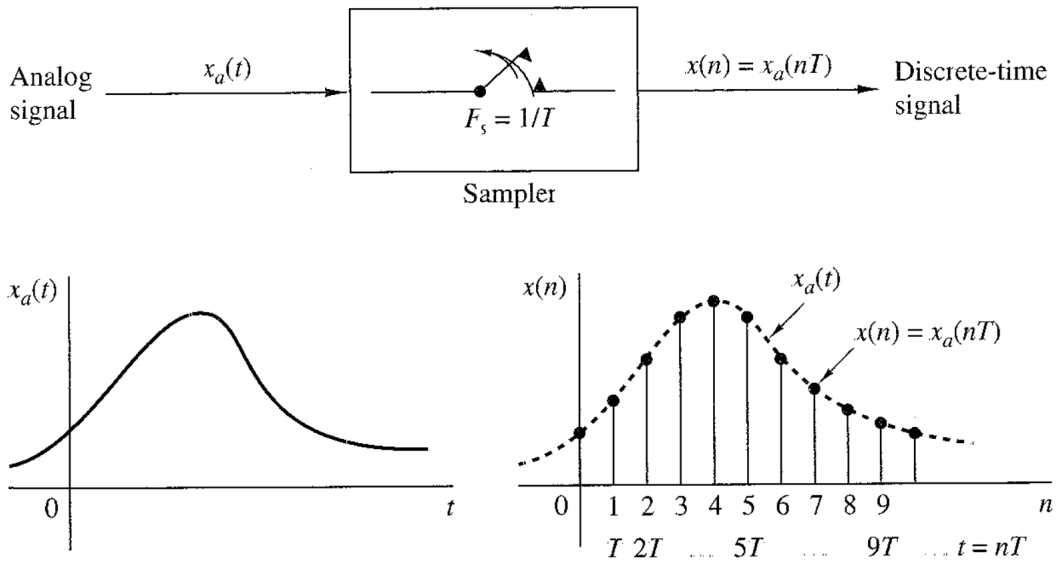

Figure 2.8: Periodic sampling of a signal: Source adapted from [12, p 21]

An analog sinusoidal signal is given by:

$$x_a(t) = Acos(2\pi ft + \theta), \ -\infty < t < \infty \tag{2.6}$$

This is sampled at F_s, by combining 2.5 and 2.6 gives a discrete-time sinusoidal signal of:

$$x_a(nT) = Acos(2\pi fnT + \theta) \tag{2.7}$$

The frequency of the signal is then $f = \frac{F}{F_s}$ The range of the frequency F is $-\infty < F < \infty$, for a discrete-time sinusoidal it is $-\frac{1}{2} < f < \frac{1}{2}$. By substitution of f the possible frequencies of the analog signal are bounded by $-\frac{F_s}{2} < F < \frac{F_s}{2}$. This is known as the Nyquist frequency and means that the sample frequency must be at least the double of the frequency one is sampling.

The signal is quantization by rounding the discrete-time signal to the nearest quantities step. Fig 2.9 illustrates the process on a sampled sinusoidal signal $x_a(nt)$. The distance between Δ between two quantifier steps is called resolution. The resolution is determined by:

$$\Delta = \frac{x_{max} - x_{min}}{L - 1} \tag{2.8}$$

$x_{max} - x_{min}$ is the dynamic range of the signal and L is the number of quantization levels. The effects that the quantization has on the performance of the A/D converter is quantified by the Signal-to-quantization-noise (SQRN). This is given by:

$$SQNR = 10log_{10}\frac{P_x}{P_n} \tag{2.9}$$

Where P_X is the signal power and P_n is the power of the signal quantization noise.

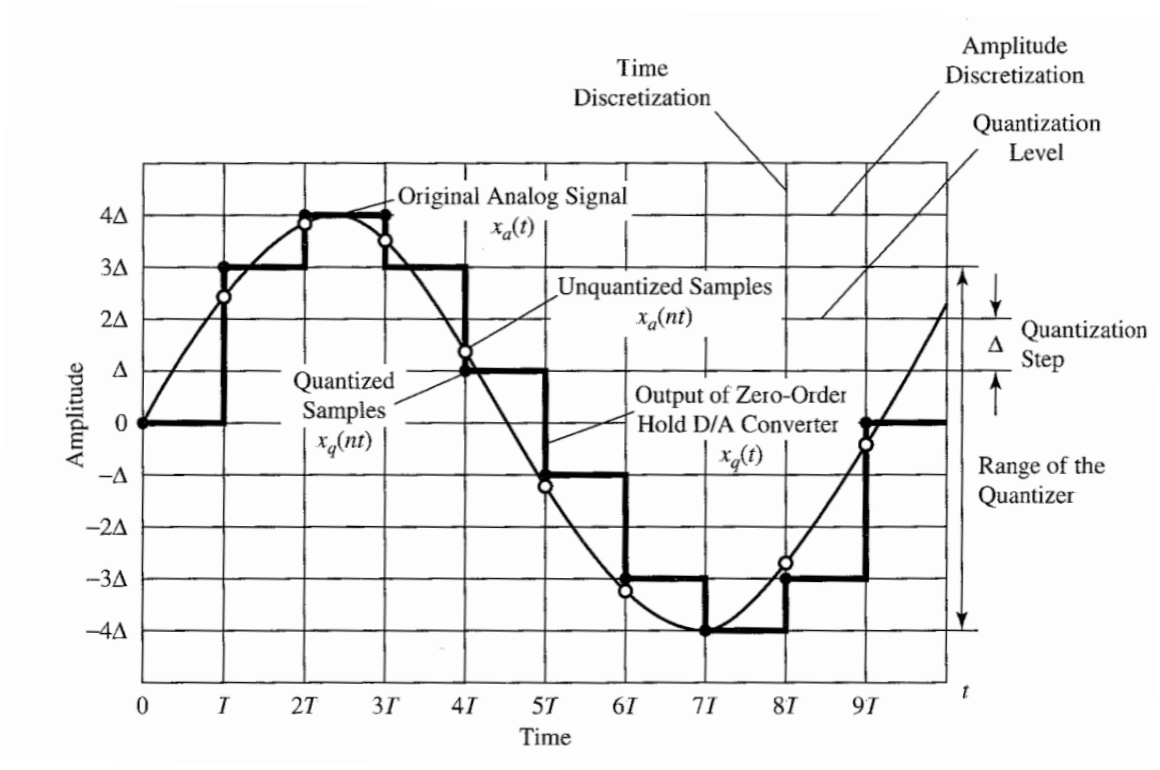

Figure 2.9: Illustration of quantization: Source adapted from [12, p 34]

The coding is done to ensure that one unique binary number is given to each quantization level. Thus, with L levels, there is a need for at least L different binary numbers. This means that at least $log_2 L$ bits B is needed.

2.5.1 Oscilloscope

In order to graphically display an electric signal a digital oscilloscope is used. A digital oscilloscope uses an A/D to convert the signal into digital information. It acquires the waveform as a series of samples and stores the samples until it accumulates enough to describe the waveform. Fig 2.10 illustrates this process.

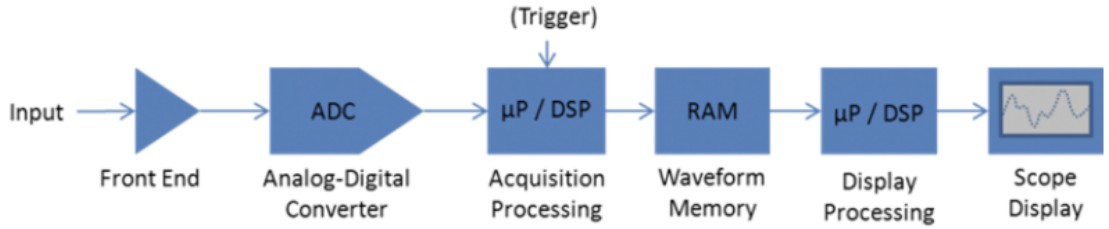

Figure 2.10: Simplified block diagram of a digital oscilloscope [13]

1) First the analog signal is scaled, and an anti-aliasing filter is applied. The filter is a low-pas filter with a bandwidth representing an amplitude decrease of 3 dB at the rated

bandwidth of the scope. To have a signal with minimal annotation, a bandwidth of $\frac{f_B W}{3}$ is sufficient. 2) Analog-Digital converter works in the same way as described in section 2.5 3) The primary purpose of the acquisition processing is to provide a stable display of the waveform. 4) Waveform memory: The signal is stored in memory to display the signal. With a large amount of data, it can occupy a significant portion of the oscilloscope's memory. For example, if a scope has a 5Gs/s sample rate and uses a horizontal scale of $20\mu s/div$, this will return 1 million samples. Various methods are commonly used to reduce the sample rate to fit a waveform into the oscilloscopes memory. These are known as acquisition modes. The default acquisition mode on most scopes is called sample. The sample mode lets the user set the sampling rate at a predefined sampling interval, and the rest of the sample points are left out. The problem with this acquisition mode is that there is a risk that some of the left-out samples are the highest and lowest points and, therefore, the most important ones. To compensate for this and ensure that these points are detected, is it possible to use acquisition mode PEAK. In this mode are extremal values from adjacent pairs of the sample interval put into memory. High and low values are therefore clearly captured, but the waveform is somewhat obscured. Hi-rise acquisition mode reduces the sampling rate by averaging the sample points to reduce noise/variations in the signal. This improves the vertical resolution, but it tends to hide glitches and reduce the bandwidth. [13].

2.5.2 Fourier Transform

The purpose of a Fourier transform is to take a function depending on time or space and convert it to a function depending on frequency. The figures below illustrate this.

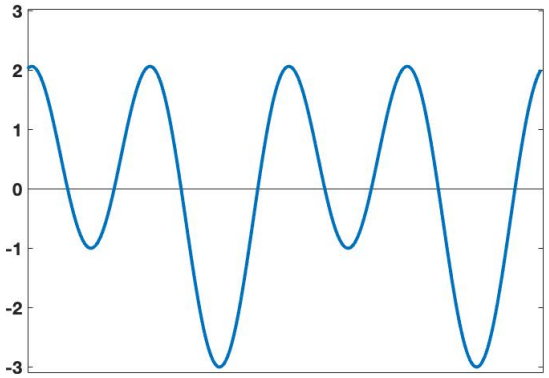

Figure 2.11: Plot of a periodic function that is a sum of fig 2.12 and fig 2.13

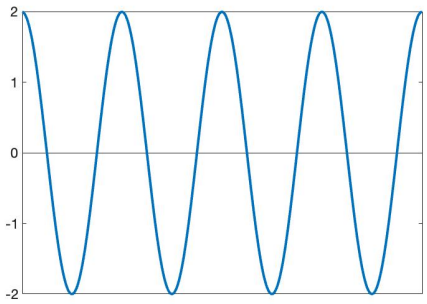

Figure 2.12: Plot of a cosine

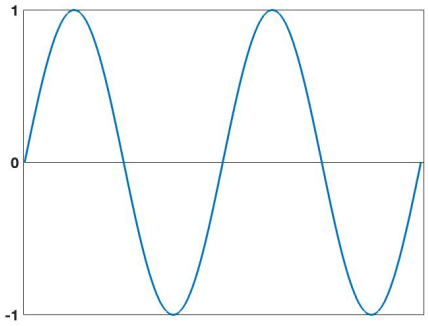

Figure 2.13: Plot of a sinus

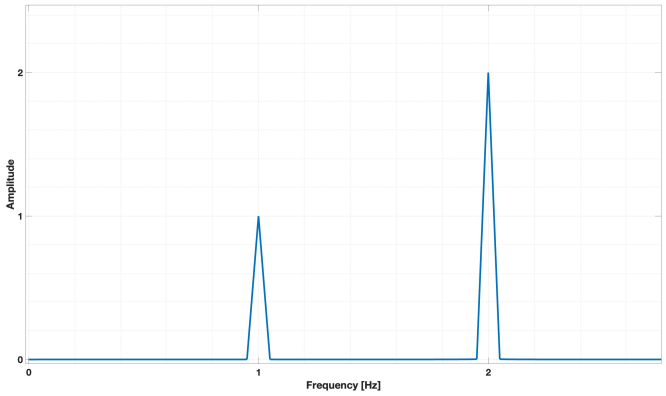

Figure 2.14: Fourier transform of fig 2.11

Fourier transform is given by

$$f(omega) = \frac{1}{\sqrt{2\pi}} \int_{-\infty}^{\infty} f(x) e^{-j\omega x}\, dx \tag{2.10}$$

Fourier transform is an extension of the Fourier series. Where Fourier series are infinite series designed to represent general periodic functions, Fourier transform is designed to represent non-periodic [2] functions [14]. This is illustrated in fig 2.11, 2.12 and 2.13 where two sinusoidal are plotted and also a sum of the two. Fig 2.14 shows the magnitude spectrum of fig 2.11. The vertical axis represents the amplitude of the Fourier coefficient, and the horizontal axis represents the frequency of the signal.

Discrete Fourier transform To utilize Fourier analysis on the sampled data instead of functions, the Fourier transform can be replaced with a discrete Fourier transform.

$$X(\omega) = \sum_{n=-\infty}^{\infty} x[n] e^{-j\omega n} \tag{2.11}$$

[2] Every non-periodic function is not liable for the Fourier integral to converge, but this is not essential for this thesis

To compute the spectrum of discrete-time signal, the value of the signal at all times is required [12, p 500]. This is not possible in a real-world situation. Signals can only be observed for a finite period, and the spectrum is therefore an approximation. When an analog signal is being sampled at the rate of $F_s > 2B$ where B is the bandwidth of the filtered signal, the highest frequency in the sampled frequency is $F_s/2$. The sampling period is limited to the interval $T_0 = LT$ where L is the number of samples and T is the sample interval. This finite observation interval limits the frequency resolution and in order to distinguish between two frequencies f_1 and f_2 must $|f_1 - f_2| < \frac{1}{LT}$ [12, p 501].

The usage of finite set of samples is analogous to multiplying the signal x(n) with a rectangular window $\omega(t)$ on the interval $0 < n < L - 1$

$$x(n) = x(n)\omega(n) \tag{2.12}$$

where

$$\omega(n) = \begin{cases} 1, & 0 < n < L - 1. \\ 0, & \text{otherwise.} \end{cases} \tag{2.13}$$

Given that the the sequence x(n) is a sinusoidal:

$$x(n) = sin\omega n \tag{2.14}$$

By padding the sinusoidal with N-L zeros and compute the Fourier transform of the truncated sequence of L points. The amplitude spectrum given that N is 1,025 point, ω is $2\pi 100$ and L is 25 is seen in fig 2.15:

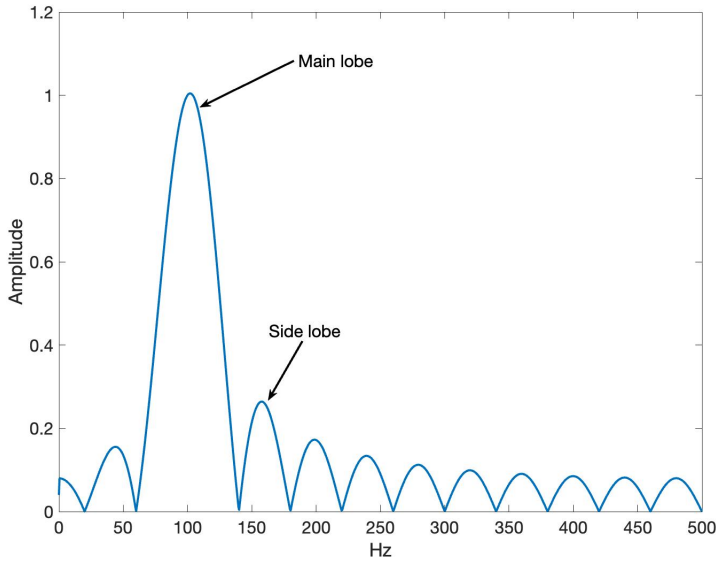

Figure 2.15: Example of spectral leakage

The spectrum in fig 2.15 shows that the power of the original frequency is spread out across the frequency range. This is known as spectral leakage. A solution to this problem is to

multiply the signal with a window function $\omega(n)$ that has lower side lobs in the frequency domain. However, a reduction in the side lobs means that the main lobe increases, reducing frequency precision. [12, p 502].

2.5.3 Short Time Fourier Transfrom (STFT)

STFT is a way of computing the Fourier transform and get insight into the timing of the different frequencies. STFT cuts the signal into shorter segments with equal length, tapers each segment with a specified window function, calculates a power spectrum, and puts it as a column in the output graph. Mathematically this is written as:

$$STFT(\tau, \omega) = \int_{-\infty}^{\infty} x(t)\omega(t-\tau)e^{-j\omega t}\, dt \tag{2.15}$$

$x(t)$ is the signal, ω is the window function and τ is the specified window length. However, in this project, discrete-time STFT is utilized since one can use overlapping segments that reduce artifacts at the boundary. Discrete-time STFT is given by:

$$DT - STFT(m, \omega) = \sum_{n=-\infty}^{\infty} x[n]\omega[n-m]e^{-j\omega n} \tag{2.16}$$

The length of the segments specifies the respectively short length, accurate time representation, and long length, accurate frequency representation. This is known as the uncertainty principle. This principle states that both accurate time and accurate frequency representation is not possible to achieve at the same time. The tapering of the signal is the same as windowing the Fourier transform. To get both the correct frequency and the correct time resolution, is it possible to specify the segment length for each frequency. This gives the user great flexibility. However, the process is tedious since the parameters are mostly specified in a trial-and-error operation.

The advantage of the STFT has been utilized to investigate the start-up of a machine and look at the effect of a broken damper bar. This method is reviewed in [15] for an asynchronous machine. The stator current was measured to detect a broken damper bar. A broken damper baris shown to induce harmonics far from the fundamental wave. With two broken damper bars, the magnitude of harmonics will drop. This makes them hard to detect with FFT. However, at start-up, the fault component reaches values several times greater than in a steady state. Because of this STFT is utilized on the start-up current, and the result from a healthy generator is seen in fig 2.16 and with two broken damper bars in fig 2.17.

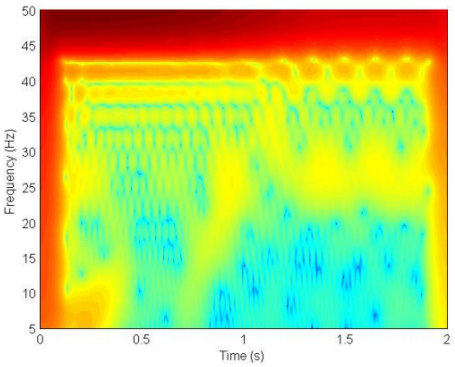

Figure 2.16: STFT of start-up current from a healthy generator [15]

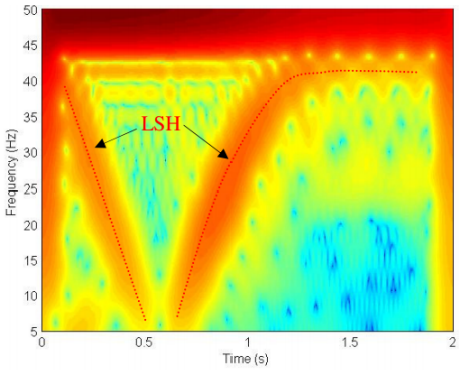

Figure 2.17: STFT of start-up current from a generator with two broken bars [15]

From the healthy case in fig 2.16 it is clear that there is a distinct difference between the healthy case and the case with two broken damper bars as seen in fig 2.17. The red dotted lines are the left sideband harmonics (LSH).

In the paper [16] the terminal voltage is used at switch-off in order to detect and distinguish between different types of eccentricity on a permanent magnet machine. It is shown that low and high-frequency components in the current spectrum are not sufficient to detect this type of fault in every different type of machine. This is because the low-order harmonics might come from the machine's inherent asymmetry or unbalanced load. The high-frequency components only work for particular pole pair and rotor slot combinations. High levels of static eccentricity can result in shaft flexing and dynamic eccentricity, masking the static eccentricity as mixed eccentricity. This has to do with the unbalanced magnetic pull (UMP) that the static eccentricity potentially generates.

The analysis of voltage was done by sampling at 35 kHz after the switch-off transients had died out. The window function used was Hamming window, and the sampling time was five cycles. The high sampling rate of 35 kHz was utilized to prevent aliasing. The result did show that it is possible to distinguish between different types of eccentricity. Static eccentricity led to changes in the odd harmonics as shown in fig 2.18 more specifically, the 17th, 19th, 21st, and 23rd harmonic, while dynamic eccentricity did show changes in the intermediate harmonics 22nd and 24th as seen in fig 2.19.

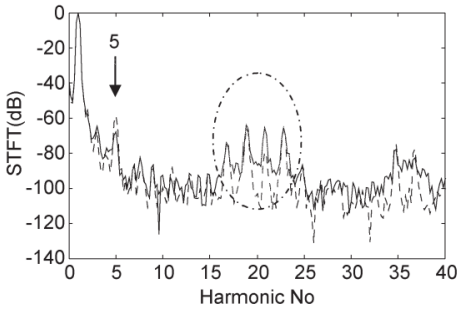

Figure 2.18: STFT of terminal voltage spectrum after switch-off with 60% static eccentricity [16]

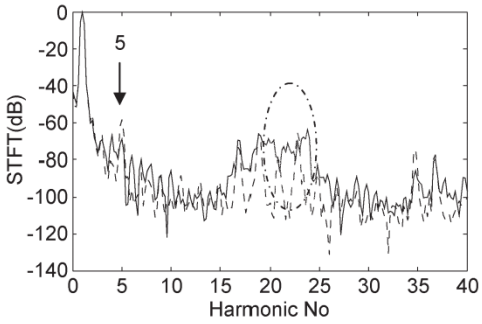

Figure 2.19: STFT of terminal voltage spectrum after switch-off with 60% dynamic eccentricity [16]

The dotted lines in fig 2.18 and fig 2.19 shows the healthy case. The spectrums are normalized with respect to the fundamental frequency 60 Hz.

A bearing fault is one of the most critical faults in many electrical drives. In [17] STFT is used to pre-process sampled acoustic emission (AE) to detecting bearing faults. After pre-processing, LAMSTAR neural network is utilized to detect a fault in the bearing. The result showed that bearing faults can be detected with similar accuracy as traditional methods with no need for specialized signal and feature extracting techniques.

2.5.4 Wavelet

Many applications need both accurate time and frequency resolution. STFT does not meet these requirements, and therefore the method wavelet transform was developed. Wavelet transform gives information about the frequencies as well as the location and magnitudes of the signal. Compared to Fourier-based methods, the wavelet transform method uses small waves as basis functions instead of truncated cosine and sinus waves. The use of wavelets gives the wavelet transform some advantages compared to STFT, such as a better description of anomalies, pulses, and other events that start and stop within the signal [18, p 2]. The small basis functions are called mother wavelets. The choice of the mother wavelet depends on the signal and which features that are studied. The concept is to take the complex dot product between the mother wavelet and the signal. This gives an output signal with a magnitude that increases with similarities between the mother wavelet and the signal. There are almost infinite mother wavelets to choose from. To choose the correct wavelet could possibly be time consuming, However each wavelet is stretched and shifted, making them extremely adaptable.[18, p 174]

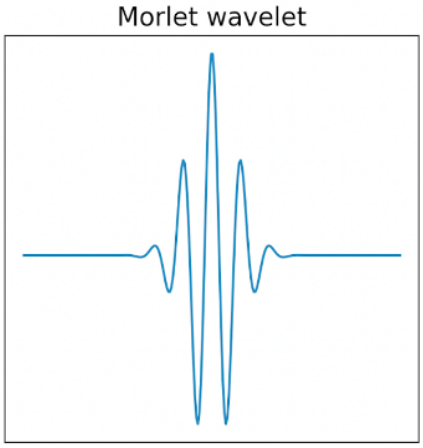

Figure 2.20: Morlet wavelet

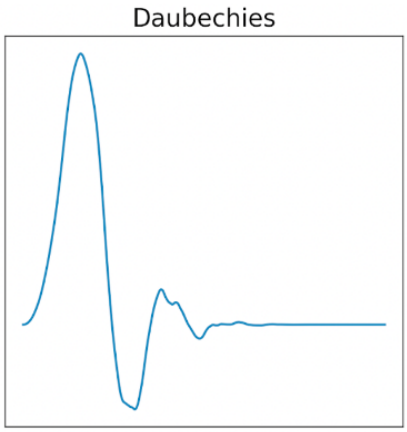

Figure 2.21: Daubechies wavelet

Although the wavelet is adaptable, there exist some guidelines on which wavelet to choose. A Shannon wavelet has good frequency resolution but is poor in detecting short-time events. This can be seen by observing the relative sharp cut-off frequency in the frequency domain. However, to be able to detect this a large number of points are needed. A 2-point Haar wavelet is good for finding concise events, but has a poor frequency cut-off [18, p 195]. Two types of mother wavelets that has been utilized in machine analysis [19] [20] are seen in fig 2.20 and 2.21.

In order to use a wavelet, some conditions have to be met for the wavelet to be valid. The Fourier transform of the wavelet squared has to be integrable

$$C = \int_{-\infty}^{\infty} \frac{|\psi(\omega)|^2}{\omega} \, d\omega < +\infty \tag{2.17}$$

ψ is the wavelet. This is known as the admissibility condition and states that the wavelet has an inverse, and one can reconstruct the signal without loss of information. Another condition is that the wavelet function need to have is limited energy:

$$E = \int_{-\infty}^{\infty} |\psi(t)|^2 \, dt < \infty \tag{2.18}$$

This ensures that the location of the different signals is possible to map. There are two main parameters in a wavelet transform other than specifying the mother wavelet. These are the wavenumber(ω) and the scale. In order to illustrate that this is the mother wavelet, Morlet described. The mathematical equation of the Morlet wavelet is given by:

$$\psi = \phi^{-\frac{1}{4}} e^{j\omega\phi} * e^{-\frac{-\tau^2}{2s^2}} \tag{2.19}$$

$\phi^{-\frac{1}{4}}$ is a scaling factor. $e^{\frac{j\omega\tau}{s}}$ is a complex sinus wave. $e^{\frac{-\tau^2}{2s^2}}$ is a Gaussian curve.

The wavenumber ω states the number of oscillations that the signal has between the tapering. When a wavelet transform is executed, the wavelet is stretched to fit the signal. This means that a wavelet with many oscillations needs to be stretched by applying a greater scale parameter to capture the low frequencies. A greater scale means that a greater portion of the signal is captured, resulting in a better frequency resolution and lower time resolution. Fig 2.22 shown below illustrates this: 2.23 illustrates this:

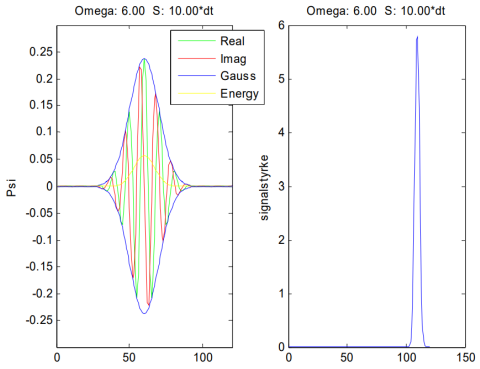

Figure 2.22: Morlet wavelet with a wide scale and good frequency resolution

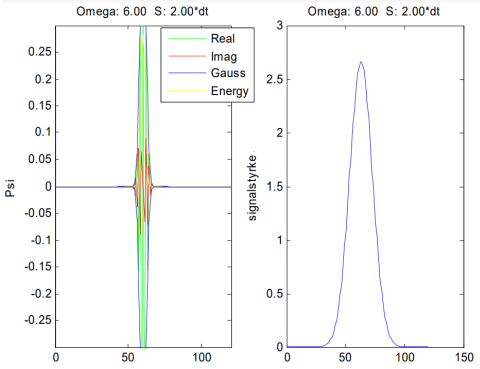

Figure 2.23: Morlet wavelet with a low scale and good time resolution

There are two main methods to compute the wavelet transform. These are continuous wavelet transform (CWT) and discrete wavelet transform (DWT). CWT is given by:

$$CWT(a,b) = \int_{-\infty}^{\infty} x(t) \frac{1}{\sqrt{a}} \psi(\frac{t-b}{a})\, dt \tag{2.20}$$

a and b are the scaling and shifting parameters. For each, a and b, there is a wavelet transform coefficient. This process gives a time-frequency representation that offers a good time and frequency localization. However, it is a heavy computation process to compute all the different coefficients. To be able to reduce the computation time, DWT was proposed. The idea is that one transforms stretch and shifts by the power of 2[18, p 19] and uses three additional filters to process the signal. The filters are constructed so that the noise is passed through the high-pass filter while the low-pass filters decompose the signal further. This filtering creates two signals per level of decomposition. According to the Nyquist rule, this should have half the point of the level above. Two parameters should be specified; the mother wavelet and the number of decomposition levels. Fig 2.24 shows the decomposition of a chirp signal.

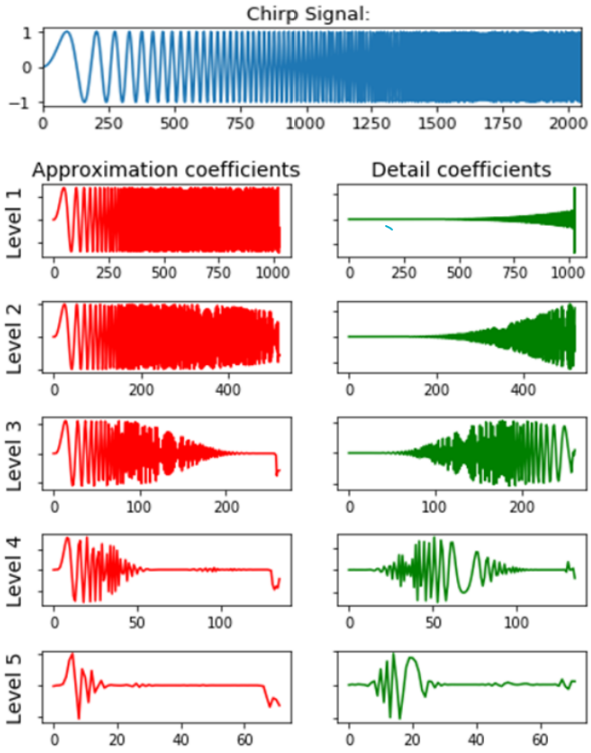

Figure 2.24: Decomposition of a chirp signal: Source adapted from [21]

The wavelet transform has been used to investigate the effect of broken damper bars. [22] uses an intelligent method that combines the use of DWT with Meyer wavelet and nearest neighbor classifier. DWT isolates the faulty component in the start-up current, and symbolic analysis transforms this into useful information. The method showed promising results in detecting whether there is a fault or not.

In [19] CWT is used to analyze the stator signal on a permanent magnet machine (PM). The decomposed signal from CWT is used to form a linear combination of the energy, peak, head angle of the peak, area below the peak, and the peak gradient. CWT was chosen since PM motors are usually driven by power electronics that generate different harmonics. Furthermore, a big PM machine is usually not driven in full load and with lighter loading it is generally not the frequency spectrum sufficient for an accurate diagnosis. The mother wavelet was set to be Daubechies 6 (db6). By reducing this classifier with Principal component analysis (PCA) and applying the machine learning algorithm, Fuzzy support vector machine (FSVM) it was possible to estimate the eccentricity type and degree even with a high noise level (S/N = 20 dB).

Analyzing the stator current with DWT is prone to fundamental components spread across the decomposition's and thereby making the fault diagnosis harder. Paper [20] propose a

method where one is using an adaptive filter to remove the fundamental components in the stator current. This is done by measuring the data in real-time and then estimate the frequencies. The estimatation of frequencies was done by an algorithm known as Estimation of signal parameters via rotational invariant techniques (ESPRIT). After that is DWT used on the residual signal with Meyer wavelet as the mother wavelet and six degrees of decomposition. This is chosen by applying a grid search algorithm to minimize the classification accuracy. In order to classify the result, the support vector machine classifier is used with radial basis function. This method gave an accuracy of 96% in simulation and experimental data and is the adaptive filtering did improve the overall accuracy.

Chapter 3

Generator

The generator that is modeled and used to verify the results of the simulations in this thesis, is a slip ring salient pole synchronous generator rated at 100 kW. It is placed in NTNU's National Smart Grid Laboratory in Trondheim, Norway. The generator is made to resemble a down scaled hydro generator that is commonly used in the Norwegian power system. The rotor has 14 poles, this is the second most common pole number of a hydropower generator in Norway. The rated values of the generator are given in the table below.

Table 3.1

Nameplate rating			
Power	P_n	100	kW
Speed	n_n	428	RPM
Voltage	U_n	400	V
Current	I_n	144.3	A
Frequency	f	50	Hz
Power factor	P.F.	0.9	
Efficeny		90.8	%
Exciation voltage	U_e	20	V
Excitaiton current	I_e	103	A
No-load exc. current	I_en	56	A
d-axis s. reactance	X_d	2.040	Ω
q-axis s. reactance	X_q	2.075	Ω

Specifications			
Number of slots	N_s	114	
Number of poles	N_p	14	
Number of slots per pole per phase	N_spp	2.71	
Damper bars per pole		7	
Winding layers		2	
Turn per pole		35	
Stator diameter	D_s	780	mm
Rotor diamter	D_r	646.5	mm
Nominal air gap length	g	1.75	mm
Winding connection		Wye	

The generator is built to operate under various operating conditions, including faulty conditions. The following modifications can be done to the machine to simulate different types of faults:

- The stator frame can be moved in order to impose static eccentricity.
- Up to 10 of the rotor windings can be short circuited on two poles, to simulate inter-turn short circuit.
- The damper bars can be removed.

This gives a unique possibility to investigate how different types of faults will affect a real machine.

Chapter 4

FEM model

It has been shown that it is possible to simulate the shaft voltage of a turbo rotor synchronous generator as a 2D model [23]. In this report a similar method is used to simulate the shaft voltage in a salient pole generator. Generally would it be sufficient to model a section of the machine and thereby reduce the simulation time. The faults will distort the magnetic symmetry in the machine. Therefore, it is necessary to model the entire cross-section. The simulations are done in ANSYS Electronics. This is a finite element analysis (FEA) software package that can solve electromagnetic field problems. The problems are determined by solving Maxwell's equation in a finite region of space called mesh points [24]. The initial computer-aided design (CAD) model of the generator has been developed and verified experimentally in the Smartgrid lab [25]. The rotor is modeled only with the poles and rotor yoke, therefore the shaft had to be modeled.

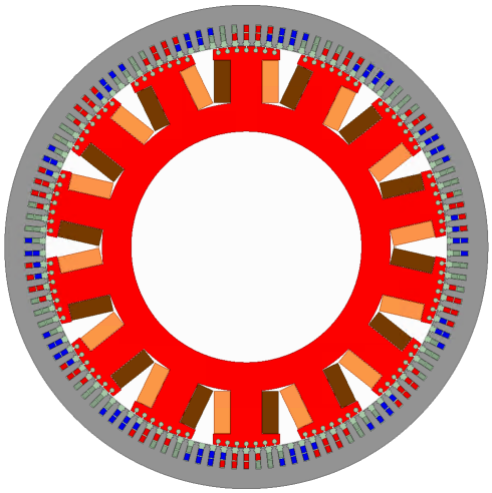

Figure 4.1: The initial generator

Schematic of the rotor A.1 states that shaft has a diameter of 110[mm]. The way it was

modeled was to first extend the rotor with the rotor core shown in fig 4.2.

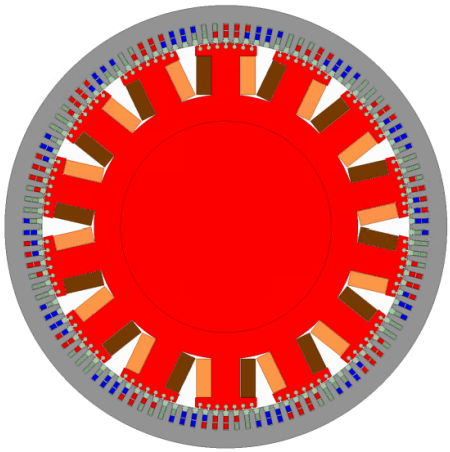

Figure 4.2: CAD model of the generator with rotor core

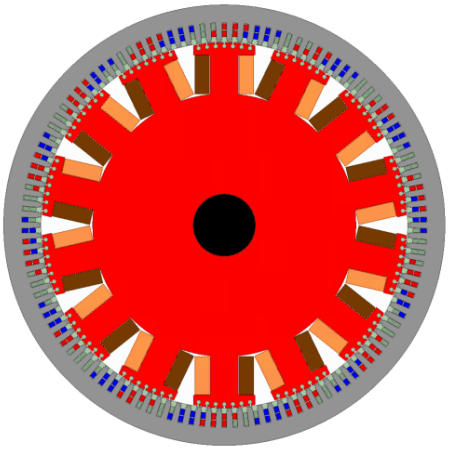

Figure 4.3: CAD model of the generator with the shaft marked in black

Then was the shaft modeled, and the shaft subtracted from the rotor area as shown in fig 4.3 to get the exact boundary that Maxwell needs [24]. The chosen material was stainless steel, which is a pre-defined material in the ANSYS library. According to [23] the choice of material has a negligible impact on the simulated shaft voltage. The accuracy of the model depends on the number of mesh points [24]. The theory is that to describe a field quantity each element must occupy a small enough region for the field to be adequately interpolated from the nodal values. This means that the mesh is usually manually defined based on the problem and intuition of where finer mesh may be needed. It has been shown that the number of mesh points needed for an accurate but no too time-consuming analysis is somewhere between 200,000 and 250,000 points [7]. Therefore, the exact location of the mesh points and the value were tested to represent the shaft voltage accurately. Two types of mesh densities in the rotor and shaft were tested out. The rest of the model has the same mesh distribution and the number of elements as fig 4.1. One type with 196,752 number of mesh elements in fig 4.4 from now on called mesh 2e5 and one with 246,324 number of mesh points from now on referred to as mesh 2.5e5 as in fig 4.5.

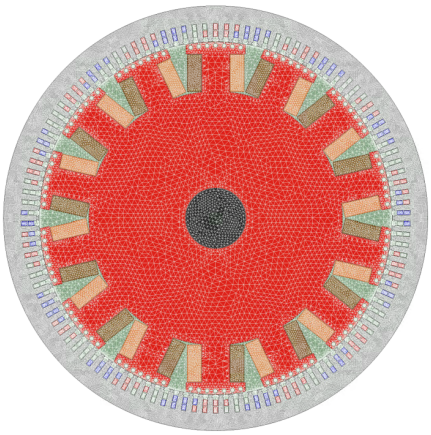

Figure 4.4: Generator with 196,752 number of mesh points

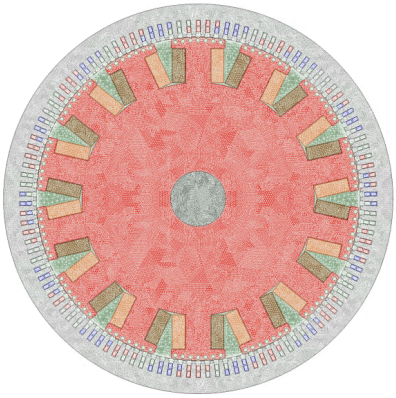

Figure 4.5: Generator with 246,324 number of mesh points

The resulting shaft voltage from running the FEA of mesh 2.5e5 and mesh 2e5 with a sampling frequency of 10,000 Hz for 1.14 sec is seen below:

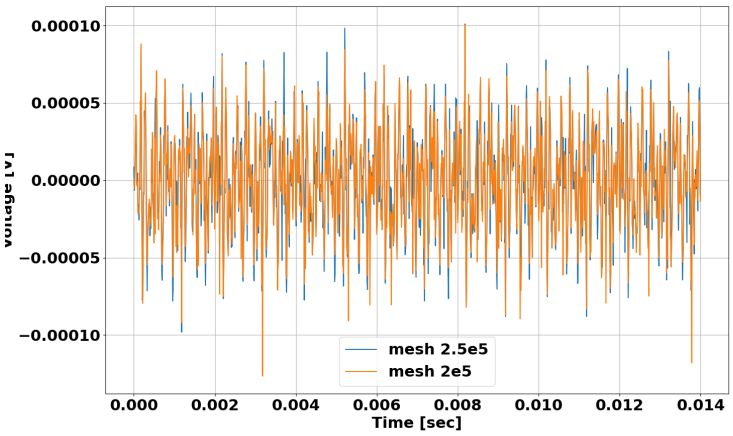

Figure 4.6: Plot of the shaft voltage, mesh 2e5 and 2.5e5

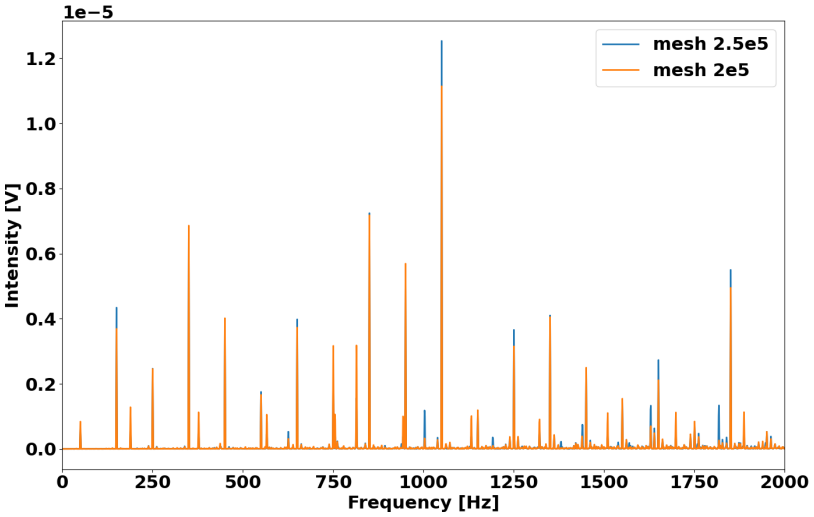

Figure 4.7: Spec of the shaft voltage, mesh 2e5 and 2.5e5

The two plots look similar. Based on the Fourier transform, the differences are the magnitude of some of the frequencies. However, since the running time was comparable, the plot with 2.5e5 number of mesh points was chosen because it is presumed to give a more accurate result. To measure the induced voltage in the shaft, the rotor is modeled as one solid coil. The coil is then modeled as a coil with "external excitation" in order to model the shaft and the measuring equipment with an equivalent circuit as shown in fig 4.8. Finally, the shaft is modeled as equivalent inductance grounded to the left, and the right is connected to an impedance with high resistance ($10m$) that does not impact the shaft voltage.

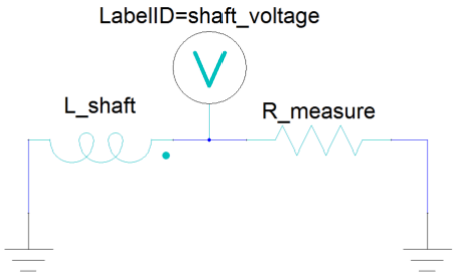

Figure 4.8: Circuit of the shaft measurement

4.1 Initial results

First a case with severe faults was simulated. More precisely ten short-circuited coils on one pole. The field current was initially set to 53.5 A. This field current should give a nominal voltage at the terminal when the generator runs in a no-load situation.

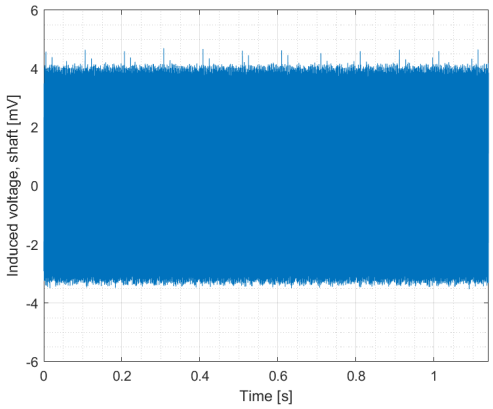

Figure 4.9: Shaft voltage with 10 ITSC

The amplitude of the signals is low as seen in fig 4.9. This means that they are potentially hard to detect. It was therefore chosen to try the field current that gave the nominal voltage under a no-load situation in the actual generator and also make a model of the generator housing similarly to [23].

4.2 Generator housing

Modeling of the generator housing is regarded as a 3D problem [26] however, the housing is radial outwards from the stator. As seen in the green section on fig 4.10 the housing is relatively homogeneous around the stator. The housing is therefore modeled as the cross-section of the housing.

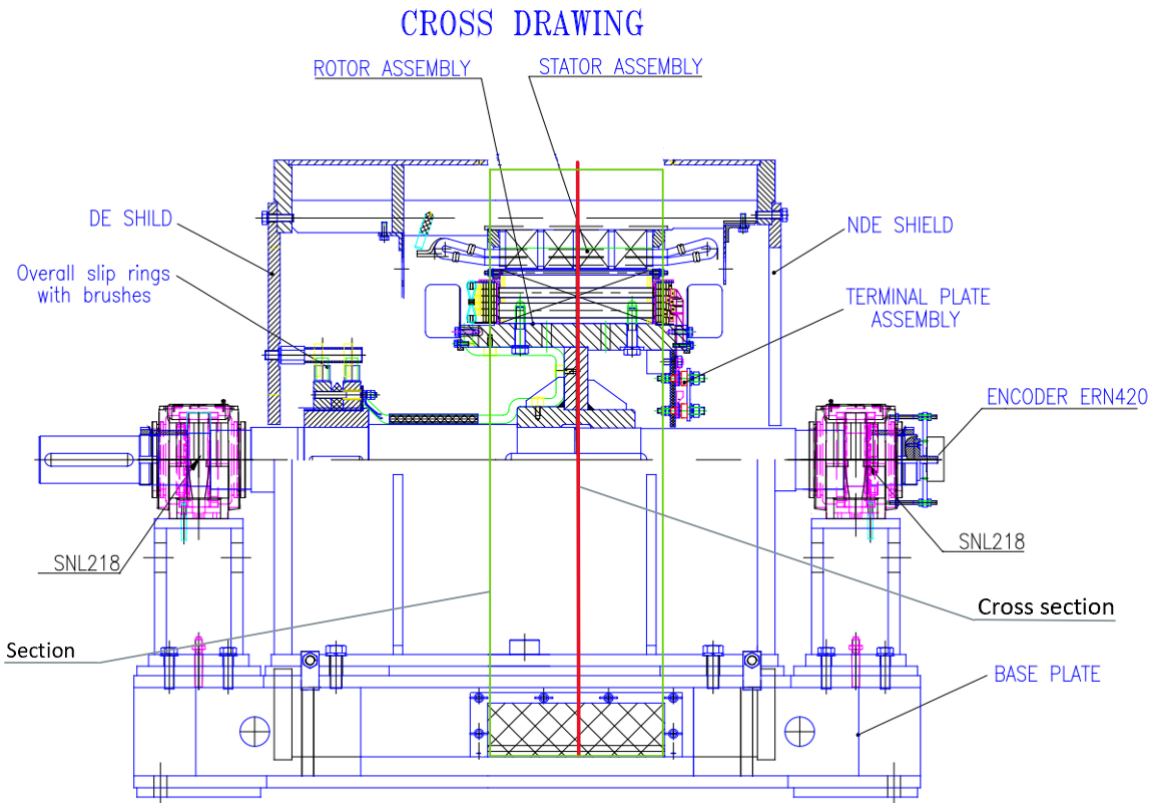

Figure 4.10: Cross drawing of the generator

The drawing and specification A.2 did not state all the dimensions needed to make a 2D cross-section model of the generator. Measurements of the housing were therefore taken in corporation with technical staff [27].

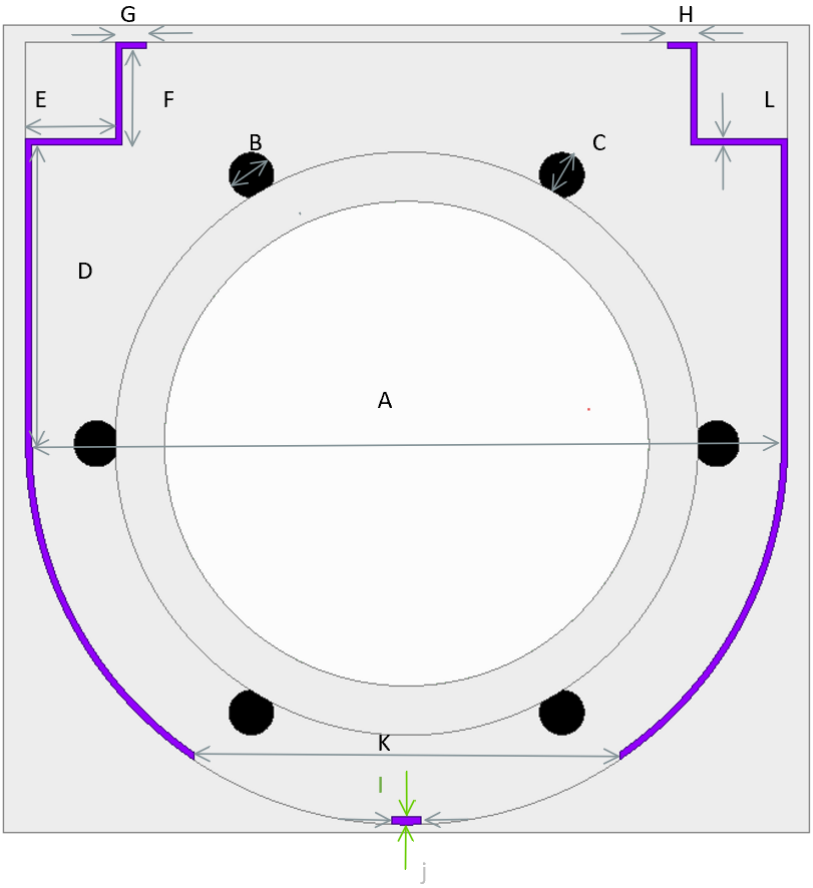

Figure 4.11: Generator house

Measurements					
A[1]	1002.82	[mm]	G	41.1	[mm]
B[2]	60	[mm]	H	40.5	[mm]
C	55	[mm]	I	11	[mm]
D	399.97	[mm]	J	37	[mm]
E	120.62	[mm]	K	570	[mm]
F	128.8	[mm]	L	8.5	[mm]

Each item was modeled as a solid coil and then connected in one coil to get the total induced voltage. The measurement circuit was modeled equal fig 4.8. This made it easy to distinguish between the two voltages and to look at each part's effect on the total shaft signal.

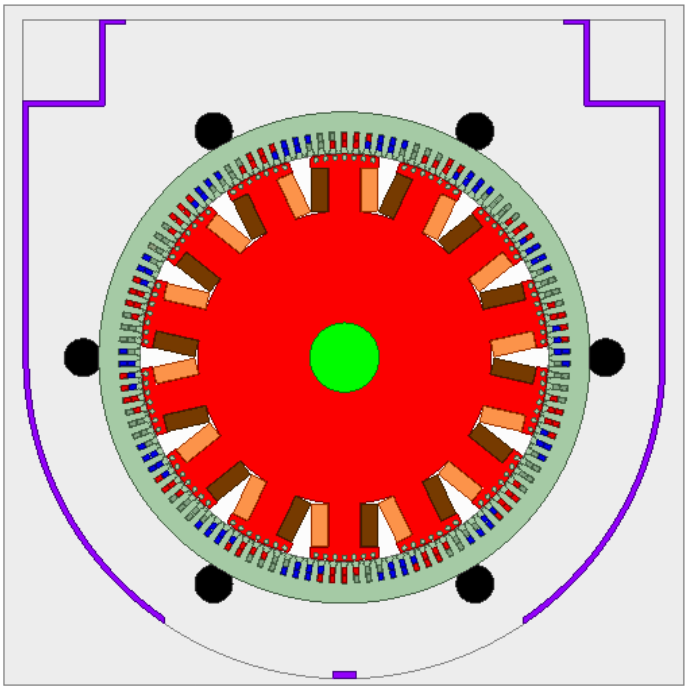

Figure 4.12: Generator model with shaft and housing

4.3 Mesh

The housing and air inside the housing have to be partitioned in mesh points and have a similar compute time as in fig 4.5. To have the total number of mesh points around 2e5, the number of mesh points in the rotor and shaft has to be decreased. The range between fig 4.5 and fig 4.4 is a relative wide gap. This made it possible to decrease the mesh points down to fig 4.4 in the model with shaft fig 4.3 and then distribute the restoring mesh points to the housing and air between. This gives a model with 247,631 number of mesh elements, where the distribution is shown in fig 4.13

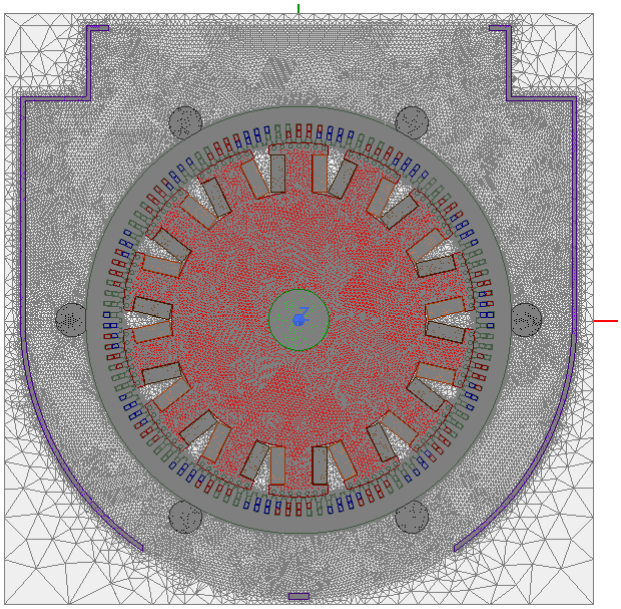

Figure 4.13: Plot of the mesh to model that includes the shaft and housing

4.4 Load

When the machine is connected to a load, an armature current flows in the stator winding. The combined effect of all the stator current exhibits an armature, MMF, that rotates with the frequency. Combined with the field, MMF gives this the resulting MMF that drives the air-gap flux. It can be seen that the armature reaction demagnetizes the generator, and the resulting MMF is smaller than the rotor MMF alone. Therefore, the magnetization current has to be increased as the load increases. An increase in load will typically give a slight flattening of flux density, which results in a third harmonic [28, p. 80]. In order to investigate what impact this has on the shaft voltage, the generator was connected to inductors and resistors as seen in fig 4.14. The resistance was set to $R = 2.78$, the inductance to $L = 22mH$, and the field current was set to $84A$ [7]. This gives an output power of $65kVA$.

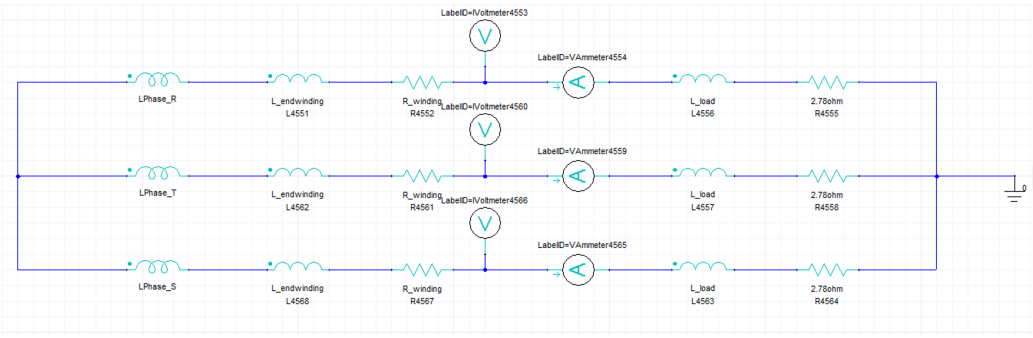

Figure 4.14: Equivalent circuit of the generator connected to a passive load

4.5 Connected to grid model

Salient pole synchronous generators are usually connected to a power system consisting of many other synchronous generators and loads. These are linked together by a transmission network. Typically, the generator's power rating is many times lower than the sum of all the other generators combined. The transmission grid is then described as solid or stiff. Its mechanical inertia and impedance determines the strength. A way to define the strength of the grid is Short-circuit ratio (SCR) [29]. It is defined as the ratio of the maximum apparent power of the grid to the rated power of the grid:

$$SCR = \frac{S_grid}{S_G} \tag{4.1}$$

A strong grid is defined as a grid with $SCR > 5$ and a weak grid is defined as a grid with $SCR < 3$.

$$S_{grid} = \frac{U_{LL}^2}{Z_g} \tag{4.2}$$

U_{LL} is the nominal line voltage, and Z_g is the grid impedance at the connection point. The NTNU lab generator with S_n of 100 MVA and given an SCR of at least 5 gives an Z_g of $0.8m$ or less. The impedance is therefore neglected, and the stiff grid is modeled as an ideal voltage source as seen in fig 4.15.

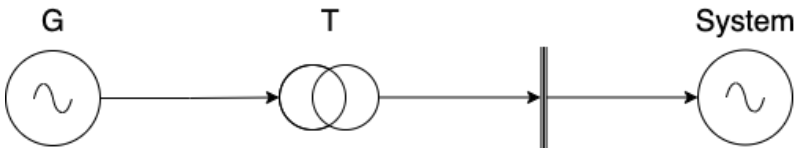

Figure 4.15: Schematic of a generator connected to a stiff grid

It is also possible to model a weak grid that has an SCR below 5. However, SCR measure how easily the terminal voltage is affected during a dynamic system event. This thesis is limited to detecting fault during steady-state operation, and modeling a weak grid is therefore not a part of this.

The power output of a salient pole synchronous generator is given by:

$$P = \frac{E_q V}{x_d} sin\delta_{gt} + \frac{V^2}{2} \frac{x_d - x_q}{x_d x_q} sin2\delta_{gt} \tag{4.3}$$

E_q is the induced voltage in the armature, x_d is the synchronous reactance in d-direction, and x_q is synchronous reactants in q-direction. V is the output voltage. δ_{gt} is the power angle, the angle between the induced voltage and the terminal voltage. The power output of the simulated generator is controlled by warring the power angle. The way to do it is to specify the phase angle of the ideal voltage source, so the phase angle between the induced voltage corresponds to the desired power output. More specifically, first it is needed to find

the phase offset of the no-load voltage by running it in no-load condition. Then is it possible to measure the time for the first peak and then the phase angle:

$$\phi = -\pi/2 + \omega t_{peak} \tag{4.4}$$

$\omega = 2\pi f$ and t_{peak} is the time when the first positive peak occurs. Then by plotting equation 4.3 as a function of power angle from 0 power to rated power and taking the phase offset into account, is it possible to control the amount of power that the generator delivers in the simulation. The plot is seen in fig 4.16

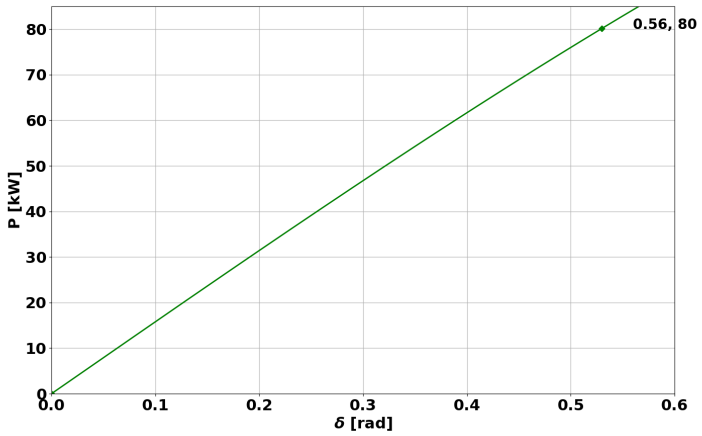

Figure 4.16: Power-angle characteristic

The voltage sources was then connected in star connection fig 4.20 and an angle of 0.56 was set as the phase offset in the equation of the ideal voltage source. The angle gives a output of $80kW$. This was then simulated with a sampling frequency 1,000 Hz for 1.14 seconds.

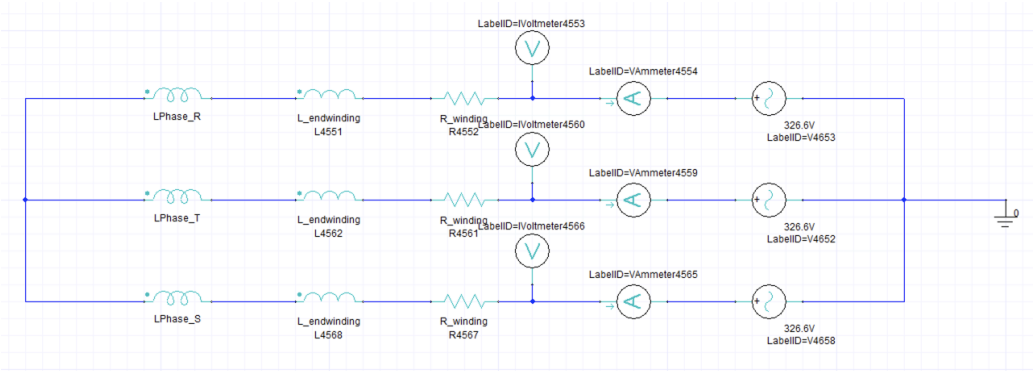

Figure 4.17: Equivalent circuit of the generator connected to ideal voltage sources in star connection

The phase current at the terminal is then:

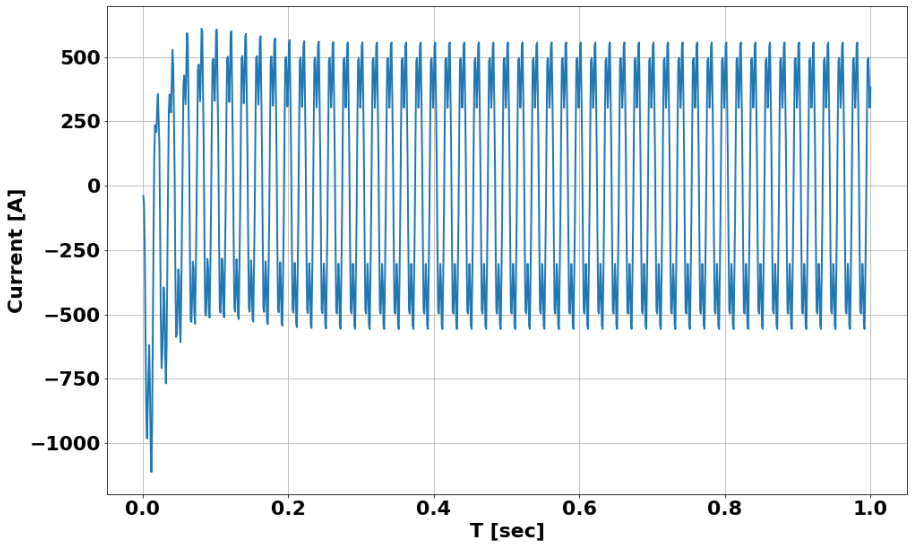

Figure 4.18: Stator current when the generator is connected in star-connection

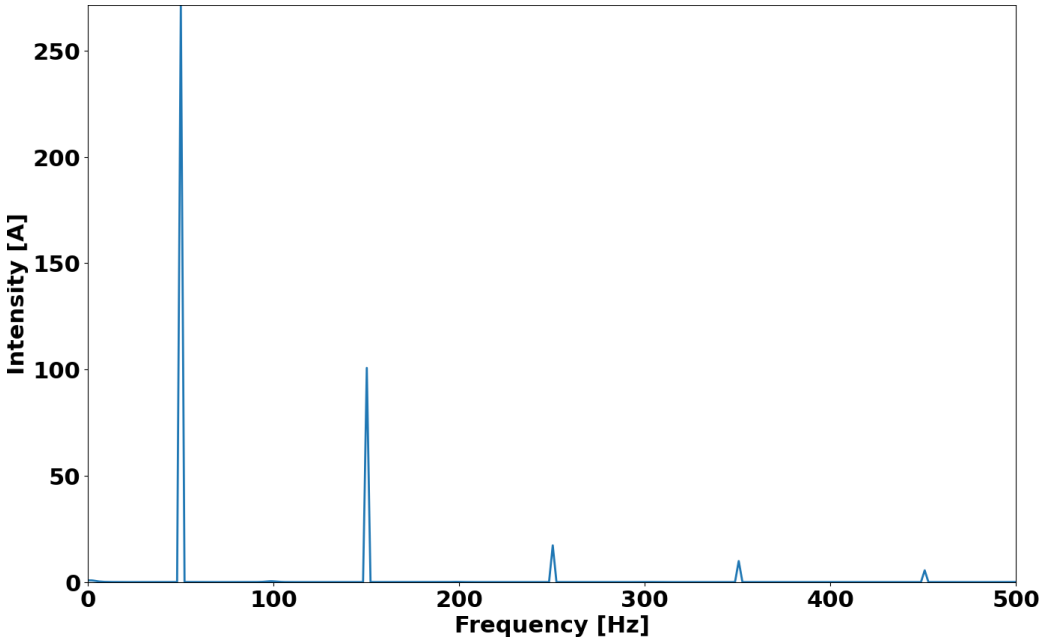

Figure 4.19: Fourier transform of the stator current when generator is connected in star-connection

By looking at the Fourier transform, it is clear that the signal contains a third harmonic component. This could be filtered out by connecting the voltage sources in delta connecting [28]. Delta connection in ANSYS requires that one is connection a passive component in series with the ideal voltage source [30] in order to make it converge to a solution.

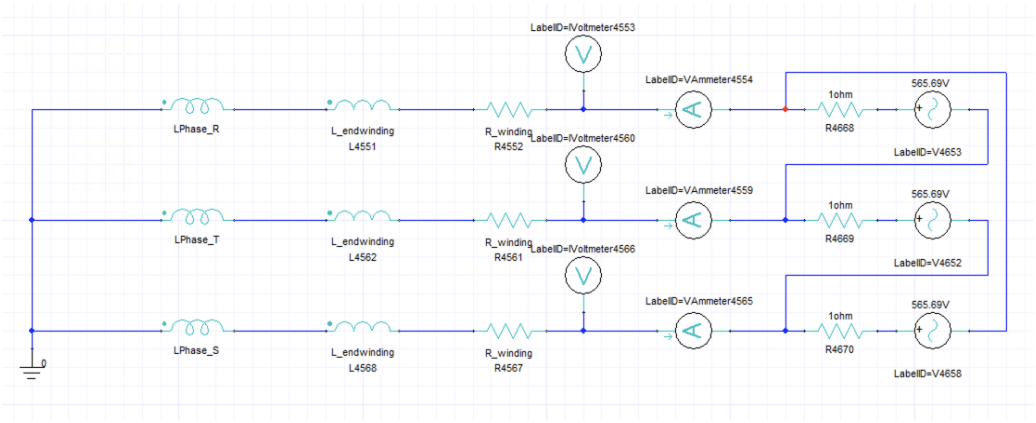

Figure 4.20: Equivalent circuit of the generator connected to ideal voltage sources in delta connection

4.6 Shaft material

By comparing the continuous wavelet transform of the laboratory and simulations results for frequencies around 814 Hz, it was discovered that the pattern is different. The problem was overcome by changing the material in the housing and shaft. Stainless steel is the first material that was used. The material has a constant relative permittivity of 1 that is similar to air. It was chosen because the manual of the generator did not specify which type of material that was used in the real generator and constant relative permittivity makes the simulation faster than a ferromagnetic material with a B-H curve. It was then proposed to use steal 1010, which is the same ferromagnetic material used in the rotor yoke. The simulation did then give a similar pattern as the laboratory measurement. Therefore, it was decided to use this material for all simulations.

Chapter 5

Laboratory Setup and Shaft Measurement

The first part of this chapter contains a description of the laboratory setup at the Smart grid laboratory. Then follows a section about how the generator was operated when the shaft voltage was measured. The third part of the chapter covers how the measuring was done and the process of finding the best and easiest way to get consistent and high-quality results.

5.1 The laboratory setup

The laboratory setup consists of the generator, an induction motor, and required converters. The generator can be operated under several faulty conditions. It has a low air gap of $1.75mm$ that increases the effect of the inter-turn short circuit in the field windings [26]. Stepwise, this is done by connecting a metal rod on terminals that corresponds to a different number of field winding seen in fig 5.1.

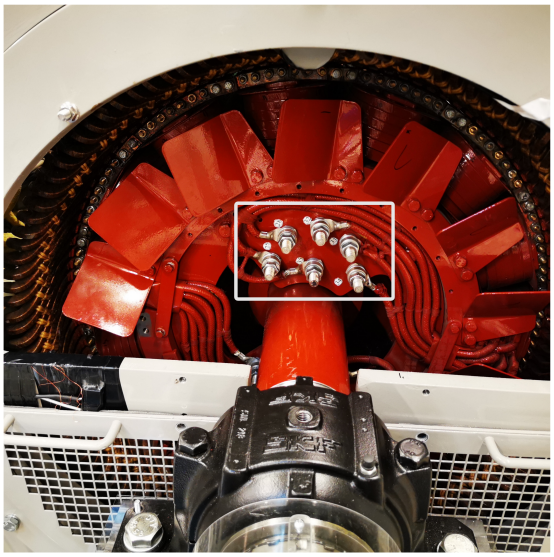

Figure 5.1: Short circuit terminal inside white box

Turns can be shorted in the two poles on the opposing sides of the generator.

Static eccentricity can be imposed by altering the position of the generator housing. The housing position is altered by changing the screw on the side of the generator housing seen in fig 5.2.

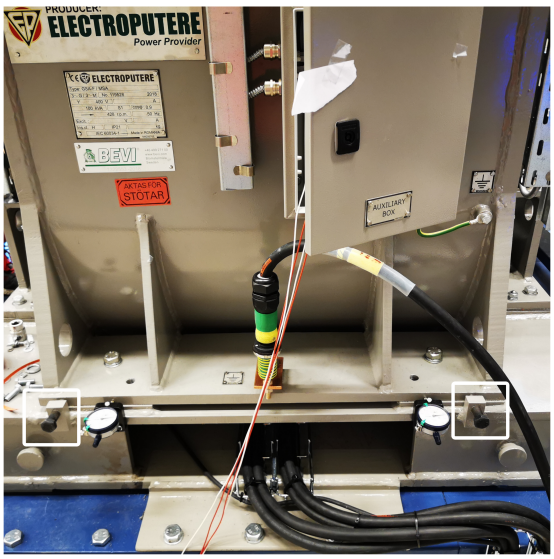

Figure 5.2: Screws that change the position of the stator inside the white boxes

The correct position is determined by looking at the pressure gauges beside the screws. Due to the small air gap, there is a risk of stator rubbing. It is therefore important to inspect the stator before running with an altered housing position.

Dynamic eccentricity can currently not be tested in the laboratory. To be able to do this, it would be needed to implement a special bearing from AB SKF. Such bearing was not available during the test period.

The generator is driven by a 90 kW, 400 V induction motor with four poles and at a rated speed of 1,482 rpm. The shaft is connected to the generator by a gearbox that has a conversion ratio of 1,485 rpm to 375.95 rpm. This means that at rated speed the generator would produce electrical power with a frequency of $\frac{375.95 \cdot 14}{P \cdot 2} = 43.86Hz$. That is below 50 Hz of the grid. This is because the setup was originally designed for a generator with 16 poles. The induction motors then have to operate at a frequency of:

$$N_{motor} = \frac{P}{2} f_{el} 603.75 = 1693.85rpm. \tag{5.1}$$

The converter driving the induction motor only accepts a speed input of integers, therefore 1,693 rpm was chosen.

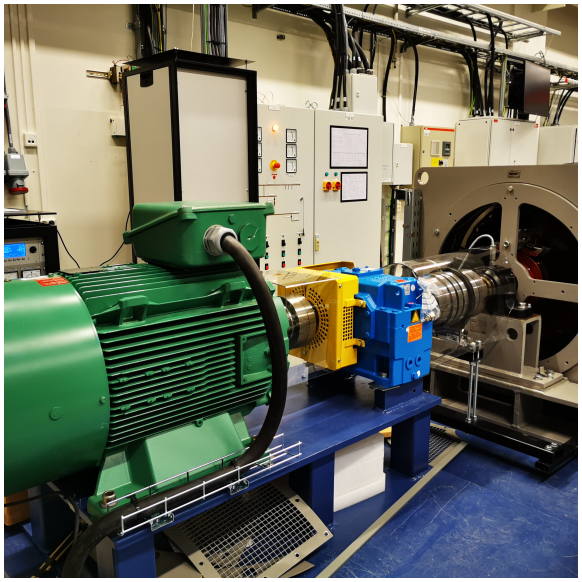

Figure 5.3: Picture of the induction motor and the gearbox

5.1.1 Excitation and converter

The induction motor is controlled by a three-phase 60 kVA converter made by SINTEF Energy. The rated value is below the rated output of the 100 kVA generator by a good margin . However, it is possible to exceed the rating for a short period to operate the generator up to the nominal operation. The converter is operated by setting the reference speed at the preferable speed for induction motor rotate at.

A rectifier made by SINTEF Energy supplied the excitation. The field current at no-load is $53.2A$, and at rated load, it is $103A$. This current is adjusted manually at the terminal

of the DC source.

5.1.2 No-load and load setup

The no-load measurement was done by adjusting the speed gradually up to rated speed and adjusting the excitation current until a terminal voltage of 400 V can be read. The healthy condition was at about 56 A, which is higher than the manufacturer's documentation.

The load measurements were done when the generator was connected to the grid. For it to be connected to the grid the generator has to be running in no-load condition, and the rated voltage has to be applied on the terminal. Then it is a matter of connecting it to the grid when the synchroscope shows that the rotor field is in sync with the network phase. When the generator is connected, the active power is adjusted by adjusting the speed reference above the nominal value. The active power is then displayed on the excitation converter. The reactive power is adjusted by adjusting the field current. The three types of load that were used are:

Load	$I_f[A]$	$\overline{P}[kW]$	$\overline{Q}[KVAR]$	$\overline{S}[kVA]$	N [rpm]
NL	56	0	0	0	1963
FL1	63	39.5 ± 4.4	0.15 ± 0.16	39.6 ± 4.2	1701
FL2	87	64.4 ± 7.5	$3,89 \pm 1.45$	$68,3 \pm 6.2$	1707
FL3	94	78.8 ± 4.6	4.7 ± 0.95	83.5 ± 3.9	1711

The AC power values shown in table above are average values of some of the measurements since the gird is fluctuating and the inverter feeding the induction motor is controlled by specifying a rotational speed reference.

The speed reference and excitation current have to be adjusted in incremental steps to avoid running into any slipping problem. Slip in a synchronous generator means that synchronism is lost, and mechanical shocks occur at the shaft. Slip typically occurs when a field current is too low compared to the applied torque [31].

5.2 Measurement setup

Shaft voltage is a potential difference between the shaft and generator housing. A voltage of a given magnitude will typically result in a current running through the bearing, and potentially damaging it. A counter measurement against this is to isolate one of the bearings, hindering a current bearing path. The lab generator was supposed to have one isolated bearing from the factory. Unfortunately, that was not the case. The solution was to lift the shaft and install a thin epoxy plate between the bearing and the stand of the shaft. Conducting paths between the bearing and the frame was also isolated. This includes bolts that connect the bearing with the stand. The temperature sensor and the cable to

the rotational sensor were removed.

5.2.1 Shaft measuring

The first proposed method of measuring the shaft voltage was to measure the shaft voltage with a probe connected to the bearing (A) and grounding it in the stator frame (B) as shown in fig 5.4.

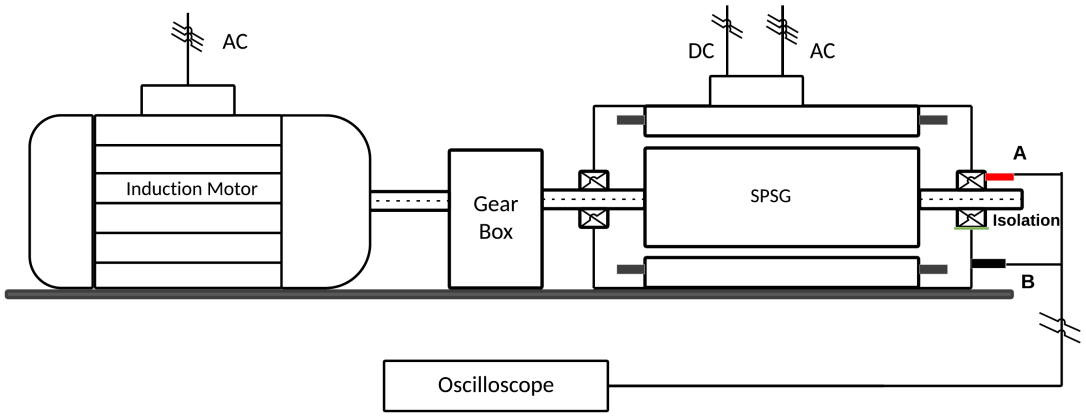

Figure 5.4: Schematic of the lab setup

This solution was proposed as a first choice of method because it is easier to connect a probe to the bearing than to the shaft where it would be needed to have a brush. The signal was measured with Tektronix MSO 3014. Unfortunately, the oscilloscope did not produce good results. The Fourier transform of the signal in fig 5.5 showed that the signal contains too much noise.

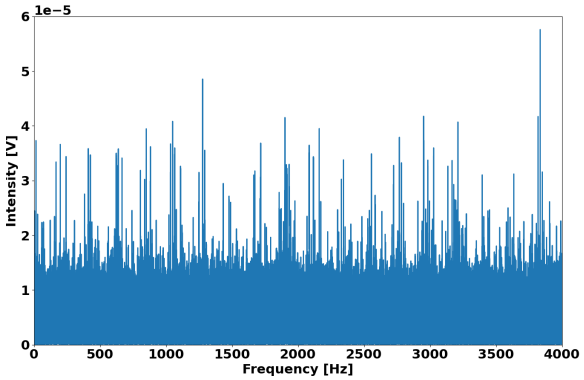

Figure 5.5: The amplitude spectrum of the shaft voltage measured at the bearing with the Tektronix scope

Therefore, it was proposed to use another oscilloscope with half the amount of noise floor compared to the Tektronix. In fig 5.6 it can be seen that the amount of noise is reduced. The noise is reduced, but it was impossible to distinguish between the different types of faults as seen in fig 5.7. The measuring point is on the bearing connected to the shaft through the grease surrounding the ball bearings. At nominal operation is the generator operating at 428.4 rpm. Then the lubrication grease will expand due to hydrodynamic effects. The lubrication grease has isolating characteristics and thereby is the bearing acting as a capacitor.

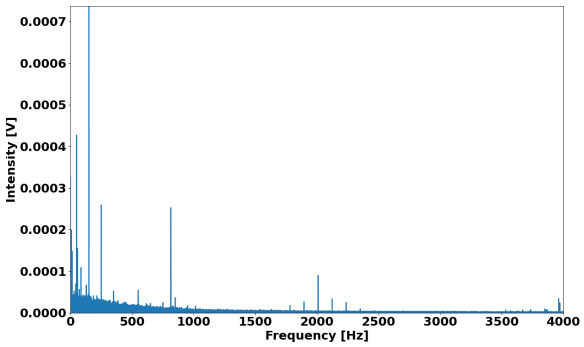

Figure 5.6: The amplitude spectrum of the shaft voltage measured at the bearing with the r scope

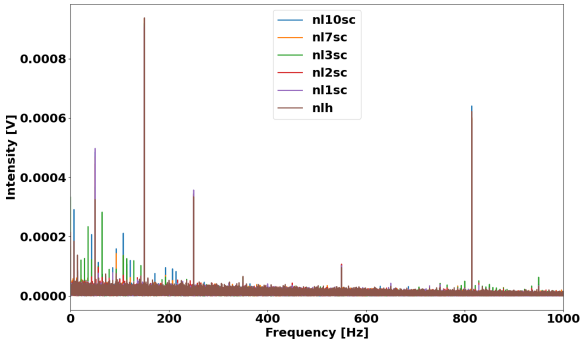

Figure 5.7: The amplitude spectrum of the shaft voltage comparing no-load with 0, 1, 2, 3, 7, 10 inter-turn short circuits

The voltage was then measured directly at the shaft with a graphite brush. The brush and the holder are seen in fig 5.11 and fig 5.10, and it is connected to the generator by a magnet.

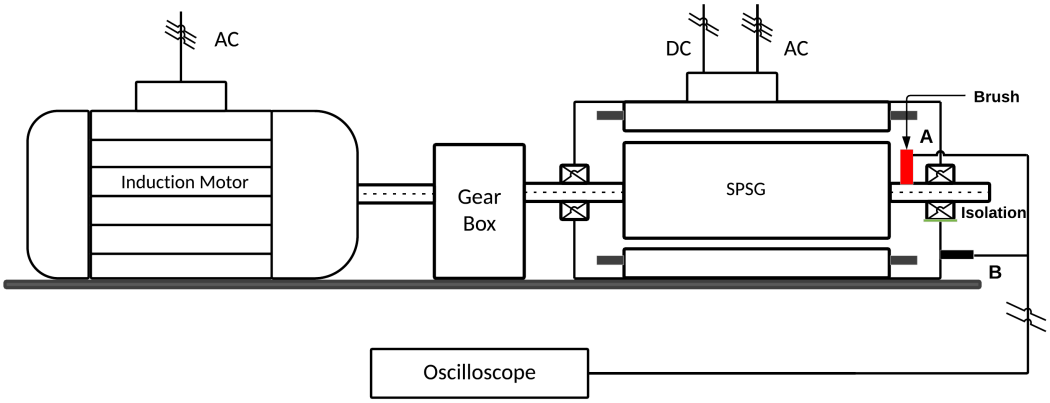

Figure 5.8: Schematic of the lab setup with a brush on the shaft

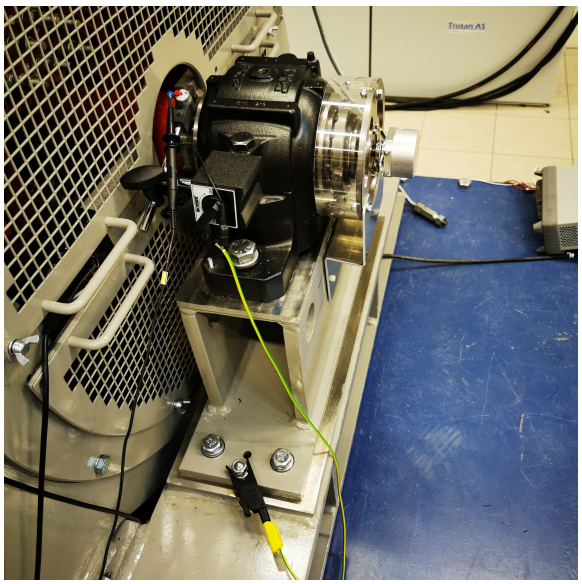

Figure 5.9: Brush mounted on generator

Figure 5.10: Brush-holder

Figure 5.11: Graphite brush

Continues wavelet transform of the results around 814 Hz shows that the magnitude is not stable. To have a stationary signal is crucial to have a constant voltage drop across the brush. A possible reason was that the spring was too soft, so that the contact area with the shaft changed during the operation, thereby changing the voltage drop. A new and stiffer spring was made, but it could not be distinguished between the old and new measurements. There was a slight change in the signal when the brush was pushed towards the shaft. With the spring pushed down, the voltage drops across the brush reduced to around 3 compared to 10. The signal has a magnitude of around 100 mV, so a significant change in resistance impacts the signal. In order to reduce the voltage drop across the brush a new brush was ordered. The new brush consists of 80% silver and 20% graphite. It has a much lower voltage drop measured to $47m$. Silver graphite brushes are brushes that are commonly used for signal transferring due to their low voltage drop and because the resistance is not as dependent on the temperature of the brush as graphite brushes [32]

Figure 5.12: Silver graphite brush

This gave a time-series plot of:

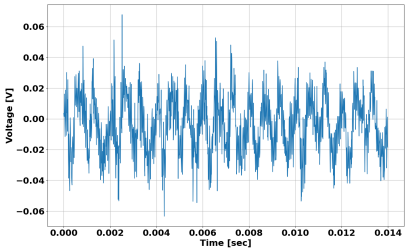

Figure 5.13: Time series plot of the healthy signal in no-load

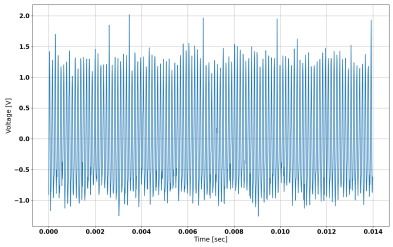

Figure 5.14: Time series plot of the shaft voltage with 3 short-circuited turns

It is not possible to distinguish between different types of faults. Signal processing in the form of Fourier transform, wavelet transform and short-time Fourier transform was utilised.

5.2.2 Signal Processing of the shaft signal

The signal was sampled at frequency of 10,000 Hz over a period of 40 seconds. The sampling frequency is the same as the one used in the FEM simulation. The rotational nature as well as a varying air gap will give a signal that varies with time. It was therefore imposed to use STFT and Continues wavelet transform in order to capture this. FFT of the no-load simulated and the measured signal did reveal that a frequency of 814 Hz did increase with the number of ITSC. This frequency is known as the slotting frequency, and it is the mechanical

rotation frequency multiplied with the number of slots. Short-time Fourier transform and Continues wavelet transform was therefore calculated in the range $795Hz$ to $825Hz$. Continues wavelet transform is a process that usually takes a long time to compute, restricting it to a small frequency bound greatly reduces computation time. In order to compute the CWT it is needed to specify a mother wavelet. The concept is that the mother wavelet should be as equal to the signal or pattern of interest. With a signal like in fig 5.13 It is impossible to know which mother wavelet that looks like the shaft signal. Further different wavelets were tested until the mother wavelet that made it easy to distinguish between the different faults was found. Complex morlet wavelet with a center frequency of 814.2 Hz and a bandwidth of 5 Hz gave the best result. By looking at the frequency response of morlet, it is something of a middle ground compared to the sharp cutoff of Shannon wavelet and the poor cutoff frequency of 2-point haar.

Short-time Fourier transform is a faster method than the CWT. However, as mentioned, there are more parameters to specify. It was decided to not account for these parameters in this thesis.

Chapter 6

Results

In this chapter the results from running the generator is presented, and the results are compared with the results from the finite element modeling. To detect the different types of faults, different types of signal processing are applied to the shaft signal. The first method is a time series plot that plots the voltage variation concerning time. The second method is a spectral analysis in the form of a Fourier transform of the signal. In the third method, there will be a wavelet transform, the type used is the continuous wavelet transform.

Fourier transform is taken over the whole spectrum of 40 seconds, which gives a resolution of 0.025 Hz 2.5.2. CWT was utilized with a complex morlet wavelet. After a trial-and-error process, and by looking at the spectrogram, a center frequency of the slotting frequency (814.4) and a bandwidth of 5 Hz turned out to give the best results.

6.1 Excitation current

Fig 6.1 and 6.2 shows the amplitude spectrum of the shaft voltage that compares running the machine in healthy conditions with excitation current and zero excitation current.

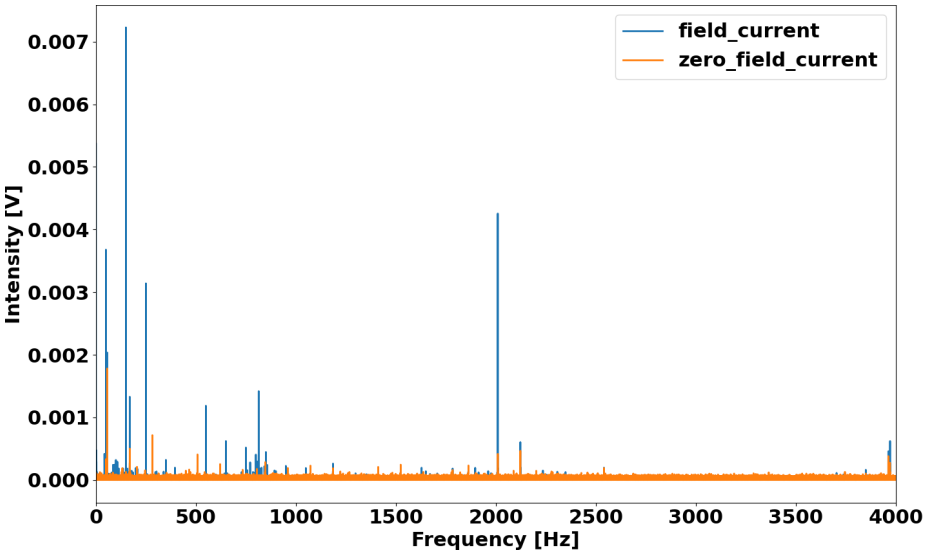

Figure 6.1: Amplitude spectrum shows a comparison between zero and nominal excitation current in no-load within the range 0-4,000 Hz

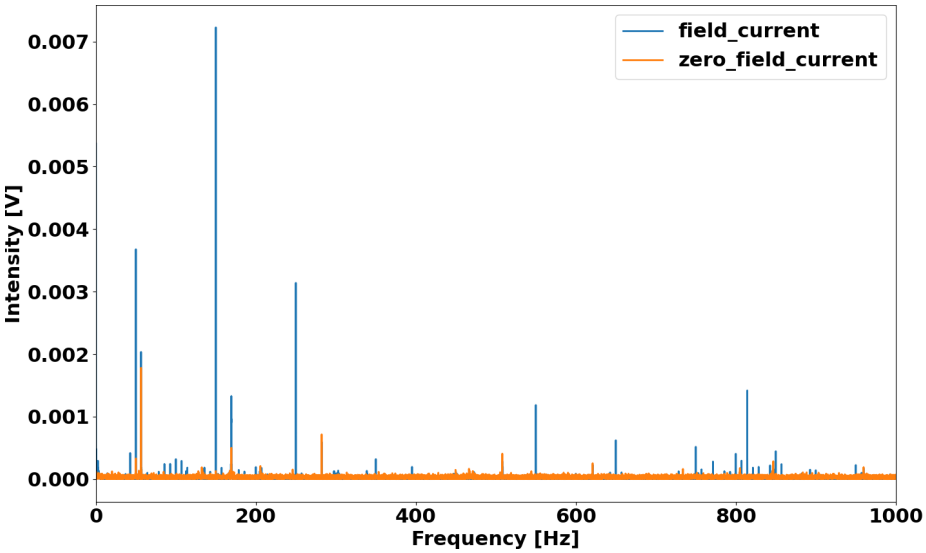

Figure 6.2: Amplitude spectrum shows a comparison between zero and nominal excitation current in no-load within the range 0-1,000 Hz

6.2 Healthy signal

6.2.1 Time series plots

The times series plot of the healthy signal with the generator running in no-load, shows voltage signals that has an amplitude of about 400 mV. This can be seen in the figure below.

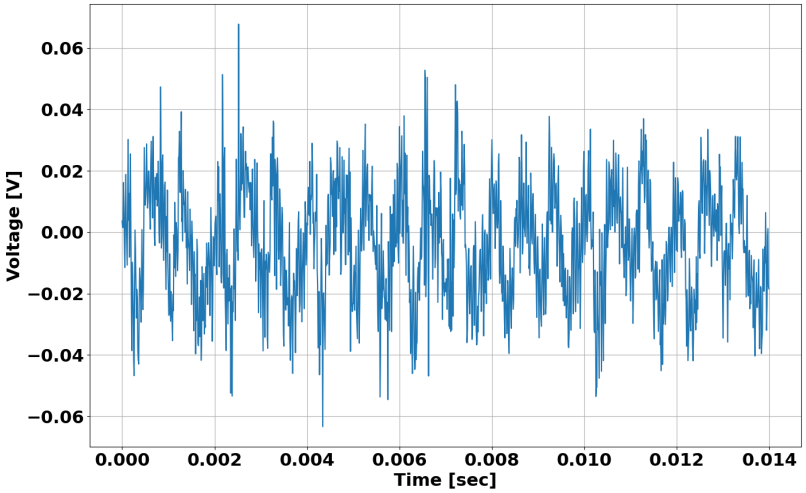

Figure 6.3: Time series plot of the healthy signal in no-load

The simulated signal has amplitude of about 15 mV that is about 3.75% of the measured signal amplitude.

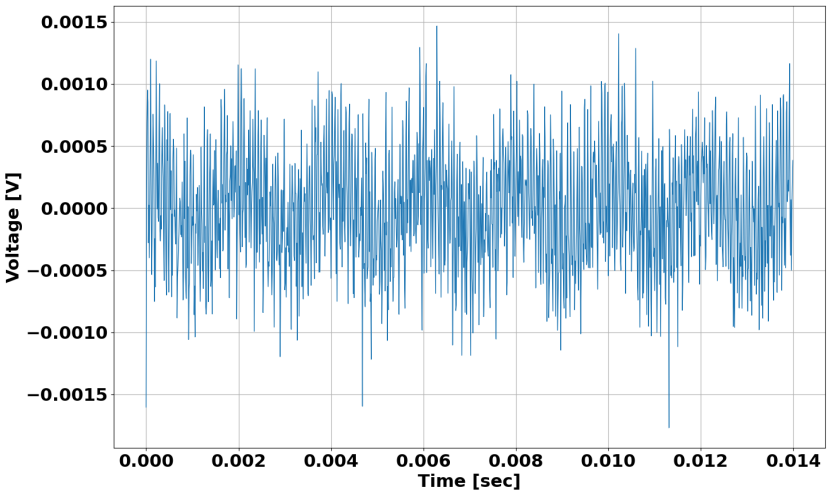

Figure 6.4: Time series plot of the simulated no-load signal

6.2.2 Fourier transform

The amplitude spectrum of the measured healthy signal in no-load shows that the main part of the frequency lies in the range of 0 to 1,000 Hz. The most prominent frequencies are 50 Hz, 150 Hz, 250 Hz, 550 Hz, and 814 Hz.

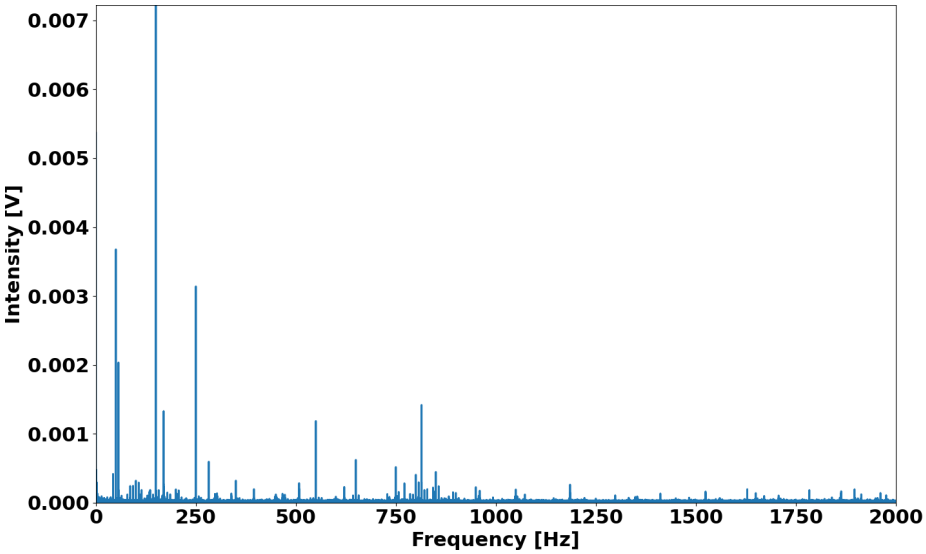

Figure 6.5: Fourier transform of the healthy signal in no-load

The simulated signal does also consist of frequencies 50 Hz, 150 Hz, 250 Hz, 550 Hz, and 814 Hz. However it also consists of higher-order frequencies that are not seen in the lab measurement.

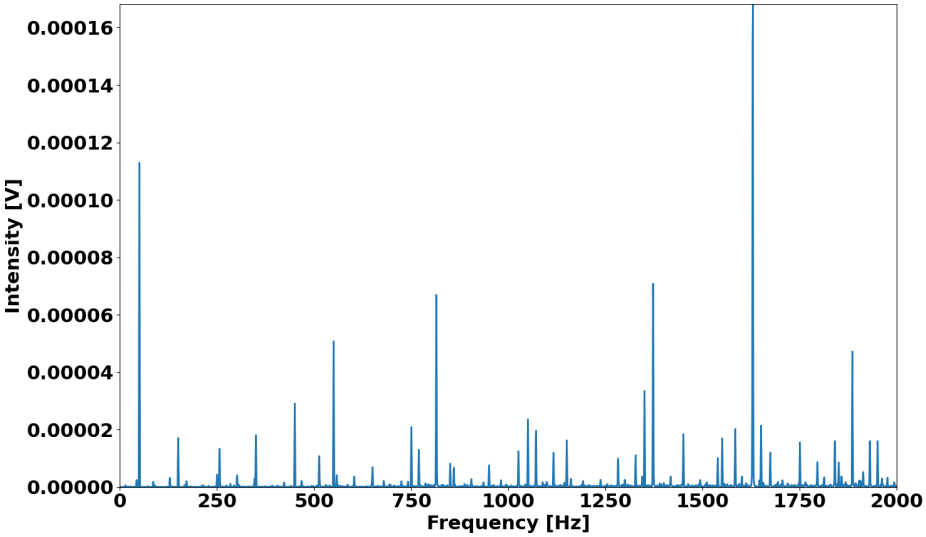

Figure 6.6: Fourier transform of the simulated healthy signal in no-load

6.2.3 Wavelet transform

The wavelet transform of the simulated and measured signal does not show a distinct pattern

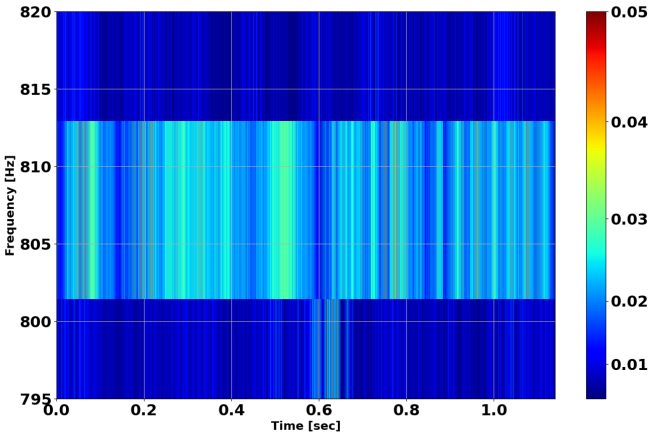

Figure 6.7: Continues wavelet transform of the healthy signal

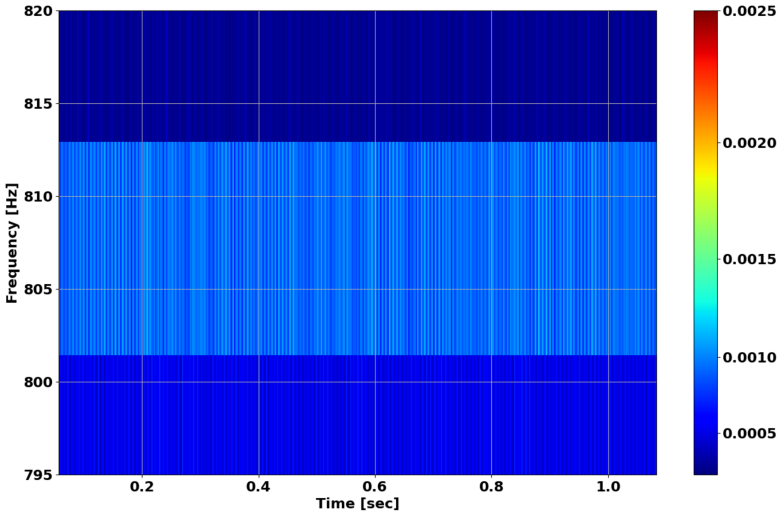

Figure 6.8: Continues wavelet transform of the simulated healthy signal

6.3 Inter-turn short circuit

6.3.1 Time-series plot

By looking at the time-series plots with an increasing number of inter-turn short circuits, it is impossible to distinguish between an increase in fault severity.

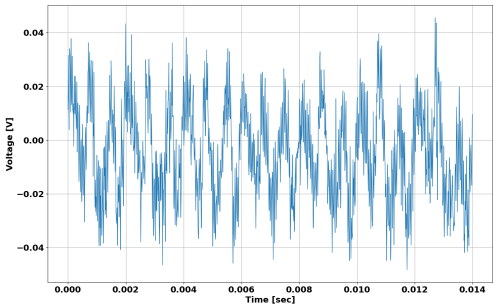

Figure 6.9: Time series plot of the shaft voltage with 1 short-circuited turn

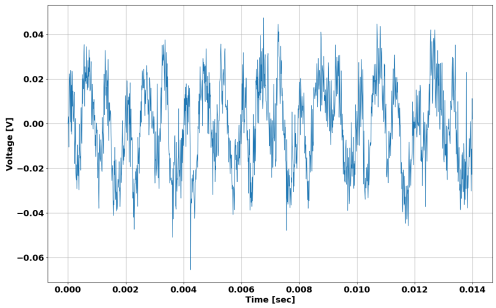

Figure 6.10: Time series plot of the shaft voltage with 2 short-circuited turns

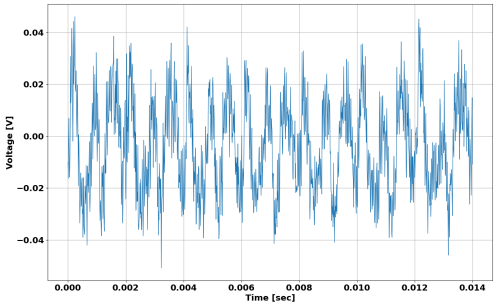

Figure 6.11: Time series plot of the shaft voltage with 3 short-circuited turns

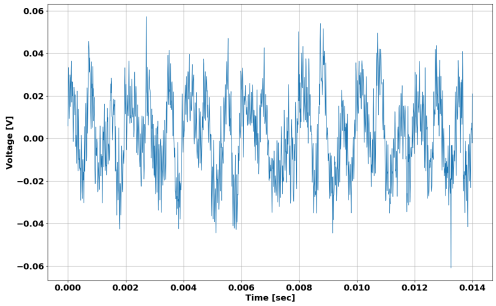

Figure 6.12: Time series plot of the shaft voltage with 7 short-circuited turns

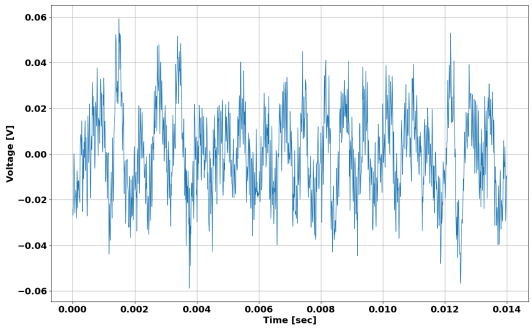

Figure 6.13: Time series plot of the shaft voltage with 10 short-circuited turns

The simulated shaft voltage on the other hand, shows an increased amplitude with the number of inter-turn short circuits.

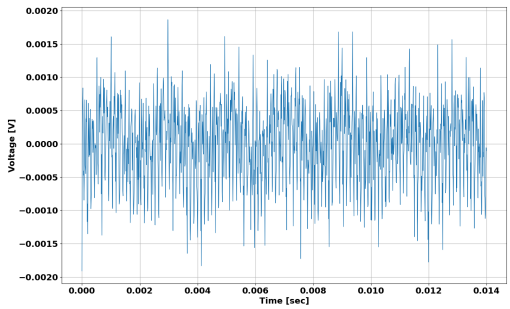

Figure 6.14: Time series plot of the simulated shaft voltage with 1 short-circuited turn

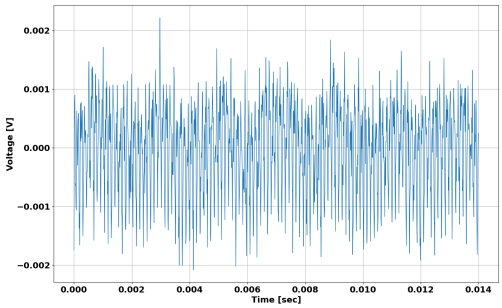

Figure 6.15: Time series plot of the simulated shaft voltage with 2 short-circuited turns

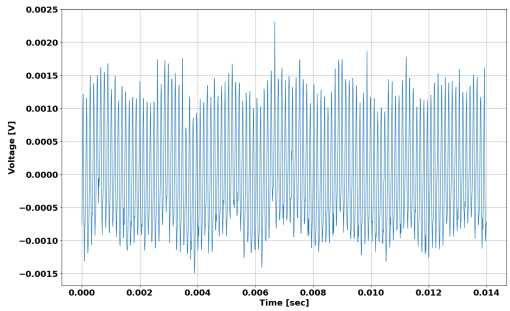

Figure 6.16: Time series plot of the simulated shaft voltage with 3 short-circuited turns

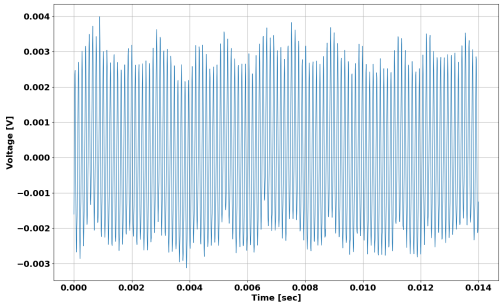

Figure 6.17: Time series plot of the simulated shaft voltage with 7 short-circuited turns

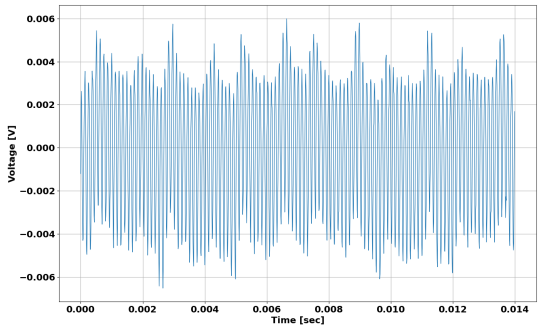

Figure 6.18: Time series plot of the simulated shaft voltage with 10 short-circuited turns

6.3.2 Fourier transform

The amplitude spectrum compares the shaft voltage with an increasing number of short circuited coils. The short circuites changes the amplitude of frequencies around 800 Hz and

0 to 300 Hz.

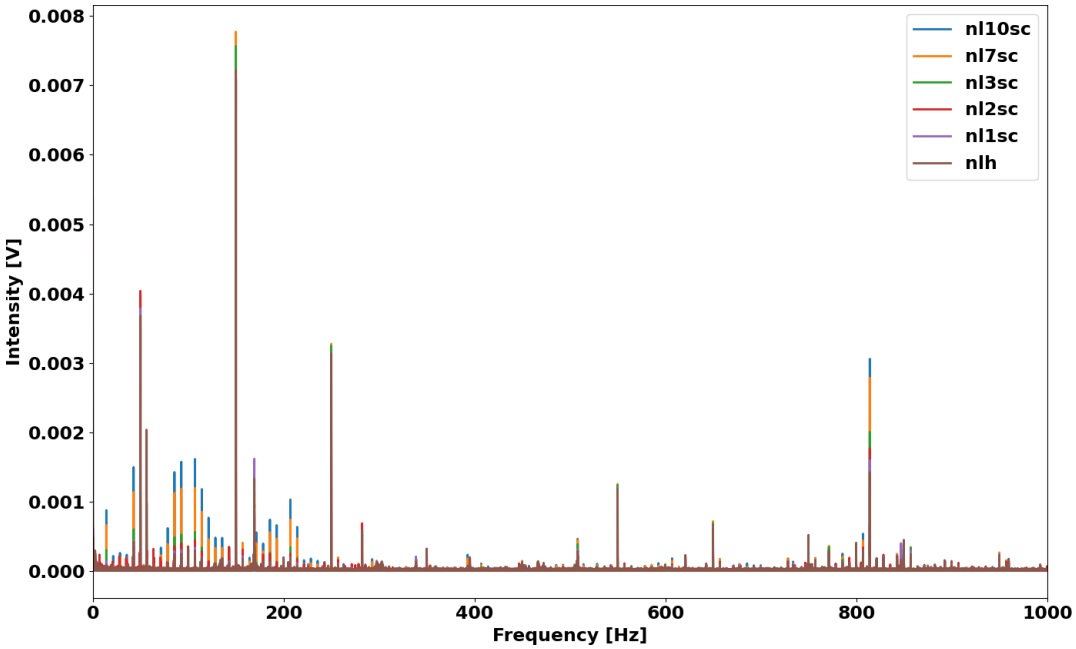

Figure 6.19: Amplitude spectrum that compares the 0, 1, 2, 3, 7, 10 ITSC when running the machine with no load

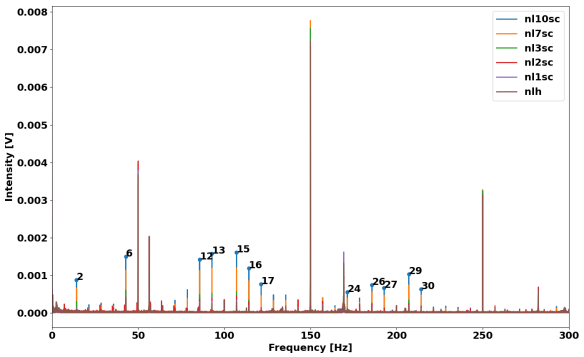

Figure 6.20: Amplitude spectrum comparing number of SC coils at no load in the range 0-300 Hz

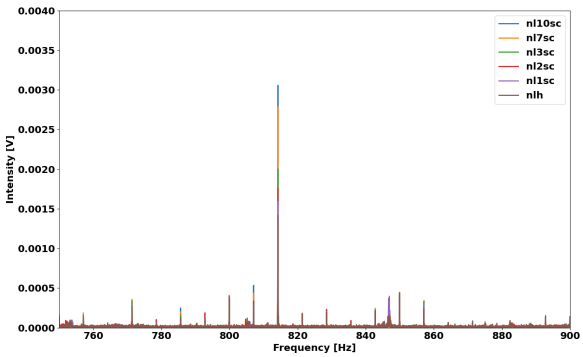

Figure 6.21: Amplitude spectrum comparing number of SC coils SC at no load around 800 Hz

Fig 6.20 shows that the change in amplitude happens at harmonics of the mechanical frequency of the machine, which is 7.14 Hz. The number indicating the frequencies with the most significant change in amplitude, given an increasing number of ITSC, is multiples of the mechanical frequency. However, the most significant change in amplitude happens at 814 Hz, which is the slotting frequency of the machine, this is seen in fig 6.21.

The amplitude spectrum of the simulated signal shows the most significant changes happen in the range 0-300 Hz and around 800 Hz, which is similar to the measured results.

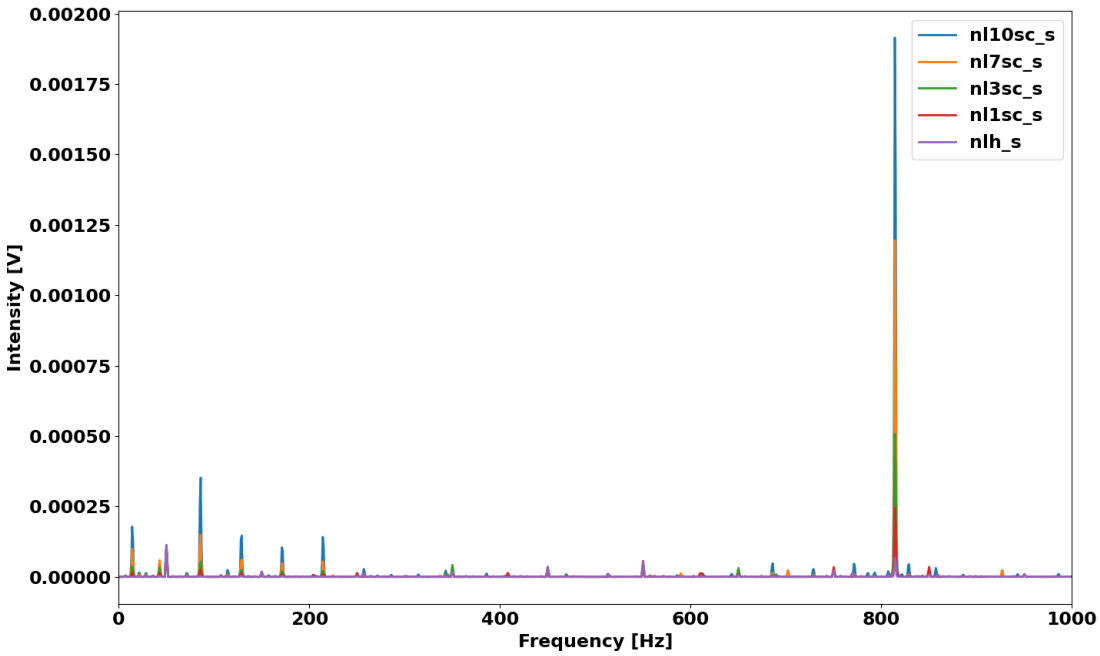

Figure 6.22: Amplitude spectrum that compares the 0, 1, 2, 3, 7, 10 ITSC when simulating the machine with no load

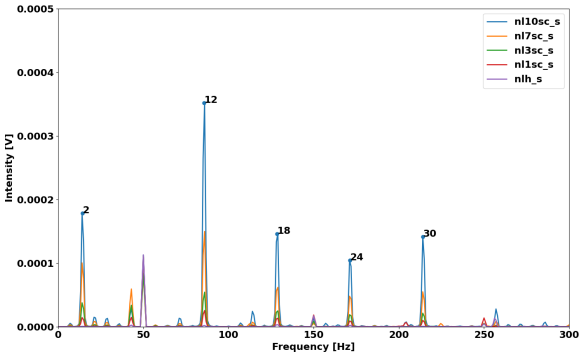

Figure 6.23: Amplitude spectrum comparing number effect of SC coils when simulating no load in the range 0-300 Hz

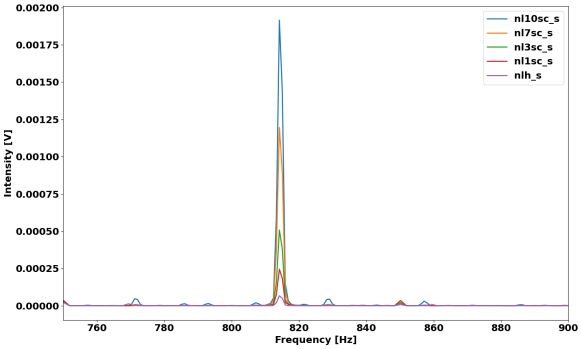

Figure 6.24: Amplitude spectrum comparing number effect of SC coils when simulating no load around 800 Hz

6.3.3 Continuous wavelet transform

CWT for the measured signal shows a clear pattern that corresponds with the mechanical rotation of the machine. The black box represents one mechanical rotation.

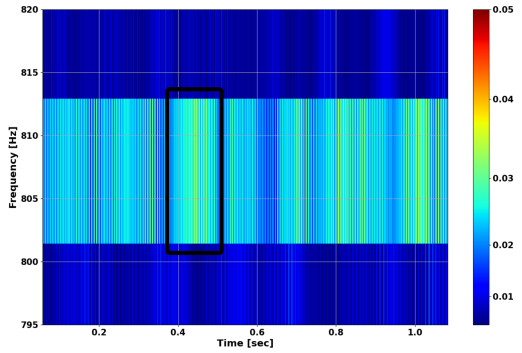

Figure 6.25: CWT plot of the shaft voltage with 1 short-circuited turns around 800 Hz

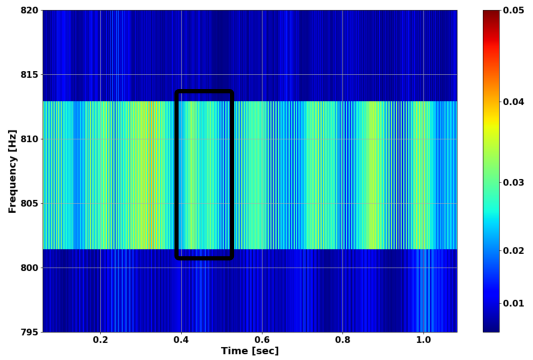

Figure 6.26: CWT plot of the shaft voltage with 2 short-circuited turns around 800 Hz

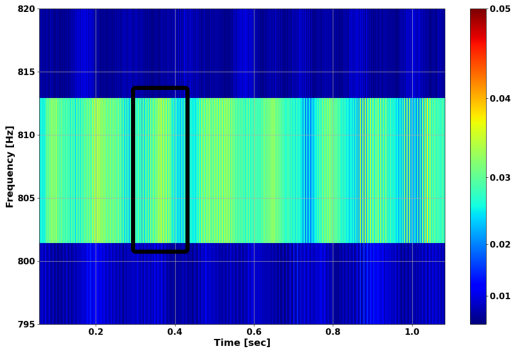

Figure 6.27: CWT plot of the shaft voltage with 3 short-circuited turns around 800 Hz

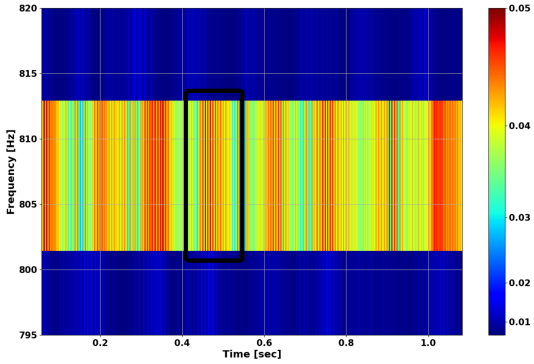

Figure 6.28: CWT plot of the shaft voltage with 7 short-circuited turns around 800 Hz

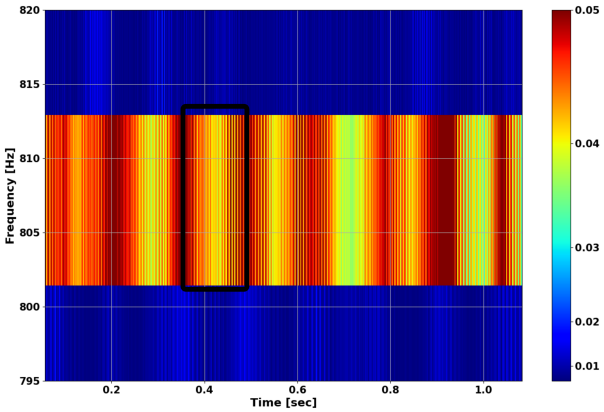

Figure 6.29: CWT plot of the shaft voltage with 10 short-circuited turns around 800 Hz

CWT of the simulated shaft voltage follows:

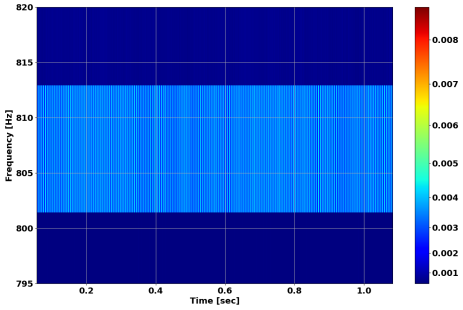

Figure 6.30: CWT plot of the simulated shaft voltage with 1 short-circuited turns around 800 Hz

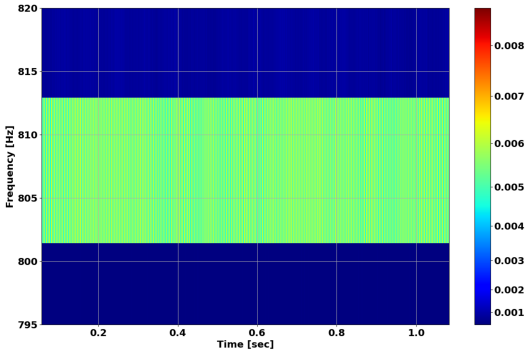

Figure 6.31: CWT plot of the simulated shaft voltage with 2 short-circuited turns around 800 Hz

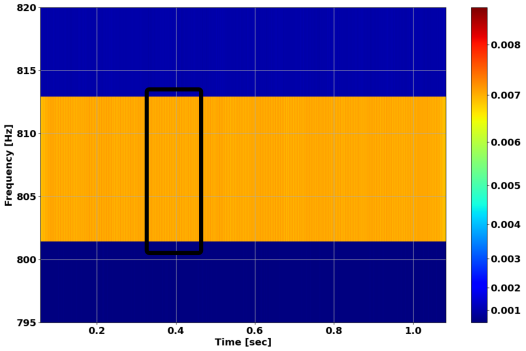

Figure 6.32: CWT plot of the simulated shaft voltage with 3 short-circuited turns around 800 Hz

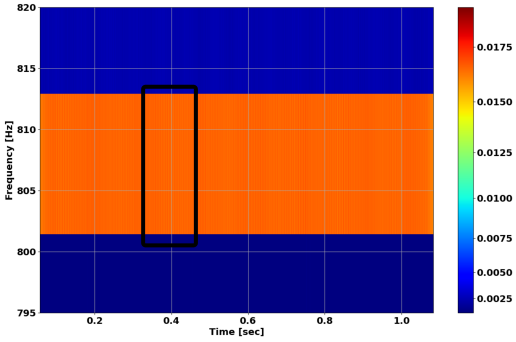

Figure 6.33: CWT plot of the simulated shaft voltage with 7 short-circuited turns around 800 Hz

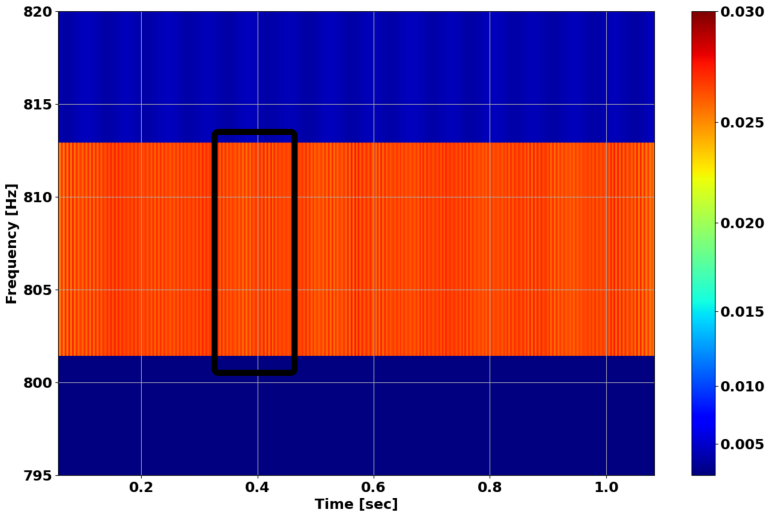

Figure 6.34: CWT plot of the simulated shaft voltage with 10 short-circuited turns around 800 Hz

The simulated results do not have a clear pattern seen in the measured results. In the case of 1 ITSC and 2 ITSC was the black box skipped due to no pattern observed.

6.3.4 Load variation

To investigate how the signal changes with load are the amplitude of frequencies numbered in fig 6.20 and the slotting frequency plotted for all the loads compared. The blue line in each plot represents the average of the amplitude at each level of short- circuits.

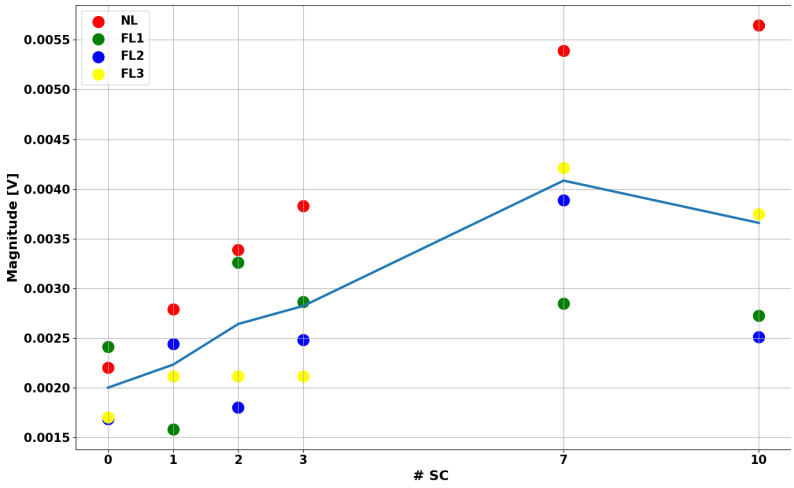

Figure 6.35: The magnitude of 814 Hz plotted as a function of SC and load

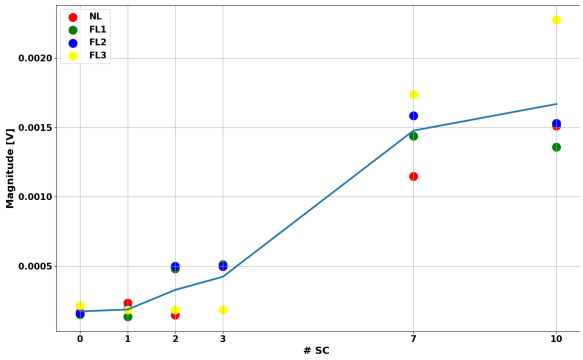

Figure 6.36: The magnitude of the 2 overtone plotted as a function of SC and load

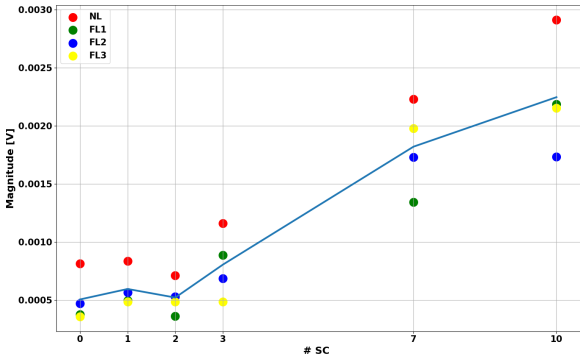

Figure 6.37: The magnitude of the 6 overtone plotted as a function of SC and load

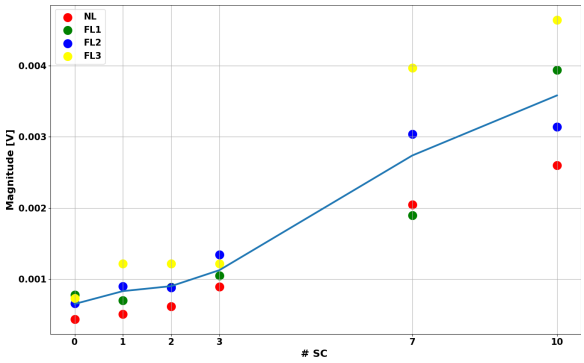

Figure 6.38: The magnitude of the 12 overtone plotted as a function of SC and load

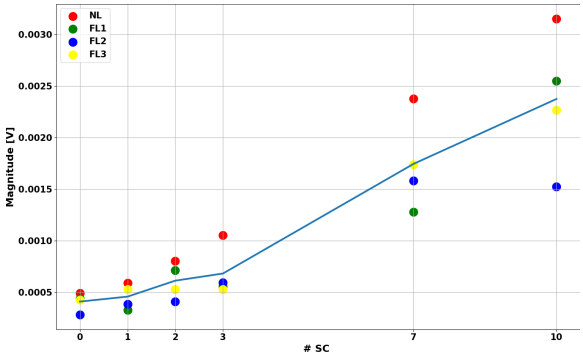

Figure 6.39: The magnitude of the 13 overtone plotted as a function of SC and load

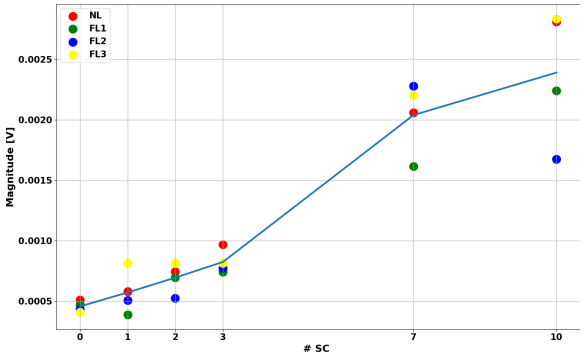

Figure 6.40: The magnitude of the 15 overtone plotted as a function of SC and load

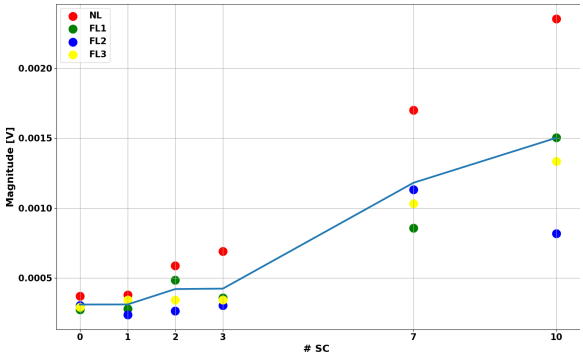

Figure 6.41: The magnitude of the 16 overtone plotted as a function of SC and load

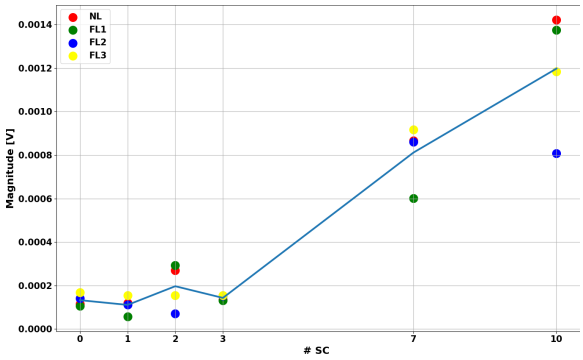

Figure 6.42: The magnitude of the 17 overtone plotted as a function of SC and load

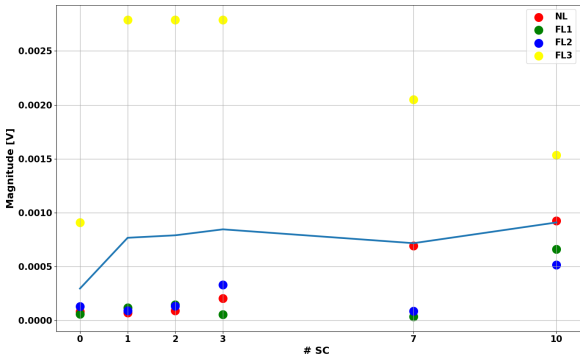

Figure 6.43: The magnitude of the 24 overtone plotted as a function of SC and load

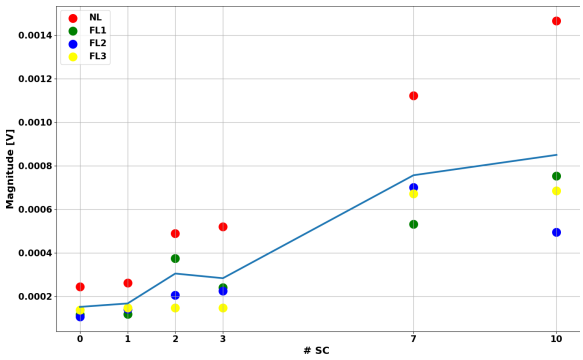

Figure 6.44: The magnitude of the 26 overtone plotted as a function of SC and load

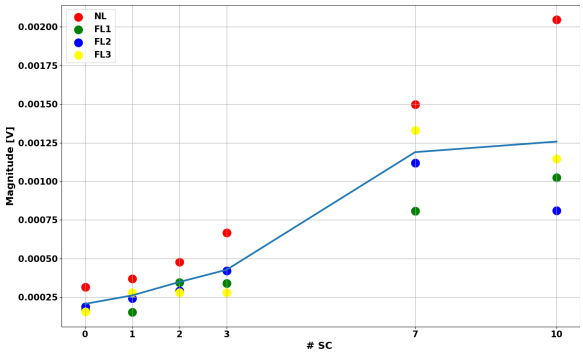

Figure 6.45: The magnitude of the 29 overtone plotted as a function of SC and load

Simulation

To investigate how the simulated signal changes with load are the amplitude of frequencies numbered in fig 6.23 and the slotting frequency plotted for no-load and R2L as described in 4.4

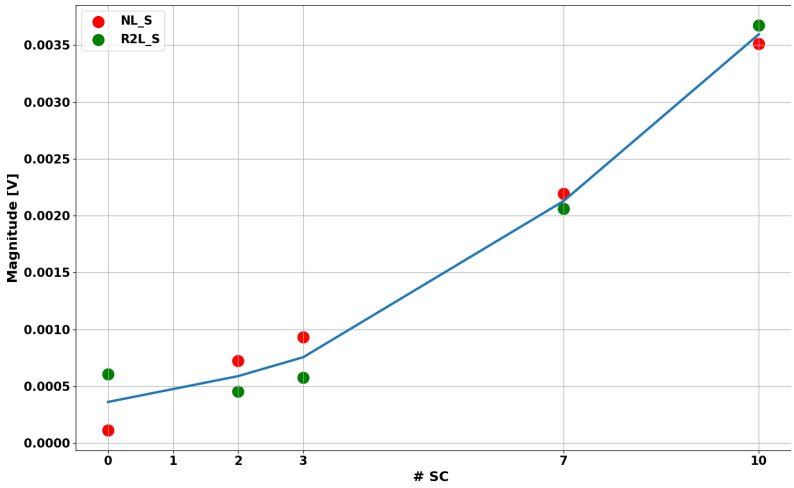

Figure 6.46: The magnitude of the simulated 814 Hz plotted as a function of SC and load

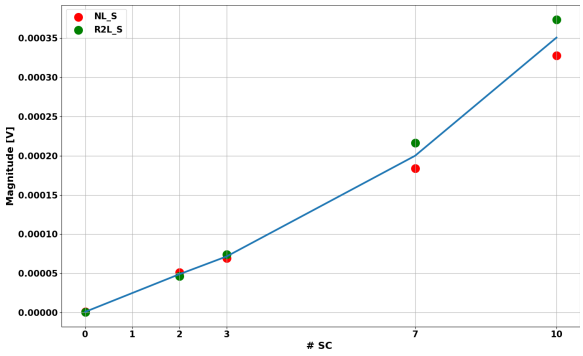

Figure 6.47: The magnitude of the simulated 2 overtone plotted as a function of SC and load

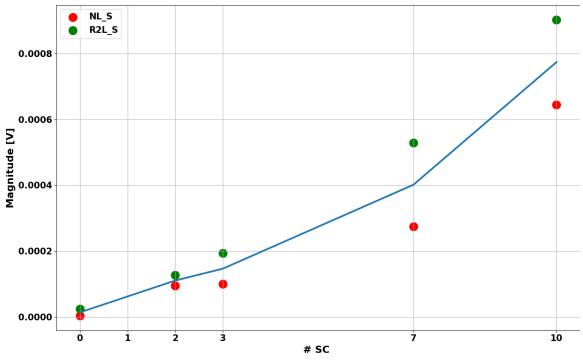

Figure 6.48: The magnitude of the simulated 12 overtone plotted as a function of SC and load

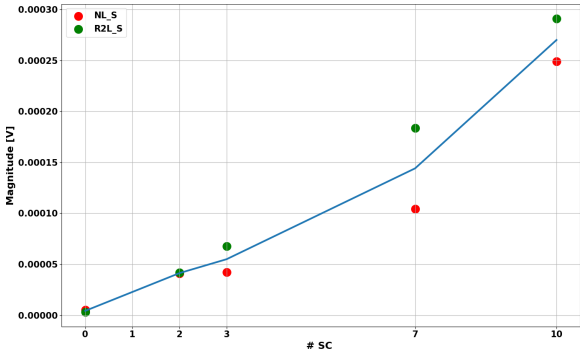

Figure 6.49: The magnitude of the simulated 18 overtone plotted as a function of SC and load

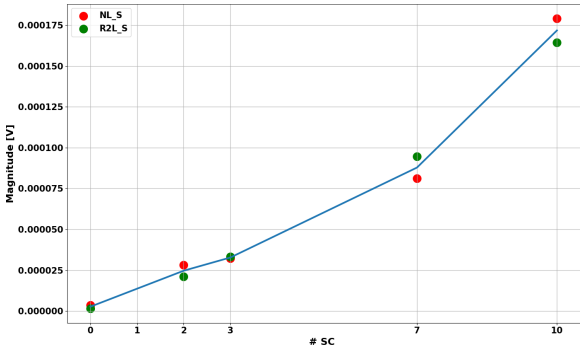

Figure 6.50: The magnitude of simulated the 24 overtone plotted as a function of SC and load

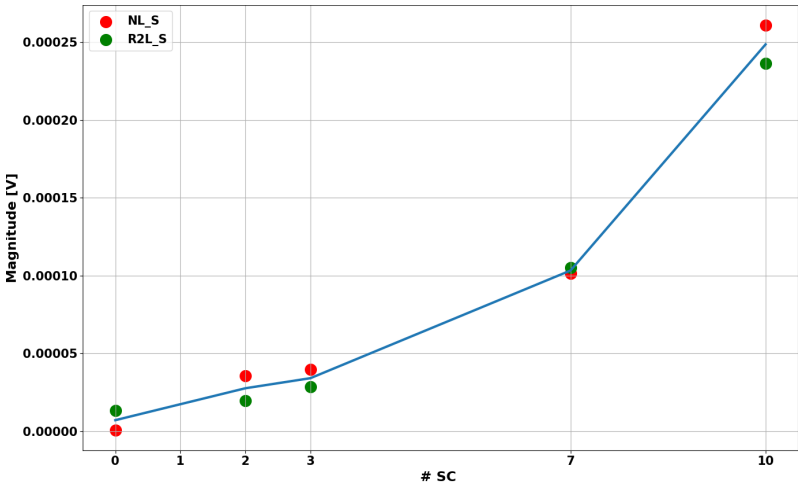

Figure 6.51: The magnitude of simulated the 30 overtone plotted as a function of SC and load

6.4 Static eccentricity

6.4.1 Time series plots

The signal of 10 and 20 percent eccentricity is not distinguishable by plotting the time series plot, this can be seen on the figures below.

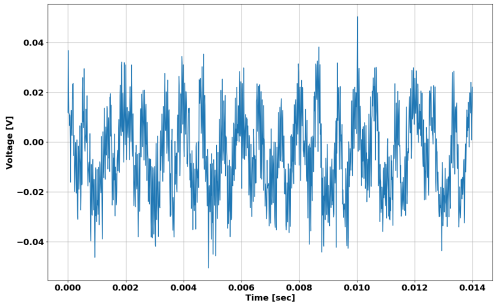

Figure 6.52: Time series plot of the shaft voltage with 10% static eccentricity

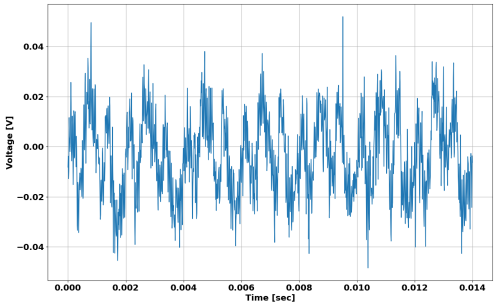

Figure 6.53: Time series plot of the shaft voltage with 20% static eccentricity

The time series plot of the simulated signal shows that the single increases with the fault severity.

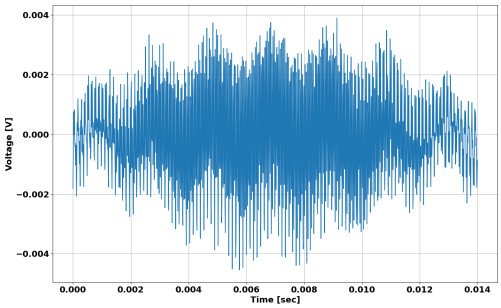

Figure 6.54: Time series plot of the simulated shaft voltage with 10% static eccentricity

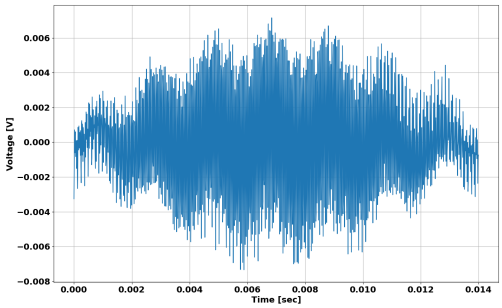

Figure 6.55: Time series plot of the simulated shaft voltage with 20 % static eccentricity

6.4.2 Fourier transform

Fourier transform of the signal shows that the 1st, 2nd, 3rd and 4th harmonic of the slotting in frequency is present and that those frequencies increases with the amount of static eccentricity.

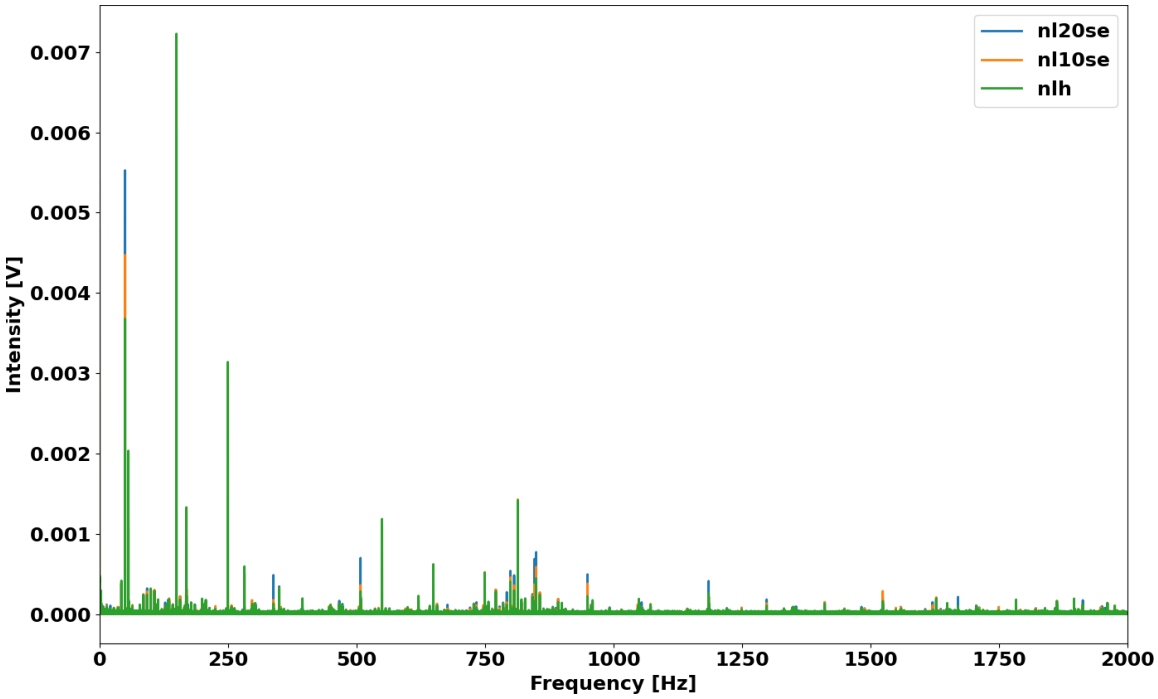

Figure 6.56: Fourier transform of the ITSC shaft signals in the frequency range 0-300 Hz

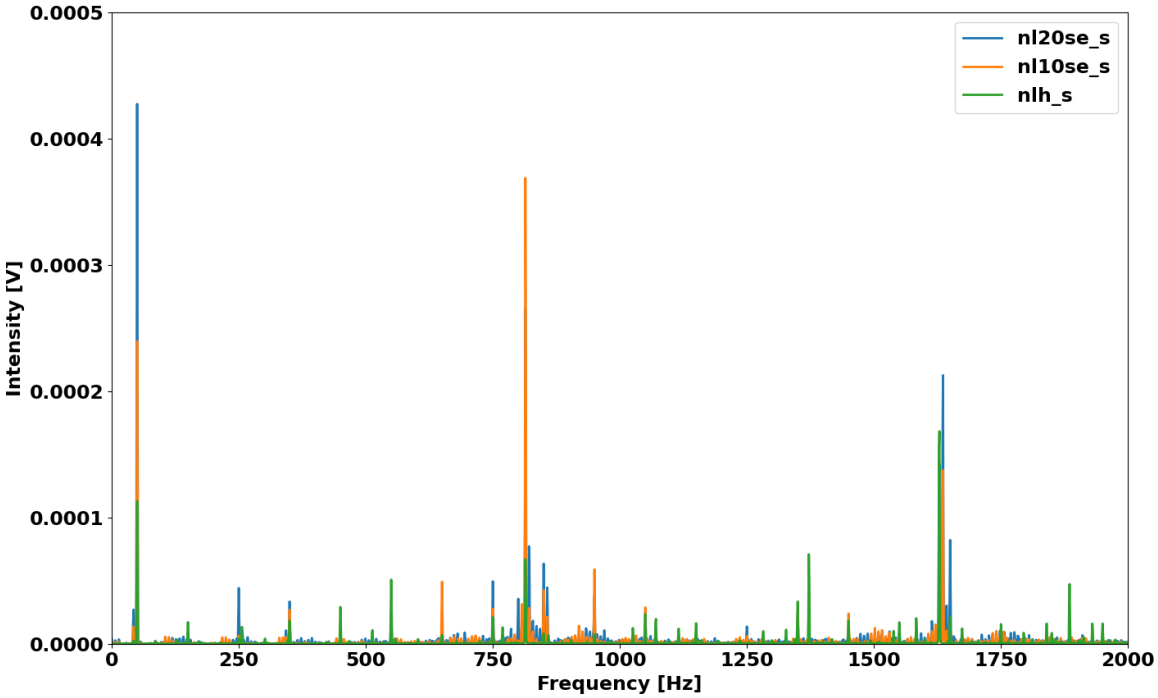

Figure 6.57: Fourier transform of the ITSC shaft signals in the frequency range 0-300 Hz

Simulation The figure above shows that the odd harmonics; 1st, 5th, 7th, 13th and 15th harmonics of 50 Hz is present in the signals.

6.4.3 Wavelet transform

Wavelet transform of the static eccentricity shaft signal clearly shows that the slotting frequency varies in the same way as with the ITSC. The difference between the simulated and the measured is that the magnitude of the simulated is reduced when the measured is constant.

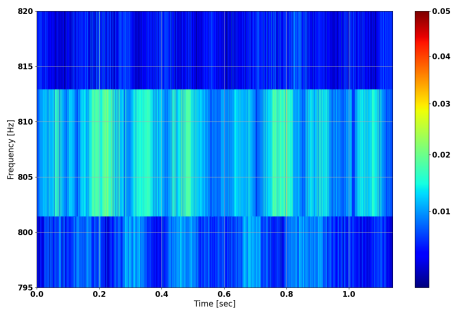

Figure 6.58: Continues wavelet transform of the signal with 10% static eccentricity

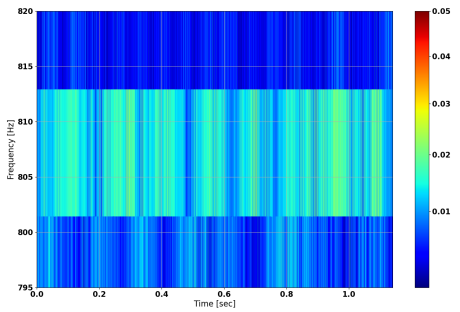

Figure 6.59: Continues wavelet transform of the signal with 20% static eccentricity

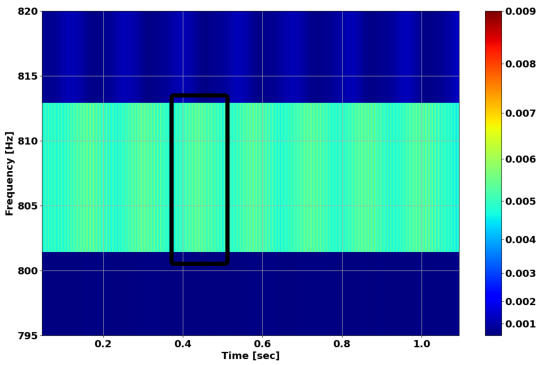

Figure 6.60: Continues wavelet transform of the signal with 10% static eccentricity

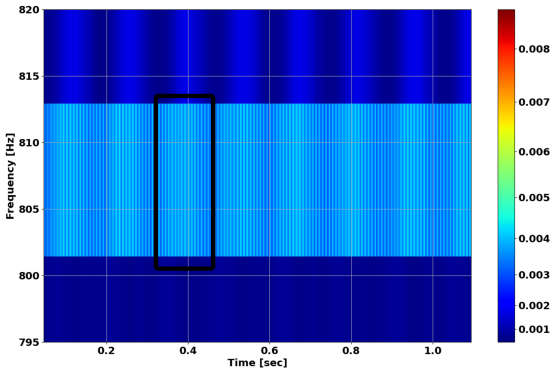

Figure 6.61: Continues wavelet transform of the signal with 20% static eccentricity

6.4.4 Load variation

50 Hz has the most noticeable amplitude change when the static eccentricity changes. Therefore, the frequency is investigated to determine the effect load has on static eccentricity.

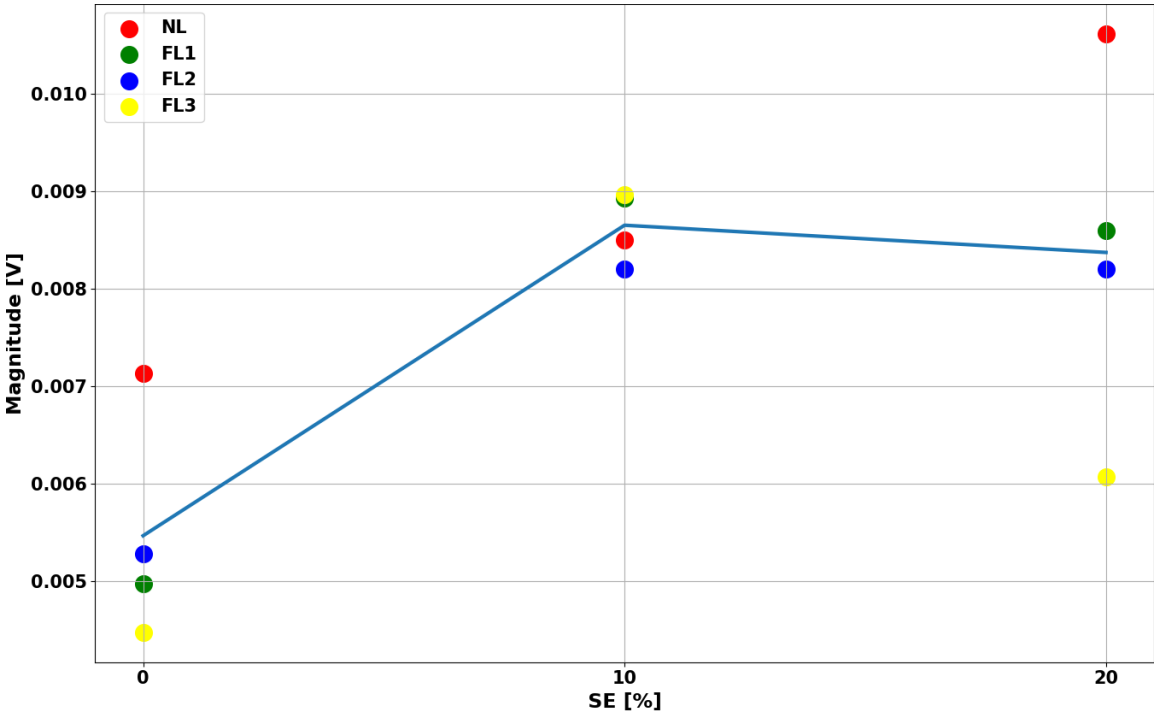

Figure 6.62: The magnitude of 50 Hz plotted as a function of SC and load

Simulation

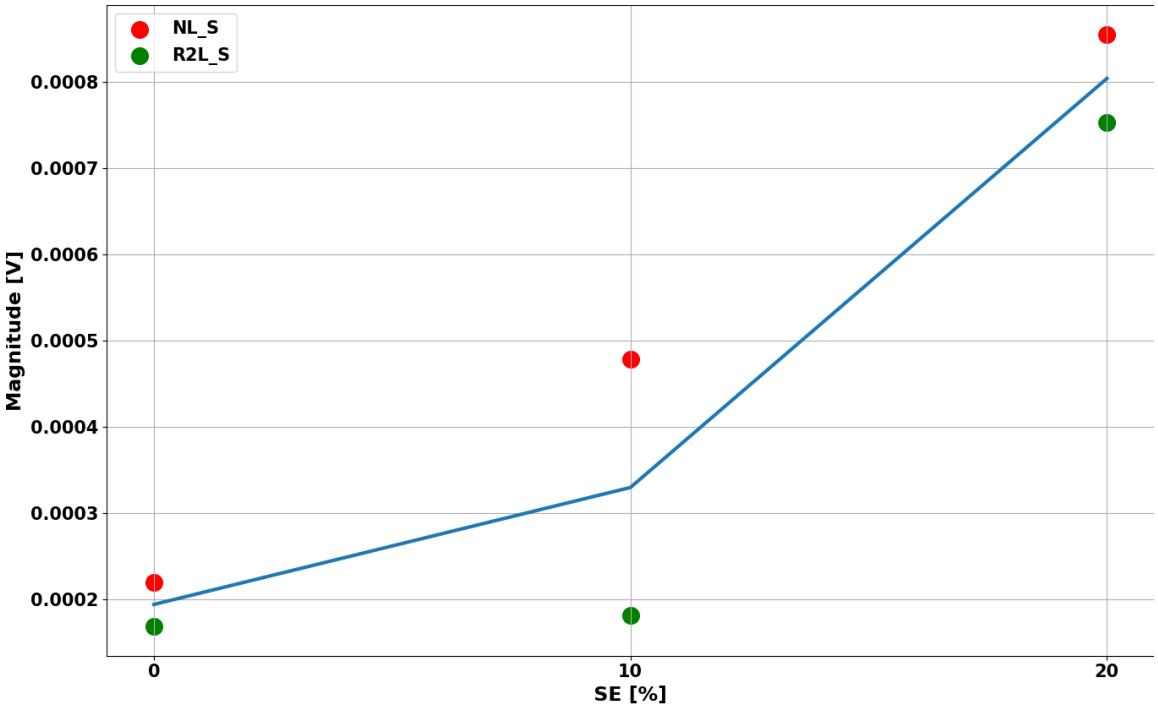

Figure 6.63: The magnitude of the simulated 50 Hz plotted as a function of SC and load

Chapter 7

Discussion

In this chapter each part of the project will be discussed. The first section covers whether it will be possible to simulate the shaft voltage of the given machine with the utilization of finite element modeling. Then the topic of measuring the shaft voltage will be evaluated. This has been a difficult task. The result is divided into two parts, one for the short circuit and the next for the static eccentricity. The central part of the findings are the results of the finite element and the measured voltage. Towards the end of the chapter, there will be a discussion about signal processing and a suggestion for future work.

7.1 Finite element modeling and simulations

The target of the finite element analysis was to simulate the shaft voltage with adequate precision. The finite element analysis was done by taking a verified generator model and extending it with a shaft and generator housing model. As earlier explained, some simplifications and assumptions were made during the extension of the generator model and when the finite element modeling was performed. A variety of different factors can impact the accuracy of the model. The material in the shaft, the housing model, and the number of mesh points are the most critical ones.

The material in the shaft and housing was first set to stainless steel. According to [23, p 54] the shaft and housing material are not affecting the induced voltage in the shaft. Stainless steel has a constant permittivity of 1, and it is faster to simulate than a material with a B-H curve. However, the pattern of the slotting frequency did not correspond with the measured lab results. Therefore, the material in the simulations was changed to the ferromagnetic material steal 1010. The change of material did impact the magnitude of the voltage and the pattern found by utilizing CWT. The magnitude went from volts to millivolts, and the pattern seems to correspond with the lab results. Ideally, the material in the simulation and the actual model should be the same. However, the permittivity and ferromagnetic material are dependent on various factors, and the same material does not

need to have the same permittivity [33]. The difference between ferromagnetic material is not as significant as the difference between stainless steel with a relative permittivity of 1 to that has a relative permittivity of around 2,000.

The number of mesh points in the original model is about 2.5e5. This is approximately the same amount as in the final model. To make this possible, the mesh points in the rotor were reduced. Without this reduction in mesh points, the already long running time of 24 hours would be further extended. The problem with a longer simulation time is that ANSYS runs on a server shared with several users. It uses around 100% of the available resources to be finished in 24 hours. A mesh comparison was made to investigate how much of a difference the decrease in the mesh would make. The full mesh was reduced by 20% by reducing the rotor and shaft points. The reduction did not show any significant alternation of frequencies in the frequency spectrum as seen in 4.7, only a slight change in amplitudes. Therefore, it is likely that the variation of around 20% does not change the shaft voltage.

The model of the housing is based on experimental measurements done with digital calipers. The digital calipers have an accuracy of 0.02 mm. The most significant uncertainty is that the housing is a 3D model and making a 2D model is the same as assuming that the model is homogeneous around the stator. Furthermore, the dimensions of the housing change throughout the model [27], making it almost impossible to create an accurate 2D model of the housing. The housing is also grounded on both ends while the model is grounded on only one end. If the model had been grounded on both ends, would one see zero induced voltage induces in the house.

The generator is connected to the grid when running different types of loads. Because of this, it was proposed to make a grid model in ANSYS to investigate the generator connected to the grid. However, connecting it to a passive load or connecting it to an ideal voltage model is similar. It was more convenient to simulate with a passive load, so it was chosen to do it that way.

7.2 The laboratory generator measurements

To get accurate test results from the laboratory measurements was challenging and time-consuming. The shaft voltage was measured multiple times with slightly different approaches. Despite some improvement in the results, getting consistent results turned out to be complicated. Important factors that impact the results are the method of measuring the shaft voltage, variation in the machine's state, and the placement of the brush holder. Other less prominent factors are noise and temperature.

In the FEM, the shaft voltage is measured as a combination of one part induced in the shaft and a second part in the housing. The equivalent way of measuring this in the lab

would be to measure the voltage across the shaft [23]. This method is challenging to get right due to its complicated setup [23]. The lab setup is supposed to be a scaled version of an actual hydropower station. It would not be easy to mount a second brush sufficiently between the turbine and generator. Due to this it was opted for a more straightforward measurement setup by measuring the voltage across the isolated bearing. This method is similar to how one measures the shaft voltage in a current installation [25]. The problem with this measurement method is that the isolated bearing and the bearing on the other side act as capacitance. The non-isolated bearing acts as capacitance since the liquid forms an isolating film due to a hydrostatic effect when running the machine above 100 rpm [34]. The effect of capacitances and other inductances is that they most likely create a low-pass filter. Based on the magnitude of the Fourier transform, the response is most likely a type of low-pass filter. This will dampen the high frequencies.

One way to make the simulations correspond with the lab measurements would be to estimate the impedances imposed by the bearing and external factors. The problem will then be to estimate or measure the values of the impedances and construct an equivalent circuit. An equivalent circuit is shown in fig B.1. Estimating the capacitance of the isolated bearing is straightforward [1]. The other capacitances are also possible to estimate [34], but this has not been done in this project. It would potentially make the FEM more accurate, but its effect is dampening the high-frequency components that are not used to assess the machine condition, except the slotting frequency. That seems to have an amplitude that is too high compared to the measured results.

The way the voltage was measured did have a significant impact on the quality of the signal. It was found that the best way to measure the voltage across the bearing was to measure at the shaft with a silver graphite brush and ground the probe to the shaft. Silver graphite brushes have high conductivity. The conductivity also remains relatively constant even with an increase in temperature. This makes silver graphite brushes suitable to measure shaft voltage. However, when mounting, it is hard to get the whole brush in contact with the shaft. The brush is prone to change position because of the improvised solution consisting of a magnet to keep the rack in place. When inspecting the brush after the last measurement, it only showed wear on half of its contact area. Ideally, the whole brush should be in contact with the shaft. A solution to this problem could be to construct a permanent brush holder that ensures complete contact between the shaft and the surface of the brush.

Noise pollution in the lab environment could affect the measured signal [35]. To investigate this effect, the signal was measured with zero excitation current. Then was the Fourier transform compared with the no-load healthy condition. This is seen in fig 6.2 It can be seen that the noise does not significantly impact the frequencies used to address

[1] Analytical formula of parallel plate capacitor $C\frac{\epsilon A}{d}$

the machine's health. When the excitation current is turned off, it is clear that it induces voltage around 2,000 Hz, this is above the frequencies of interest.

7.3 Fault detection using Shaft signals

7.3.1 Inter-turn short-circuit (ITSC)

Based on the simulated results, it was easy to distinguish between the different ITSC cases. The amplitude of the time series plot increases with the number of short-circuit faults. The same characteristic is not possible to see based on the measured results.

Fourier transform of the signal reveals that the most significant change happens at the slotting frequency, 814 Hz. An increase in this frequency is seen both in the simulation and in the laboratory measurements. This is in line with previous work on the field [10]. The difference is that the simulation has a more significant increase, making it easier to distinguish between the cases. Because the measured signal has a lower change, especially from healthy to 1, 2, 3 turn short-circuit, it could be hard to detect a ITSC fault in a real-world application.

When the number of short circuits is above two turns, harmonics of the mechanical frequency are observed. However, the simulation only predicts five harmonics—namely, 2nd, 12th, 18th, 24th, and 30th. These frequencies are also seen in the amplitude spectrum of the laboratory generator, but there are also many more harmonics of the mechanical frequency. Why the simulation is not predicting all the harmonics is hard to explain, but it might be a combination of the housing being a 3D object that is not easy to model in 2D, the material of the shaft, and the number of mesh points. In appendix D is the amplitude spectrum of the induced voltage in the shaft and housing plotted. It shows that most of the shaft voltage lower-order components are induced in the housing. With a more accurate model of the housing, it could probably be possible to predict more of the low-frequency component.

Another way to predict the frequencies affected by an increase in short-circuited coils is by analytical formulas. Using formula 2.3 it is predicted that one sees a specific harmonic component at around the 18th mechanical order. That is the case for both simulations and measurements results.

The continuous wavelet transform was focused on the slotting frequency to investigate whether the pattern of the project work was visible in the lab measurements. It did not reveal the same pattern as seen in the project work C. This is most likely due to the fact that stainless steel was used in the project work simulations. With the new steel, steel 1010, a comparable pattern like the one in the lab measurement is observed. The difference is that there is a more significant magnitude difference in the simulation than in the lab measurement.

7.3.2 Static eccentricity (SE)

The time-series plot of the simulated data indicate that the severity of the SE is linked with the magnitude of the signal. This was not the fact for the result measured in the lab.

Fourier transform of the simulated and the measured shaft signal reveals a magnitude increase in the 50 Hz frequency. This frequency increases with the amount of SE severity. The result is in line with previous work [2], which states that odd harmonics of the electrical frequency increases with the degree of SE.

Continues wavelet transform (CWT) around the slotting frequency did not reveal any pattern that could be used to assess the machine's health state.

7.4 Load variation and measurement variability

The shaft voltage is dependent on the load. This can be seen in section 6.3.4, where the magnitude of different frequencies changes when the machine is loaded. Based on the measurements, there is no clear pattern showing that the loads steadily increase with the severity. Because of this, a scheme based on the correspondence between a loaded condition and the shaft voltage is not the best method. A solution is to use the machine running in no-load. On most of the frequencies of interest, it is seen that the no-load voltage has a steady increase in voltage with an increasing fault. Another method could be to look at the variation of shaft voltage since the variation of the shaft voltage increases with the severity.

As already mentioned previously in the discussion, the measurement set-up is not ideal with an improvised installation. This could result in a change of contact area of the brush. To investigate this, the voltage drop was measured with an ohmmeter between each fault. It shows values between 0.97 and $47m$, which is a big difference. To see if the measurement was constant through time, the no-load healthy case was measured before and after all the other measurements. The amplitude spectrogram can be seen in appendix E. The first and last measurements differ in amplitude in two frequencies of interest, namely the 50 Hz and 814 Hz. Comparing the amplitude spectrum E of the last measured signal with 1 ITSC, which has a higher magnitude, due to this it was not possible to detect 1 ITSC.

7.5 Signal sampling and processing

Fourier transforms and CWT were chosen to process the signals. Fourier transform is a fast and easy method to use and is often utilized in online condition monitoring. CWT, on the other hand, is not as straightforward to use. Choosing the suitable mother wavelet is a tedious process, and scaling the color bar to make changes in the time-frequency spectrum clear. As seen in the section 2.5.4, it has its place in online condition monitoring, but it seems that it works best with transient phenomena or when one expects abrupt changes in

the signal.

7.6 Final remarks

The work has shown that it is possible to distinguish between the ITSC and SE faults and their severities. Unfortunately, it was not easy to distinguish between minor and severe cases, and it was needed to use the expensive Rohde & Schwarz oscilloscope to see the individual frequency components. However, an ordinary hydropower generator is bigger than the generator used in the lab measurements. This means that the shaft voltage amplitude is higher. A higher shaft voltage amplitude leads to a greater difference between noise and signal since the signal to noise ratio is increased. Indicating that the fault detection becomes easier compared with the synchronous generator in the laboratory. However, sensor installation and its measurement in a synchronous generator of a hydropower plant is challenging compared with the laboratory measurement.

7.7 Suggestions of further work

Future work in the field of measuring the shaft voltage could for instance be to:

- Create a new model that includes the capacitance of the isolated bearing and the non-isolated bearing.
- Measure the shaft voltage by utilizing two silver graphite brushes on both sides of the machine and differential probes.
- Utilize the Egstone to see what impact harmonics in the stator current exhibits on the shaft voltage and simulate it by having a 3-phase, unbalanced load.
- Perform the shaft voltage measurement and finite element analysis in a real hydropower machine.

Chapter 8

Conclusion

In this thesis it has been investigated how inter-turn short circuit and static eccentricity can be detected by measuring the shaft voltage of a scaled model of a hydropower generator.

The analysis that is presented has first been simulated with the utilization of Finite element modeling and experimental tests performed on a 100 kVA synchronous laboratory generator.

The proposed method is to measure the shaft voltage and then analyze its frequency spectrum as well as its time-frequency spectrum. First fast Fourier transform is used to investigate whether some frequency components that are linked with inter-turn short circuits and whether others are linked with static eccentricity. Then, continuous wavelet transform is used to investigate if a time-dependent frequency pattern in the induced voltage could be used to assess faults and the severity of them.

The simulation results indicated specific harmonics in the shaft signal related to the inter-turn short circuit and static eccentricity. Inter-turn short circuit result in an increased amplitude of the slotting frequency and overtones of the mechanical frequency. The static eccentricity did increase the amplitude of the electrical frequency. However, it was not found any specific time-frequency pattern that made it worthwhile to utilize continuous wavelet transform.

The shaft voltage was measured by attaching a silver graphite brush to the 100 kVA laboratory generator rotor shaft. The measurements showed that it is possible to detect inter-turn short-circuits and static eccentricity in the laboratory generator.

Comparison of the simulations to the measured shaft voltage indicates that the simulations predicts most of the frequencies used to address the machine health. It does however fall short of predicting all of the mechanical frequency overtones. The simulation seems to overestimate the magnitude of higher frequencies such as the slotting frequency. The insuf-

ficient prediction of the mechanical frequencies is believed to do with the complex geometry of the generator housing, which is not accounted for in a 2D simulation. On the other hand, the high-frequency components are dampened due to the capacitances in the measurement loop making it a low-pass filter.

The amplitude of frequencies of interest depends on the loading of the machine. However, two key observations where found: When running the machine in no load, one sees an apparent increase in the amplitude of critical frequencies with the severity of the fault, and when the severity is significant, a large variability in the amplitude of critical frequencies are seen.

In conclusion, measuring the shaft voltage can extract information regarding the operation condition of the generator. To obtain quality measurements it is recommended to use a silver brush that is mounted directly and then grounded below the isolated bearing on the shaft and then grounded below the isolated bearing.

Bibliography

[1] S. sentralbyraa. (2021) Electricity. [Online]. Available: https://www.tek.com/blog/sample-processing-digital-oscilloscope

[2] T. Plazenet, T. Boileau, C. Caironi, and B. Nahid-Mobarakeh, "A comprehensive study on shaft voltages and bearing currents in rotating machines," *IEEE Transactions on Industry Applications*, vol. 54, no. 4, pp. 3749–3759, 2018.

[3] J. S. Hsu and J. Stein, "Shaft signals of salient-pole synchronous machines for eccentricity and shorted-field-coil detections," *IEEE Transactions on Energy Conversion*, vol. 9, no. 3, pp. 572–578, 1994.

[4] H. Ehya, G. Lyng Rødal, A. Nysveen, and R. Nilssen, "Condition monitoring of wound field synchronous generator under inter-turn short circuit fault utilizing vibration signal," in *2020 23rd International Conference on Electrical Machines and Systems (ICEMS)*, 2020, pp. 177–182.

[5] Y. Zhou, X. Bao, C. Di, and L. Wang, "Analysis of dynamic unbalanced magnetic pull in induction motor with dynamic eccentricity during starting period," *IEEE Transactions on Magnetics*, vol. 52, no. 7, pp. 1–4, 2016.

[6] I. Sadeghi, H. Ehya, J. Faiz, and A. A. S. Akmal, "Online condition monitoring of large synchronous generator under short circuit fault—a review," in *2018 IEEE international conference on industrial technology (ICIT)*. IEEE, 2018, pp. 1843–1848.

[7] I. Groth, "On-line magnetic flux monitoring and incipient fault detection in hydropower generators," *Master thesis*, 2019.

[8] P. L. Alger and H. W. Samson, "Shaft currents in electric machines," *Journal of the American Institute of Electrical Engineers*, vol. 42, no. 12, pp. 1325–1334, 1923.

[9] M. Costello, "Shaft voltages and rotating machinery," *IEEE Transactions on Industry Applications*, vol. 29, no. 2, pp. 419–426, 1993.

[10] J. . Torlay, C. Corenwinder, A. Audoli, J. Herigault, and A. Foggia, "Analysis of shaft

voltages in large synchronous generators," in *IEEE International Electric Machines and Drives Conference. IEMDC'99. Proceedings (Cat. No.99EX272)*, 1999, pp. 607–609.

[11] A. Chen, R. Nilssen, and A. Nysveen, "Harmonic analysis and comparison of the back emfs of four permanent magnet machine with different winding arrangements," in *2008 International Conference on Electrical Machines and Systems*, 2008, pp. 3043–3048.

[12] J. G. Proakis and D. K. Manolakis, *Digital Signal Processing (4th Edition)*, 4th ed. Prentice Hall, 2006.

[13] b. Wolke, "Sample processing in a digital oscilloscope," Jul 2013. [Online]. Available: https://www.tek.com/blog/sample-processing-digital-oscilloscope

[14] E. Kreyszig, "Advanced engineering mathematics," 2011.

[15] M. Riera-Guasp, J. Pons-Llinares, F. Vedreño-Santos, J. A. Antonino-Daviu, and M. Fernández Cabanas, "Evaluation of the amplitudes of high-order fault related components in double bar faults," in *8th IEEE Symposium on Diagnostics for Electrical Machines, Power Electronics Drives*, 2011, pp. 307–315.

[16] S. Nandi, T. C. Ilamparithi, S. B. Lee, and D. Hyun, "Detection of eccentricity faults in induction machines based on nameplate parameters," *IEEE Transactions on Industrial Electronics*, vol. 58, no. 5, pp. 1673–1683, 2011.

[17] M. He and D. He, "Deep learning based approach for bearing fault diagnosis," *IEEE Transactions on Industry Applications*, vol. 53, no. 3, pp. 3057–3065, 2017.

[18] D. Lee Fugal, *Conceptual Wavelets in Digital Signal Processing*. Space Signals Technologies LLC, 2009.

[19] B. M. Ebrahimi, M. Javan Roshtkhari, J. Faiz, and S. V. Khatami, "Advanced eccentricity fault recognition in permanent magnet synchronous motors using stator current signature analysis," *IEEE Transactions on Industrial Electronics*, vol. 61, no. 4, pp. 2041–2052, 2014.

[20] M. Heydarzadeh, M. Zafarani, M. Nourani, and B. Akin, "A wavelet-based fault diagnosis approach for permanent magnet synchronous motors," *IEEE Transactions on Energy Conversion*, vol. 34, no. 2, pp. 761–772, 2019.

[21] A. Taspinar, Apr 2019. [Online]. Available: https://ataspinar.com/2018/12/21/a-guide-for-using-the-wavelet-transform-in-machine-learning/

[22] P. Karvelis, G. Georgoulas, I. P. Tsoumas, J. A. Antonino-Daviu, V. Climente-Alarcón, and C. D. Stylios, "A symbolic representation approach for the diagnosis of broken rotor bars in induction motors," *IEEE Transactions on Industrial Informatics*, vol. 11, no. 5,

pp. 1028–1037, 2015.

[23] S. Hoffs, "Synchronous generator fault diagnosis using shaft signal measurements," 2006.

[24] "Maxwell help," 2019.

[25] H. Ehya, "Private conversation," Doctoral Research Fellow at the Department of Electrical Engineering, NTNU, 10.2020.

[26] A. Nysveen, "Private conversation," Professor at the Department of Electrical Engineering, NTNU, 12.2020.

[27] M. Flaa, "Private conversation," Staff Engineer at the Department of Electrical Engineering, NTNU, 10.2020.

[28] B. J. W. Machowski, Jan and J. R. Bumby, *Power System Dynamics Stability and Control*, 2nd ed. John Wiley Sons, Ltd, 2008.

[29] C. Poulain, B. Metz-Noblat, and F. Dumas, "Calculation of short-circuit currents," 11 2005.

[30] Mostafa, "Ansys support," private communication, 2021.

[31] V. Krištof and M. Mester, "Loss of excitation of synchronous generator," *Journal of Electrical Engineering*, vol. 68, 03 2017.

[32] G. Dorsey and D. Kuhlmann-Wilsdorf, *Metal Fiber Brushes*, 11 2014, pp. 1151–1169.

[33] R. M. Bozorth, *Factors Affecting Magnetic Quality*, 1978, pp. 14–47.

[34] A. Mütze, "Bearing currents in inverter-fed ac-motors," 2004.

[35] H. Ehya, A. Nysveen, and T. N. Skreien, "Performance evaluation of signal processing tools used for fault detection of hydro-generators operating in noisy environments," *IEEE Transactions on Industry Applications*, pp. 1–1, 2021.

Appendix A

Schematic of Generator

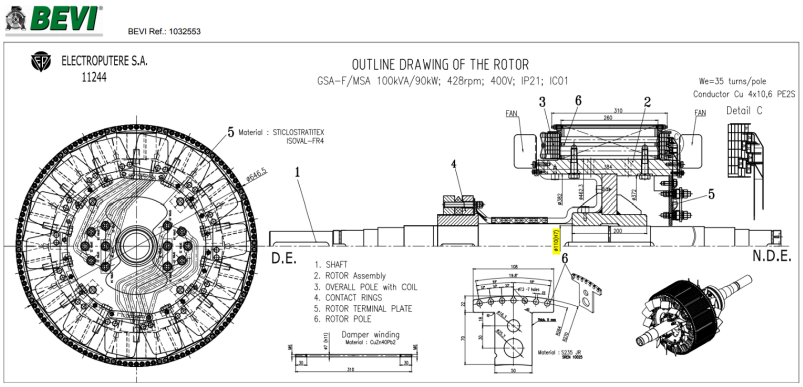

Figure A.1: Schematic of the rotor

FIGURE 10-1 Outline Drawing

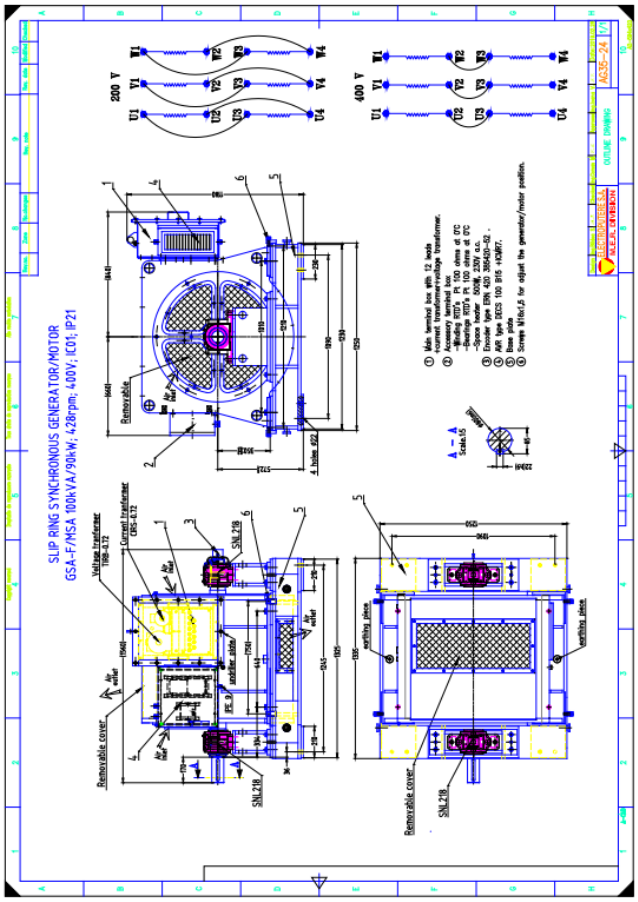

SLIP RING SYNCHRONOUS GENERATOR / MOTOR
GSA-F / MSA 100 kVA/100 kW ; 428 rpm ; 400 V ; IP21 ; IC01

Figure A.2: Schematic of the case

Appendix B

Schematic of messurment circuit that includes capacitanses of bearing and shaft isolation

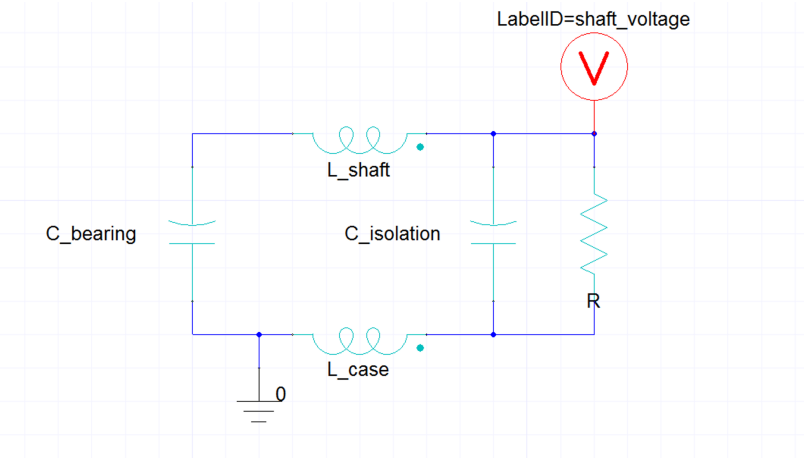

Figure B.1: Schematic of messurment circuit

Appendix C

Simulation results from the project work

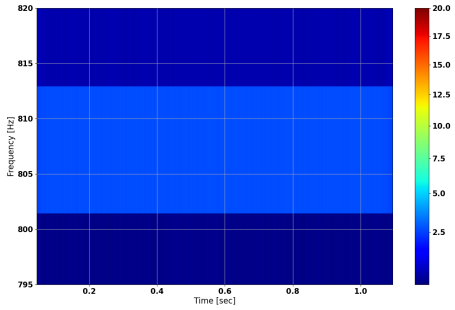

Figure C.1: CWT of the simulated healthy signal

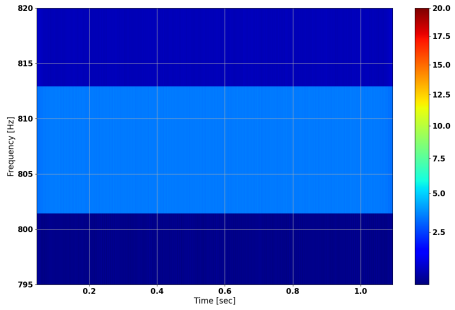

Figure C.2: CWT of the simulated shaft voltage with 1 short-circuited turn

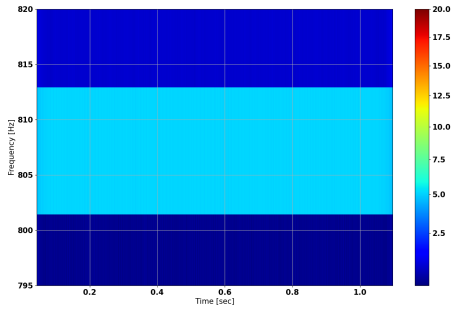

Figure C.3: CWT of the simulated shaft voltage with 2 short-circuited turns

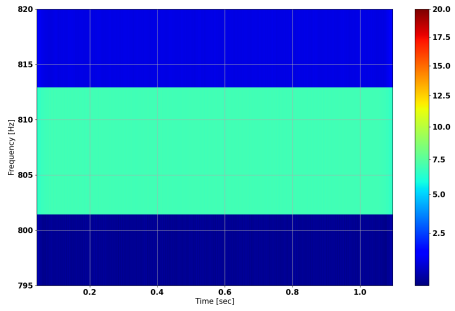

Figure C.4: CWT of the simulated shaft voltage with 3 short-circuited turns

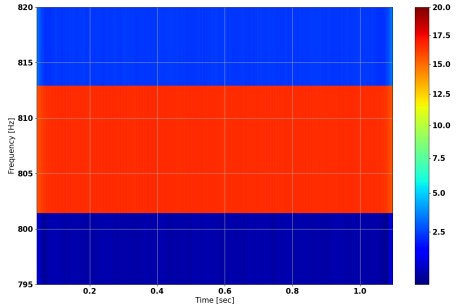

Figure C.5: CWT of the simulated shaft voltage with 7 short-circuited turns

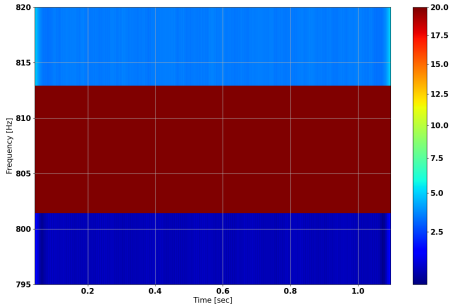

Figure C.6: CWT of the simulated shaft voltage with 10 short-circuited turns

C.1 SC

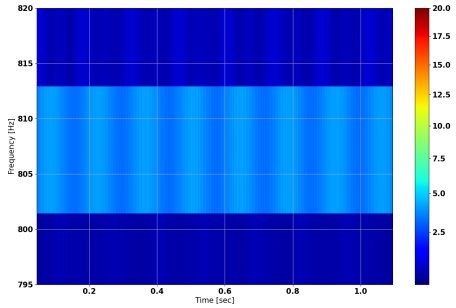

Figure C.7: CWT of the simulated shaft voltage with 10% static eccentricity

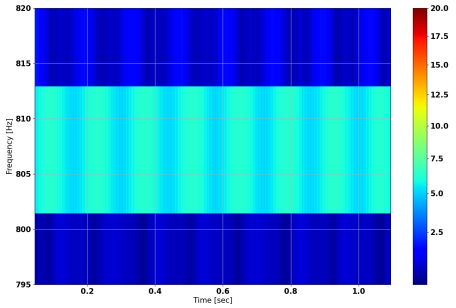

Figure C.8: CWT of the simulated shaft voltage with 20% static eccentricity

Appendix D

Amplitude spectrogram of voltage induced in the shaft and housing

D.1 ITSC

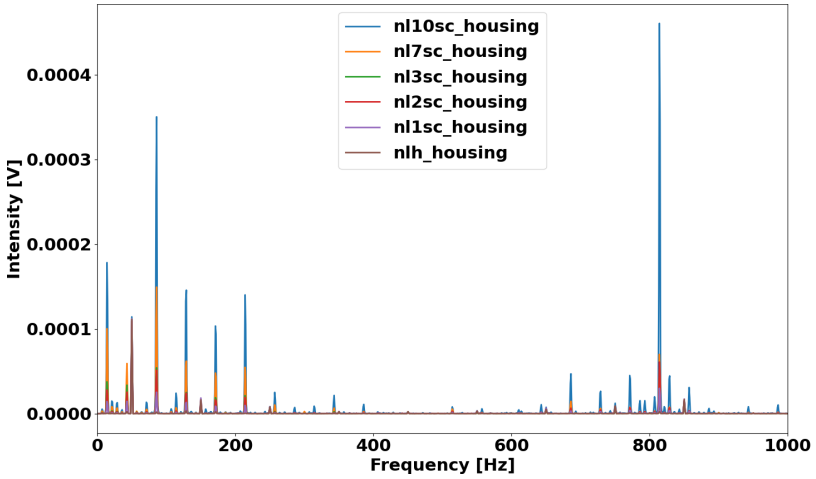

Figure D.1: Amplitude spectrogram of voltage induced in the shaft

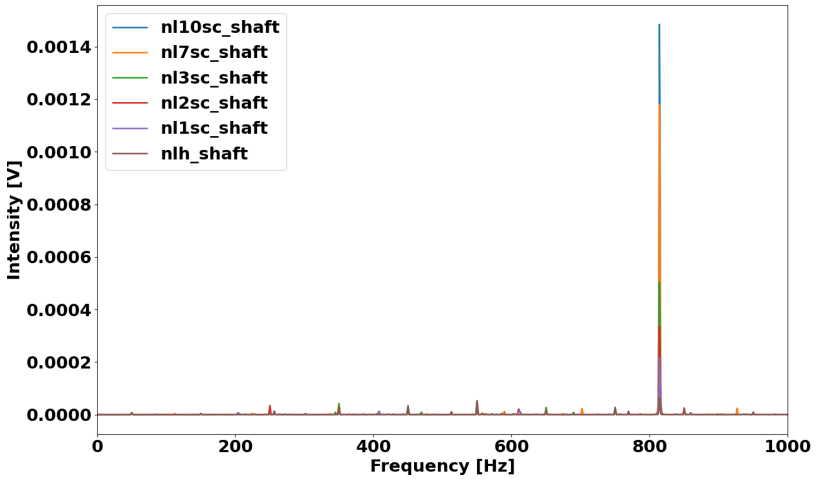

Figure D.2: Amplitude spectrogram of voltage induced in the housing

D.2 SE

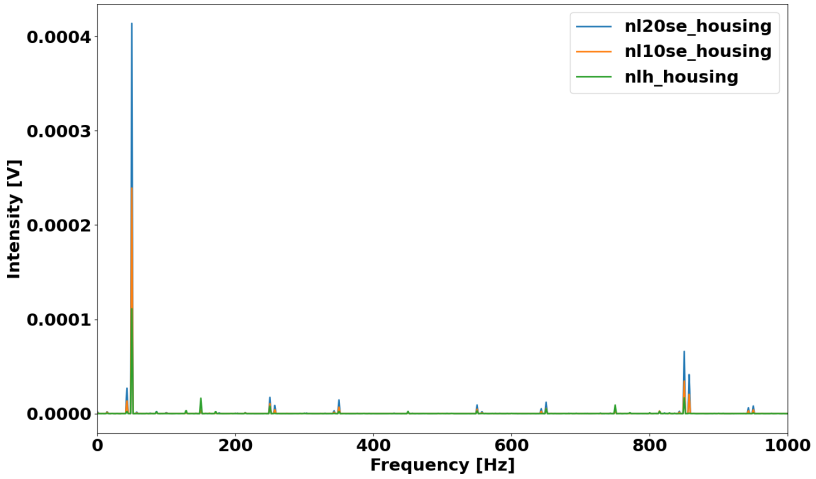

Figure D.3: Amplitude spectrogram of voltage induced in the shaft

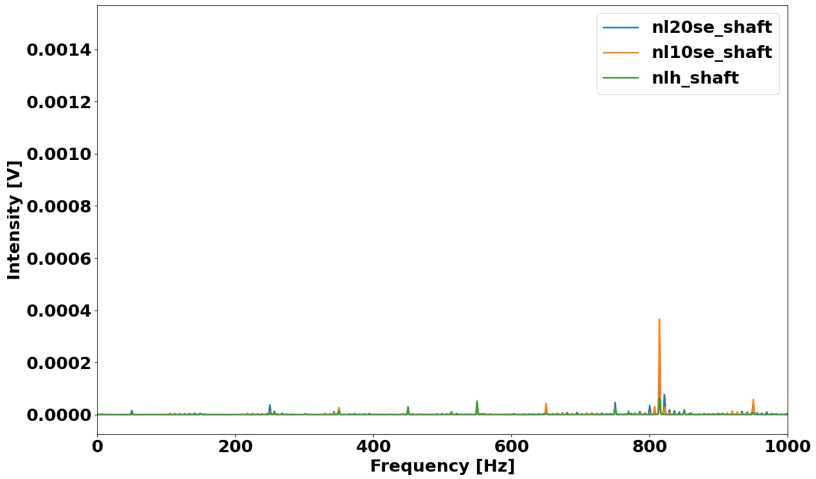

Figure D.4: Amplitude spectrogram of voltage induced in the housing

Appendix E

Comparison of healthy shaft voltage before and after measurements

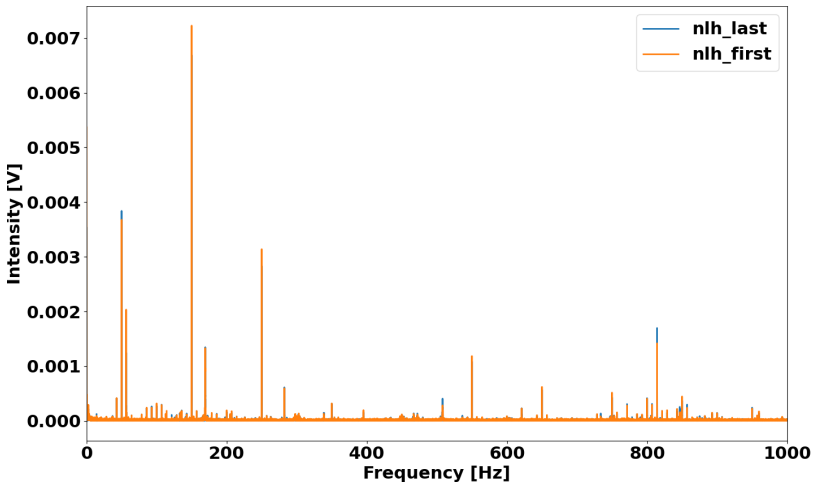

Figure E.1: Amplitude spectrogram that compares measured no-load healthy shaft voltage before and after measurements

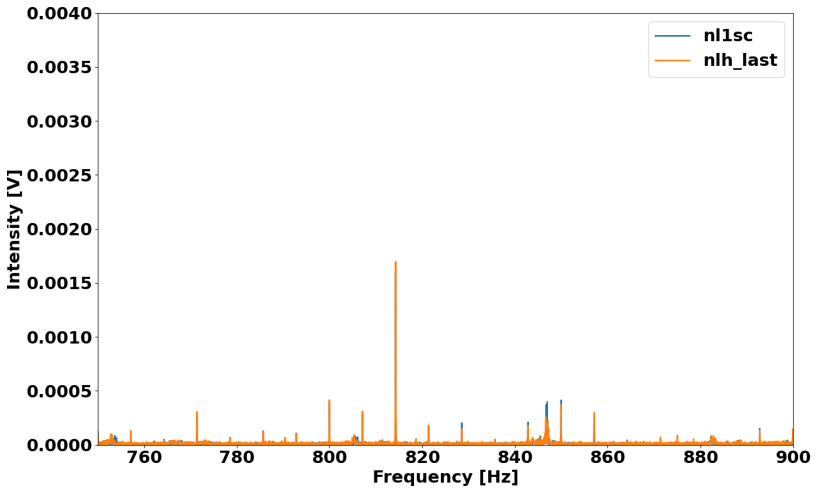

Figure E.2: Amplitude spectrogram that compares measured no-load after the measurements with 1 ITSC

Gaute Hagen Hallingstad

Online condition monitoring of synchronous generator using shaft signals

NTNU
Kunnskap for en bedre verden